TECHNISCHE UNIVERSITÄT MÜNCHEN

TUM School of Natural Sciences

Insight into All-solid-state Lithium Metal Batteries: Performance Enhancements and Failure Mechanisms

Yuxin Liang

Vollständiger Abdruck der von der TUM School of Natural Sciences der Technischen Universität München zur Erlangung einer

Doktorin der Naturwissenschaften (Dr. rer. nat.)

genehmigten Dissertation.

Vorsitz:	Prof. Dr. Lorenzo Tancredi
Prüfende der Dissertation:	1. Prof. Dr. Peter Müller-Buschbaum
	2. Prof. Dr. Aliaksandr Bandarenka

Die Dissertation wurde am 14.02.2025 bei der Technischen Universität München eingereicht und durch die TUM School of Natural Sciences am 27.03.2025 angenommen.

Abstract

Polyethylene oxide (PEO)-based composite electrolytes are promising for next-generation lithium metal batteries due to their safety, ease of fabrication, and electrochemical stability. However, their low ionic conductivity and high ethylene oxide (EO) chain crystallinity hinder commercialization. This thesis addresses these challenges by fabricating high-performance PEO composite electrolytes and conducting operando structural analyses using advanced X-ray scattering techniques. Grazing incidence X-ray scattering (GIXS) enabled real-time monitoring of electrochemical changes in morphology and crystalline structure, while nano-focus X-ray scattering revealed dendrite formation and solid electrolyte interphase (SEI) growth at the electrolyte-lithium interface. By integrating innovative fabrication and characterization methods, this research provides critical insights into the structural dynamics influencing electrochemical performance, paving the way for advancements in all-solid-state lithium metal batteries.

Zusammenfassung

Polyethylenoxid (PEO)-basierte Verbundelektrolyte gelten als vielversprechende Kandidaten für Lithium-Metall-Batterien der nächsten Generation, da sie sicher, einfach herzustellen und elektrochemisch stabil sind. Ihre geringe Ionenleitfähigkeit und die hohe Kristallinität der Ethylenoxid-(EO)-Ketten behindern jedoch die Kommerzialisierung. Diese Arbeit widmet sich diesen Herausforderungen in der Herstellung von Hochleistungs-PEO-Kompositelektrolyten durch die Durchführung von operando-Strukturanalysen mithilfe spezieller Röntgenstreutechniken. Die Röntgenstreuung unter streifendem Einfall (GIXS) ermöglichte die Echtzeitbeobachtung elektrochemischer Veränderungen in Morphologie und Kristallstruktur, während die Nano-Fokus-Röntgenstreuung die Bildung von Dendriten und das Wachstum der festen Elektrolyt-Interphase (SEI) an der Grenzfläche zwischen Elektrolyt und Lithium sichtbar machte. Durch die Kombination innovativer Herstellungs- und Charakterisierungsmethoden liefert diese Forschung entscheidende Einblicke in die strukturelle Dynamik, die die elektrochemische Leistung beeinflusst, und ebnet den Weg für Fortschritte bei Festkörper-Lithium-Metall-Batterien.

Contents

List of abbreviations

AC: Amplified current
ACN: Acetonitrile
Al: Aluminum foil
Al_2O_3: Aluminum dioxide
ASSLB: All-solid-state lithium batteries
CA: Chronoamperometry
CE: coulombic efficiency
CTAM: Conversion-type transition-metal compounds
Cu: Copper foil
CV: cyclic voltammetry
DA: decoupling approximation
DESY: Deutsches Elektronen-Synchrotron
DI water: Deionized water
DSC: Differential scanning calorimetry
DWBA: Distorted wave Born approximation
EIS: Electrochemical impendence spectroscopy
EV: Electric vehicles
FTIR: Fourier-transform infrared spectroscopy
GCD: Galvanostaic charge-discharge cycling
GISAXS: Grazing-incidence small-angle X-ray scattering
GIWAXS: Grazing-incidence wide-angle X-ray scattering
GIXS: Grazing-incidence X-ray scattering
ICE: Inorganic ceramic electrolyte
LFP: Lithum ferro-phosphate
Li: Lithium
LIB: Lithium ion battery
LiTFSI: Lithium bistrifluoromethanesulfonimidate

LLZO: $Li_7La_3Zr_2O_{12}$
LMA: Local monosdisperse approximation
LMB: Lithium metal batteries
LSV: Linear sweep voltammetry
NMP: N-methyl-2-pyrrolidone
nWAXS: Nano-focus wide-angle X-ray scattering
PEIS: Potentiostatic electrochemical impendence spectroscopy
PEO: Polyethylene oxide
PVDF: Polyvinylidene difluoride
SCE: Solid composite electrolyte
SDD: Sample-to-detector distance
SE: Solid electrolyte
SEI: Solid electrolyte interphase
SEM: Scanning electron microscopy
SLD: Scattering length density
SN: Succinonitrile
SPE: Solid polymer electrolyte
SS: stainless steel
Super P: Carbon black
T_c: Crystallization temperature
T_g: Glass transition temperature
TGA: Thermogravimetric analysis
T_m: Melting temperature
VFT: Vogel–Tammann–Fulcher models

1 Introduction

Humanity is confronting pressing challenges driven by the growing reliance on fossil fuels and their severe consequences for the climate and environment. To mitigate these impacts, it is imperative to develop and enhance technologies that enable the efficient conversion and storage of renewable energy. Advanced energy storage technologies have played a crucial role in driving social progress and transforming daily life. Since the creation of the first battery by Volta, known as the "voltaic pile," in 1800, battery technology has evolved significantly, leading to the development of various commercial batteries, including lead-acid, nickel-cadmium, nickel-metal hydride, and lithium-ion batteries (LIBs). Among these, LIBs are notable for their high energy density, making them ideal for applications ranging from portable electronic devices to large-scale power systems. Conventional LIBs, featuring graphite anodes with a theoretical specific capacity of 372 mAh g^{-1} and lithium transition metal oxide cathodes, have nearly reached their maximum theoretical specific energy density of 350 Wh kg^{-1} [1-3]. To surpass this limit and achieve energy densities exceeding 350 Wh kg^{-1} and 750 Wh L^{-1} at the cell level [4], the adoption of innovative anode and cathode materials with advanced technologies is necessary.

Batteries capable of outperforming LIBs — referred to as beyond-LIB technologies— are urgently needed for applications such as electric vehicles and grid energy storage. Among these alternatives, rechargeable lithium metal batteries (LMBs) have garnered significant attention due to their potential to double the energy density of current state-of-the-art LIBs [5]. As “holy grail” anode materials, lithium metal has the lowest electrochemical potential (-3.04 V vs. the standard hydrogen electrode), which enables high operating voltage, and remarkably high theoretical capacity (3860 mA g^{-1}), ten times higher than that of graphite [6-7]. In fact, while potentially providing high gravimetric energy, the low standard reduction potential of Li lies well outside the

stability window of most liquid organic electrolytes [8]. As a result, the electrolyte is reduced by the lithium metal, forming a solid electrolyte interphase (SEI). During charging, lithium plating occurs, leading to the formation of fresh lithium and the potential rupture of the SEI [9]. This exposes fresh lithium, which reacts with the electrolyte, reducing coulombic efficiency and increasing cell impedance due to the growing SEI thickness. The ruptured SEI also creates an uneven surface during lithium plating, contributing to the formation of dead lithium and dendrites. Depending on the current density, dendrites can develop as mossy structures at high current densities or needle-like formations at low current densities. The needle-like dendrites are more likely to penetrate the separator and make contact with the cathode, causing short-circuits and triggering thermal runaway [10]. This uncontrollable exothermic reaction between the cell components raises the temperature, producing highly flammable and toxic gases. As the temperature increases, the reaction rate accelerates, leading to further gas formation, and ultimately, the pressure build-up can cause the cell to explode and ignite [10-11]. Figure 1.1 summarizes the current challenges faced by LMBs and presents potential solutions to address these issues.

Efforts to improve LMBs have focused on four main strategies: solid electrolytes, artificial solid-electrolyte interphases, novel binders, and advanced separators [12-13]. All-solid-state lithium batteries (ASSLBs), which use solid electrolytes, are considered highly promising energy storage devices, offering exceptional energy densities and enhanced safety. The solid-state electrolyte plays a crucial role in these batteries, significantly influencing both their safety and electrochemical performance. Among the various solid-state electrolyte options, composite polymer electrolytes (CPEs) stand out as particularly promising due to their excellent overall performance. The new generation of ASSLBs, often referred to as Generation 4, holds great potential for meeting the increasing demand for safer and higher energy-dense batteries, particularly for large-scale applications [14-15]. However, several significant challenges remain that hinder their full commercialization. One of the primary obstacles is achieving ionic conductivity on par with traditional liquid electrolyte systems, typically greater than 10^{-3} S cm^{-1}, which is essential for ensuring efficient charge and discharge rates [16]. Additionally, reducing the substantial impedance at the electrode-electrolyte interfaces remains a key challenge that must be addressed for optimal performance. Another critical barrier is enhancing the electrochemical stability of the solid electrolyte when in contact with lithium metal. This is crucial to preventing degradation, dendrite

formation, and other issues that could compromise the battery's safety and longevity [17]. Overcoming these bottlenecks will be essential for unlocking the full potential of ASSLBs in practical, large-scale applications.

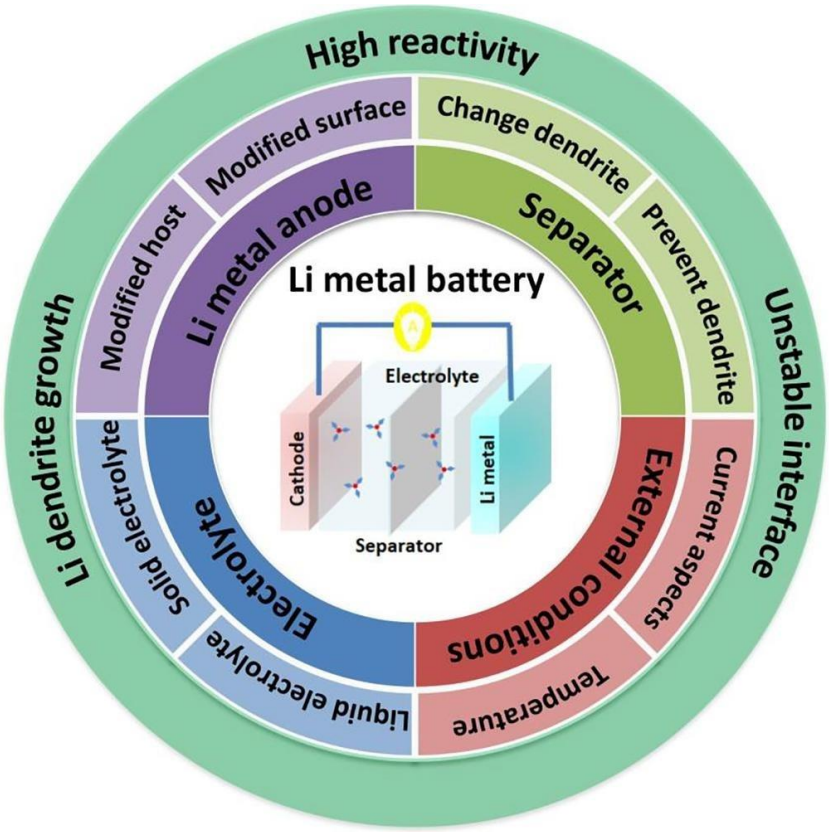

Figure 1.1. *Overview of the progress and challenges in lithium metal batteries [18]. Copyright 2021 Elsevier.*

In the present thesis, the PEO based composite electrolyte and its failure mechanism is investigated. PEO (polyethylene oxide) polymers were among the first materials studied for polymer electrolytes, with pioneering research conducted by Wright and Armand et al. in the 1970s. The oxyethylene group (-CH_2-CH_2-O-) in PEO can coordinate with lithium salts, allowing various lithium salts to dissolve into the PEO polymer matrix. Due to their excellent compatibility with metallic lithium, PEO-based composite electrolytes are among the most extensively studied systems, as they can be directly used with lithium metal anodes. However, pure PEO polymer solvated with lithium salts typically demonstrates low ionic conductivity, ranging from 10^{-8} to 10^{-7} S cm^{-1} at room temperature, due to the high crystallinity of the PEO chains. Many

methods have been tried to improve the performance of PEO-based CPEs, such as adding plasticizers and building blender copolymers and so on. However, investigation about the inner morphology and the crystal orientation evolution of the electrolyte during cycling, as well as the interfacial properties of Li metal electrode and PEO composite electrolyte are very limited.

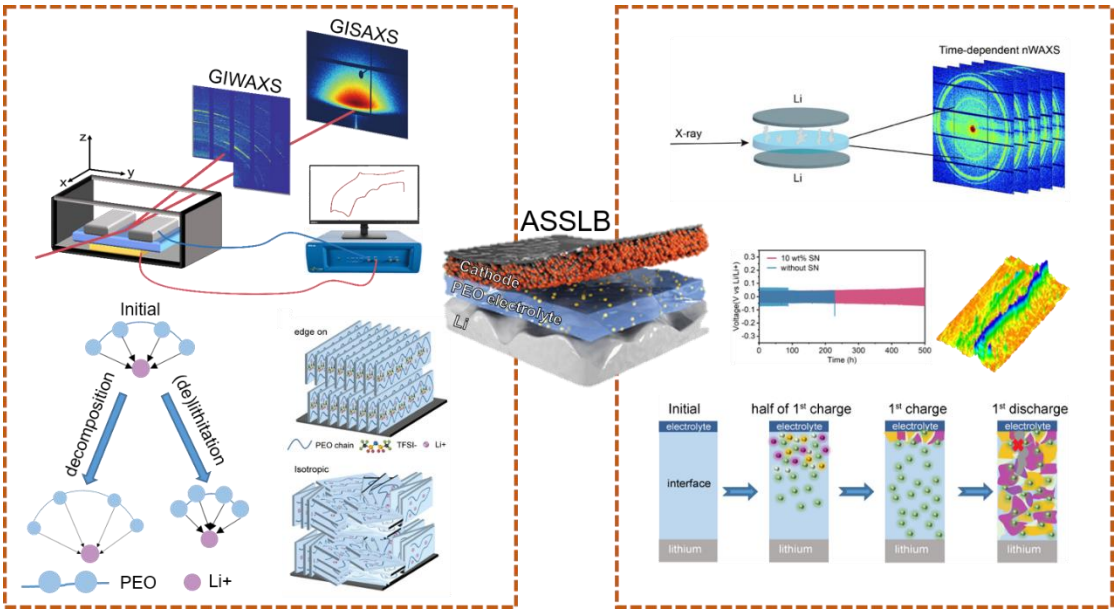

Figure 1.2. *Overview of the projects in presents Ph.D. thesis. The Figure is created from [19-20]. Copyright 2024 by the authors. This publication is licensed under CC-BY 4.0. Published by American Chemical Society. Copyright 2025 by the authors. Advanced Science published by Wiley-VCH GmbH.*

Grazing-incidence X-ray scattering (GIXS) offers a non-destructive and reliable approach to investigating the internal structure of PEO composite electrolytes. Specifically, grazing-incidence small-angle X-ray scattering (GISAXS) is used to examine the arrangement and configuration of the materials, while grazing-incidence wide-angle X-ray scattering (GIWAXS) allows for the analysis of crystallinity and the orientation. Nano-focused wide-angle X-ray scattering (nWAXS) enables detailed examination of crystalline structure changes at the electrode/electrolyte interface. With its transmission geometry and nanometer beam size, nWAXS provides valuable insights into the interfacial properties of PEO composite electrolytes and the failure mechanisms of lithium metal batteries (LMBs) during cycling. In this thesis, the evolution of the buried morphology and crystalline structure of PEO composite electrolytes is systematically studied using GIXS techniques. The interface between the Li anode and the PEO composite electrolyte is also analyzed using nWAXS. The primary objective

of this work is to gain a deeper understanding of the degradation mechanisms of LMBs with PEO composite electrolytes and to identify strategies for improving battery performance. Figure 1.2 outlines the research projects presented in this thesis.

In Chapter 2, the theoretical foundation of lithium batteries is explored, detailing their working principles and key components, including anode materials, cathode materials, and electrolyte materials. This chapter also provide the core concepts of solid composite electrolytes, focusing specifically on PEO-based composite electrolytes and their degradation mechanisms. Furthermore, the principles of X-ray scattering techniques—GISAXS, GIWAXS, and nWAXS — are thoroughly discussed. Chapter 3 outlines the primary characterization and analytical methods used in this research, encompassing structural, thermal, spectroscopic, and electrochemical analyses. Chapter 4 provides an overview of sample preparation, detailing the materials and fabrication processes utilized throughout the thesis.

In Chapter 5, PEO-LiTFSI composite electrolytes with Al_2O_3 as an inorganic filler are fabricated, and their performance is evaluated through electrochemical characterization. Operando GIWAXS/GISAXS techniques reveal buried morphology and crystalline structure changes during cyclic voltammetry sweeps. Under voltage, PEO-LiTFSI domains stretch, PEO-Li^+ coordination bonds weaken, and crystallite orientation shifts from edge-on to isotropic, generating a more disordered, amorphous structure that enhances ion transport. These insights offer valuable guidance for designing lithium metal batteries with high coulombic efficiency and improved conductivity.

Chapter 6 highlights the development of high-conductivity, interfacially stable PEO-based composite electrolytes. Succinonitrile (SN) is introduced to disrupt the PEO chain structure, as confirmed through FTIR and TGA analyses. The modified electrolyte exhibits a reduced glass transition temperature, indicating decreased PEO crystallinity. Electrochemical cycling tests are conducted to evaluate battery performance. Operando nWAXS is used in lithium symmetric cells to observe interfacial behaviors, including lithium dendrite formation and the evolution of the SEI layer.

The final chapter summarizes the overall conclusions of this thesis and provides a brief outlook for future research directions.

2 Theoretical Background

This chapter lays the groundwork for the topics addressed in this thesis by outlining background and theoretical concepts. Section 2.1 introduces lithium ion batteries, offering an overview of its principles. Section 2.2 elaborates the fundamental concept of solid composite electrolyte and its degradation mechanism. Section 2.3 introduces the PEO based composite electrolyte. Section 2.4 introduces the basic principles of X-ray scattering, including advanced techniques employed in this thesis, GISAXS, GIWAXS and nWAXS.

2.1 Lithium battery

In recent years, the development of high-energy-density lithium-ion batteries have positioned them as the ideal power source for electric vehicles (EVs) and hybrid electric vehicles (HEVs), revolutionizing the automotive industry. Lithium-ion batteries (LIBs) have garnered significant attention as a cutting-edge energy storage technology, thanks to their exceptional attributes, including high energy density, minimal self-discharge, negligible memory effect, elevated open-circuit voltage, and extended operational lifespan [21-22]. Their ability to deliver superior energy output while maintaining compact size and weight addresses the critical need for enhanced range and performance in modern vehicles. This alignment with the demands of sustainable transportation has solidified LIBs as a cornerstone technology in the shift towards greener, more energy-efficient automotive solutions. In this section, the working principle of LIBs and the crucial components of LIBs are discussed.

2.1.1 Working principle of battery

As shown in Figure 2.1, there are several different lithium-ion cell designs in the market: cylindrical, prismatic, button and pouch lithium-ion cells [21]. The cylindrical cell, commonly used in primary and secondary batteries, features a stainless steel exterior for mechanical stability and a pressure relief valve to prevent internal pressure build-up. Button cells, found in small devices like watches and medical tools, lack a pressure relief valve and can handle high-current charging. Prismatic cells, used in mobile phones and electric vehicles (EV) applications, have rectangular packaging but vary in dimensions by manufacturer. Pouch cells, a newer design without metal housing, offer high energy or power density, reduced weight, and efficient use of space, simplifying battery pack design.

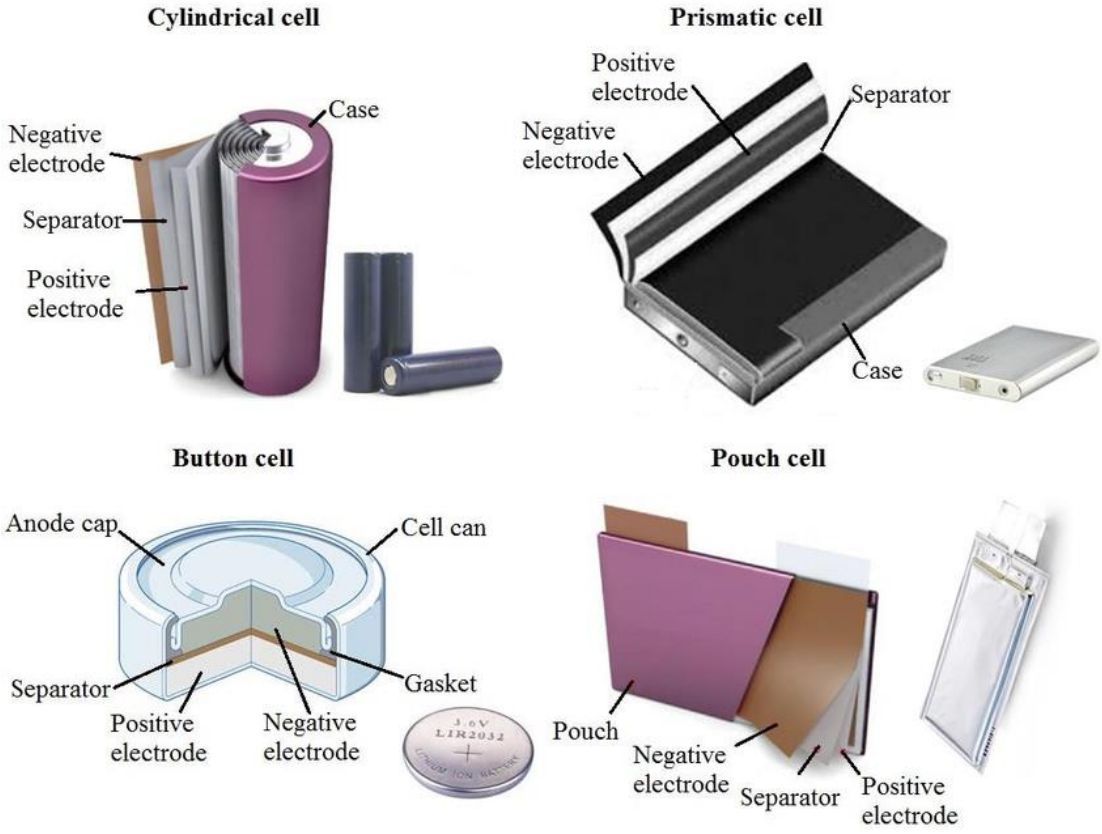

Figure 2.1. *The most common lithium ion batteries [23]. Copyright 2016 Lappeenranta University of Technology.*

Lithium-ion batteries, regardless of their external form — cylindrical, button-shaped, square, or soft-pack — share a consistent internal structure comprising five key components: the positive electrode, negative electrode, separator, electrolyte, and

battery casing. In most LIBs, the separator ensures the separation of the positive and negative electrodes, creating the core of the battery cell.

The fundamental operating principle of lithium-ion batteries involves the intercalation and deintercalation of lithium ions between the positive and negative electrodes. During the charging process, the two electrodes are connected to an external power source, which drives electrons to flow externally from the cathode to the anode. Simultaneously, lithium ions move internally from the cathode to the anode through the electrolyte. This process stores external electrical energy within the battery as chemical energy, housed in the anode and cathode materials, which have different chemical potentials. In contrast, during the discharging process, the flow is reversed. Electrons travel from the anode to the cathode through an external circuit, performing work, while lithium ions migrate internally from the anode to the cathode via the electrolyte. This cycle of lithium ions moving back and forth between the electrodes is referred to as the "shuttle chair" mechanism, representing the fundamental operation of lithium-ion batteries during charge and discharge. However, interactions between Li^+ ions and other battery components, such as the electrolyte and separator, can lead to incomplete reinsertion of Li^+ into the positive electrode. These interactions cause irreversible reactions, resulting in irreversible capacity loss.

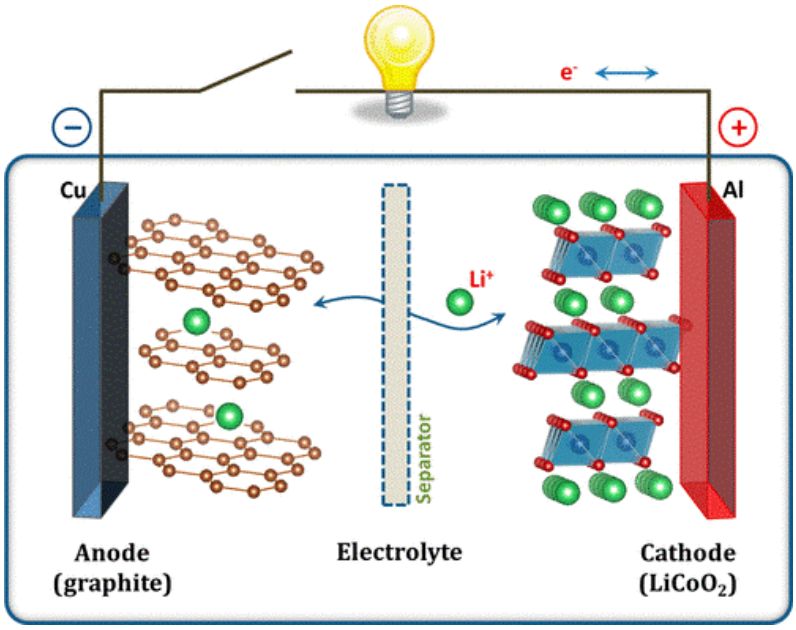

Figure 2.2. *Schematic illustration of the first Li-ion battery with $LiCoO_2$ as cathode and graphite as anode [24]. Copyright 2013 American Chemical Society.*

Figure 2.2 illustrate the basic operating principle of a typical LIB. In this design, lithium cobalt oxide ($LiCoO_2$) serves as the positive electrode material, while graphite is used as the negative electrode material. The electrolyte is typically carbonate-based electrolyte. During charging, the cathode undergoes delithiation and oxidation, where Co^{3+} is oxidized to Co^{4+}, releasing an electron. Positively charged lithium ions migrate through the electrolyte and separator to the graphite anode, where they are intercalated between graphene layers. Simultaneously, electrons supplied by the power source travel through the external circuit to the graphite structure, forming Li_xC_6 (where $0 < x \leq 1$). During discharging, the process reverses: lithium ions are extracted (delithiated) from the graphite anode and intercalated into the cathode, again crossing the electrolyte and separator. Electrons flow through the external circuit to the cathode, where cobalt ions are reduced. The chemical reactions involved in the charging and discharging processes are as follows:

$$Anode: \quad 6C + xLi^+ + xe^{-1} \underset{discharging}{\overset{charging}{\rightleftharpoons}} Li_xC_6 \tag{2.1}$$

$$Cathode: \quad LiCoO_2 \underset{discharging}{\overset{charging}{\rightleftharpoons}} Li_{1-x}CoO_2 + xLi^+ + xe^{-1} \tag{2.2}$$

$$Total\ reaction: \quad 6C + LiCoO_2 \underset{discharging}{\overset{charging}{\rightleftharpoons}} Li_xC_6 + Li_{1-x}CoO_2 \tag{2.3}$$

With these reactions, the theoretical specific capacity (mAh g^{-1}) of anode graphite can be estimated as [25]:

$$C_{specific} = \frac{xF}{nM} = \frac{1 \times (96485\ \frac{C}{mol})}{6 \times (12\ \frac{g}{mol})} = 372\ mAh\ g^{-1} \tag{2.4}$$

where x is number of electrons transferred in reaction (2.1) and in here 1 as the practical number of electrons transferred, F = 96485 C/mol is Faraday's constant, n is number of moles of a chosen electroactive component that take place in the reaction, and M is the molecular weight of the same electroactive component.

Similarly, the theoretical specific capacity of cathode can be estimated [25]:

$$C_{specific} = \frac{xF}{nM} = \frac{0.5 \times (96485\ \frac{C}{mol})}{1 \times (98 \frac{g}{mol})} = 137\ mAh\ g^{-1} \quad (2.5)$$

here, 0.5 as the practical number of electrons transferred.

In practice, evaluating the specific capacity of a lithium-ion battery cell requires considering not only the integration of cathode and anode materials but also other crucial components, including binders, conductive additives, separators, electrolytes, current collectors, the casing, tabs, and battery management systems. As a result, the actual energy density of the battery is always lower than the theoretical value based solely on its chemistry.

2.1.2 Anode materials

The anode plays a crucial role in the performance of rechargeable batteries, with its properties and structure significantly impacting the overall functionality of the battery. Graphite, with its unique hierarchical structure, is commonly used as the anode material in most commercially available batteries. When lithium ions intercalate into graphite, the relatively large gaps between adjacent layers of carbon atoms provide sites for lithium ions to insert, preventing changes in the anode's shape, size, and structure during the charge-discharge cycle. In addition to this traditional mechanism of lithium-ion intercalation, new approaches have also been explored, such as redox reactions in transition metal oxide anodes and displacement reactions in alloy anodes [26]. Figure 2.3 shows the different types of anode materials and a sketch of lithium storage mechanism.

Intercalation anode

The introduction of carbon as an anode material over 20 years ago made lithium-ion batteries commercially viable, and it remains the preferred choice for anodes today. The electrochemical activity of carbon arises from the intercalation of lithium ions between its graphene planes, which provide excellent two-dimensional mechanical stability, electrical conductivity, and efficient lithium transport. This structure allows for the storage of up to one lithium atom per six carbon atoms. Carbon has the combined properties of low cost, abundant availability, low delithiation potential vs Li, high Li diffusivity, high electrical conductivity, and relatively low volume change during lithiation/delithiation. Thus carbon has an attractive balance of relatively low cost, abundance, moderate energy density, power density, and cycle life, compared to any

other intercalation-type anode materials. Carbon's gravimetric capacity is higher than most cathode materials, but the volumetric capacity of commercial graphite electrodes is still small (330 – 430 mAh cm^{-3}). Although carbon-based materials have been commercialized as the anode for lithium-ion battery, they are facing formidable challenges. The main issue of the carbon-based materials is the relatively high irreversible capacity loss during the initial discharge/charge cycle, which results in a low coulombic efficiency [27]. Moreover, because the solid electrolyte interface (SEI) on the graphite surface will easily decompose at a temperature as low as 60 °C, the continuous heat flow from the exothermal reaction between the lithiated graphite and the electrolyte can quickly accumulate. When a large amount of heat is generated on the anode side during a short period of time, it would eventually trigger the major reaction between the cathode and the electrolyte, leading to a thermal runaway associated with fire or explosion of the battery.

From the safety perspective, titanium-based oxides including $Li_4Ti_5O_{12}$ and TiO_2 hold the great potential to be a class of attractive alternatives to graphite anode, since they operate at a potential above 0.8 V versus Li+/Li where the formation of a SEI layer on the anode surface can be avoided by eliminating the reduction of electrolytes [28]. These materials offer benefits like low cost, low toxicity, minimal volume changes during cycling, high power density, and long cycle life. However, the main drawbacks of this type of materials are the low inherent theoretical capacities (in the range of 175 – 330 mAh g^{-1}) and low electronic conductivity in bulk materials with micrometer-sized particles. The structure, morphology and size of titanium-based oxides strongly determine their electrochemical performance in a cell.

Alloy anode

Here, “alloying anode materials” refer to elements which electrochemically alloy and form compound phases with Li at a low potential (preferably below 1 V). The alloying mechanism has the general reaction of:

$$xLi^+ + xe^- + M \rightarrow Li_xM \tag{2.6}$$

where the typical examples of M are Si, Ge, Sn, P.

Of all alloying materials, Si has received the most attention due to its relatively low average delithiation potential, extremely high gravimetric and volumetric capacity, abundance, lost cost, chemical stability, and non-toxicity. Sn has also been of high interest, having similar properties except with lower gravimetric capacity, slightly lower

cell voltage, but higher electrical conductivity. However, Sn appears to suffer from easy fracturing, even when the particle dimensions are decreased to the 10 nm range. Ge does not fracture even at larger particles sizes but is too expensive for most practical application. Ga also has an interesting property of being liquid near room temperature but is again too expensive.

The alloying mechanism shares some of the most challenge issues. The first one is volume expansion and fracture. Large capacity of lithium storage in the materials unavoidably causes large volume expansion during lithiation, for example by 4 times in Si, 3.7 times in Ge, 2.6 times in Sn, 3 times in P [29-30]. The large volume expansion can cause mechanical fracture in individual particles, resulting in the loss of electrical contact and capacity fading. The second one is the instability of the SEI. The volume expansion during lithiation and contraction during delithiation causes the movement of interface boundary between the particles and electrolyte and thus the challenge of forming a stable SEI layer. The third one is the swelling at the electrode level. The volume expansion in the individual particle also results in the swelling at the whole electrode level and thus the challenges for the battery cell design.

Conversion anode

Conversion-type transition-metal compounds (CTAM) have risen to prominence as highly promising anode materials for lithium-ion batteries due to numerous attractive compositions alongside a high theoretical specific capacity. Some examples of conversion-type anode materials in LIBs include transition-metal sulphides, oxides, phosphides, nitrides, fluorides, and selenides [31-33]. The conversion mechanism has the general reaction:

$$M_xO_y + 2ye^- + 2yLi^+ \rightarrow yLi_2O + xM \tag{2.7}$$

where M are the transition elements and O can be replaced by S, Cl, P, N, and other elements.

One of the advantages of CTAM is that when compared to alloy anode materials their production costs could be relatively on the lower side. This is consequent to the fact that many CTAMs appear in their natural forms, such as magnetite (Fe_3O_4). Secondly, as a result of their lower lithium-intercalation potential CTAMs, unlike graphite anodes, do not experience the formation of lithium dendrites and therefore may make provision for better safety of operation for the LIB [34].

Notwithstanding, CTAMs have some major drawbacks, which include inherent poor electronic and ionic conductivity, continuous electrolyte decomposition, and relatively large volume expansion (< 200 %).

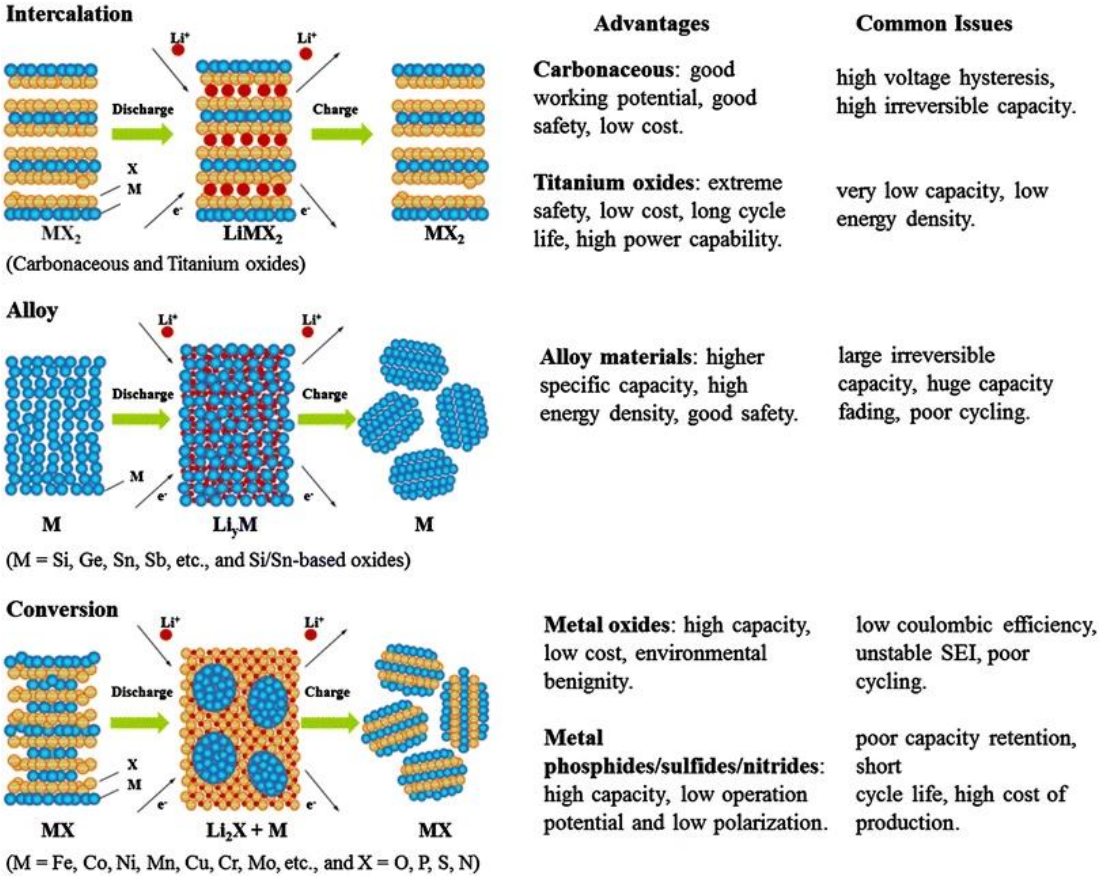

Figure 2.3. *Schematic illustration of three different types of anodes based on the lithium storage mechanism and their advantages and disadvantages [28]. Copyright 2018 John Willey & Sons.*

Lithium metal anode

Lithium metal is the ultimate choice for the anode in a Li battery, because it has the highest theoretical capacity (3860 mAh g^{-1}, or 2061 mAh cm^{-3}) and lowest electrochemical potential (–3.04 V versus the standard hydrogen electrode) of all possible candidates [7-35]. Lithium metal anodes can significantly increase the energy density of batteries by offering a much higher specific capacity than conventional anodes. State-of-the-art Li-ion cells can reach a specific energy of ~250 Wh kg^{-1}, which is an order of magnitude lower than the practical value of petrol (gasoline) [36]. However, challenges such as dendrite formation — where lithium metal grows in spiky structures during cycling — pose significant safety risks, including short circuits and

reduced battery life. The lithium dendrite growth mechanism and recent development will be discussed in Section 2.2.4.

2.1.3 Cathode materials

Cathode materials in lithium-ion batteries are usually transition metal oxides, capable of oxidizing to higher valence states as lithium ions are extracted. This oxidation helps maintain charge neutrality within the compound. However, significant compositional changes during this process can lead to phase transitions, necessitating the use of crystal structures that remain stable across a wide range of compositions. Figure 2.4 shows the different types of cathode materials.

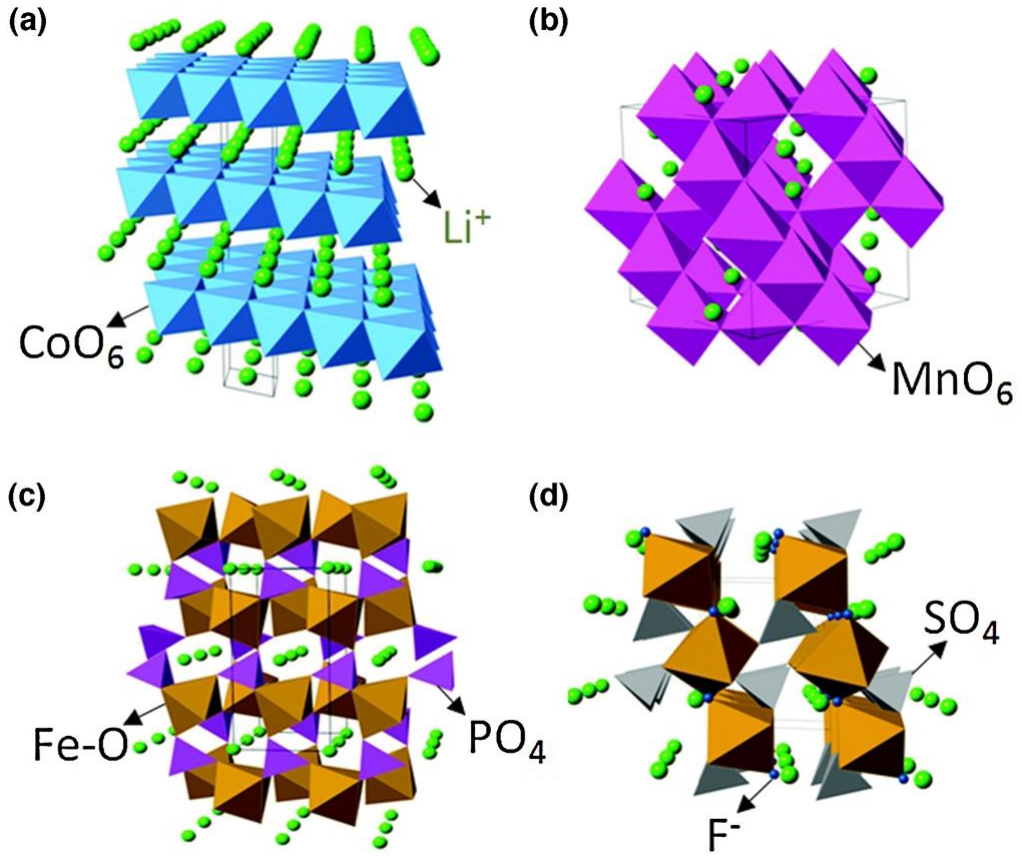

Figure 2.4. *Schematic illustration of different types of cathode materials: (a) layered ($LiCoO_2$), (b) spinel ($LiMn_2O_4$), (c) olivine ($LiFePO_4$), and (d) tavorite ($LiFeSO_4F$) [37]. Copyright 2015 Elsvier.*

Layered compounds

The ideal structure of layered compound $LiMO_2$ (M = Co, Ni, Mn, etc.) is demonstrated in Figure 2.4a. The layered $LiMO_2$ compounds are originally of rhombohedral

symmetry (R-3m) "ordered rocksalt" configuration, and the MO_2 slabs and Li layers are stacked alternatively [38-39]. Lithium ions can be reversibly removed from and inserted into this structure, creating or annihilating vacancies within the lithium layers. The c most commonly used layer cathode materials in lithium ion batteries is $LiCoO_2$. Although the conventional layered oxide $LiCoO_2$ has been commercialized as the LIB cathode for twenty years, it can only deliver about 140 mAh/g capacity which is half of its theoretical capacity [40]. Such limitation can be attributed to the intrinsic structural instability of the material when more than half of the Li ions are extracted. On the other hand, the presence of toxic and expensive Co ions in $LiCoO_2$ has introduced the environmental problem as well as raised the cost of the LIB. Another example is $LiNiO_2$, though isostructure to $LiCoO_2$, it acts differently in electrochemistry. In these layered structures, Ni, with partially filled e_g^* states, tends to reach a maximum of charge localization due to the $(t_{2g})^6$–$(d_{z2})^1$ electronic nature of Ni^{3+} and Jahn–Teller (J–T) distortion of NiO_6 octahedron, while in contrast Co prefers to achieve a maximum of charge delocalization [41-42]. Moreover, the Ni^{2+} ions have a tendency to substitute Li^+ sites during synthesis and delithiation, blocking the Li diffusion pathways.

Considering the Li–Ni disorder being major factor affecting the material rate capability, attempts to create new compounds of $LiCo_xNi_yMn_{1-x-y}O_2$ are motivated. In the system doped by divalent elements, the dopants will act as electrochemically active centers for valence change, leaving two trivalent ions to only take on +4 oxidation states stably, thus avoiding the Jahn–Teller effects. Therefore the presence of Co ions can help to reduce the amount of defect Ni in Li layer. Small amounts of cobalt (up to 0.20 – 0.25) have been shown to improve capacity [43]. Increased cobalt content can also reduce the loss in capacity during cycling. The improved performance has been attributed to cobalt increasing the conductivity and improving the structural stability of the cathode. Although nickel in the lithium layer can be detrimental to lithium transport, it has been shown to stabilize the structure during delithiation and thus improve cycling performance. $Li(Ni,Mn,Co)O_2$ can be overlithiated, which has been shown to improve electrode performance. The $Li(Ni,Mn,Co)O_2$ cathode materials has high capacity, good rate capability, and can operate at high voltages [44-46].

Spinel compounds

The space group of spinel materials LiM_2O_4 (M = Co, Ni, Mn, etc.) is Fd-3m, as shown in Figure 2.4b. The oxygen framework of LiM_2O_4 is the same as that of $LiMO_2$ layered structure. M cations still occupy the octahedral site but 1/4 of them are located in the Li layer, leaving 1/4 of the sites in transition metal layer vacant [47]. Li ions occupy the

tetrahedral sites in Li layer that share faces with the empty octahedral sites in the transition metal layer. The structure is based on a three-dimensional MO_2 host and the vacancies in transition metal layer ensure the three-dimensional Li diffusion pathways. The most common used spinel cathode is $LiMn_2O_4$ and is lower cost and safer than $LiCoO_2$. However the material was found to encounter sever capacity fading problem [48]. Two reasons have been considered as the main sources for the capacity fading: (1) dissolution of Mn^{2+} into the electrolyte generated by the disproportional reaction [49]: $2Mn^{3+} \rightarrow Mn^{4+} + Mn^{2+}$, and (2) generation of new phases during cycling and the related micro-strains. Partial substitutions of Mn with other transition metals such as Fe, Co, Cu, etc. are taken as an effective approach to improve the cycling stability [50]. The raises of intercalation voltages are the most obvious effects produced by doping which can be attributed to the high degree electronic reorganization around the dopant atoms and subsequently strong coupling between Li ion and M–O bonding [37-51]. For example, Co and Cu doping will lower the Li diffusion barrier, and the cathode system exhibits decreased reversible discharge capacity but high capacities at high rates.

Olivine compounds

A typical ordered-olivine phosphate structure (space group of Pnma), taking $LiFePO_4$ as an example, is composed by each FeO_6 octahedron linked with four FeO_6 octahedra in a corner-sharing way in the *bc* plane, while LiO_6 octahedra forming edge-sharing chains stacking along the *b*-axis [52], as shown in Figure 2.4c. High stability is an outstanding thermodynamic feature of olivine phosphates, and is mainly contributed by the extremely strong bond of oxygen–phosphorus. Large $(XO_4)^{3-}$ (X = S, P, Si, As, Mo, W) polyanions occupy lattice positions and increase cathode redox potential while also stabilizing its structure. Electronic conduction in $LiFePO_4$ occurs by small polaron hopping and is relatively low (10^{-9} S cm^{-1} for pure $LiFePO_4$). In $LiFePO_4$ cathode, Li^+ ion migration occurs preferentially via one-dimensional channels oriented along the [010] direction of the orthorhombic crystal structure [53-55]. However, the one-dimensional channel is easily blocked by impurities, disorder or defects, impeding the availability of active volume and long-range Li conduction. Besides, on the surface, the energy barrier of Li ions diffusion between channels is 0.52 – 0.77 eV, much higher than that of in subsurface (only 0.13 eV) [56]. Although the material shows excellent cycling performance, the main drawbacks of this material lie on its low energy density limited by the voltage, and its poor rate capability which is limited by the 1D ionic and poor intrinsic electronic conductivity. Different experimental approaches have been proposed to solve the problems: low voltage of the Fe^{3+}/Fe^{2+} redox couple can be

overcome by applying other transition metal redox, such as Co, Mn, and Ni; three main different approaches have been proposed to improve the conductivity successfully, including: (1) surface modifications, i.e. coating the particles with a conductive film; (2) size modifications; (3) doping either Li or Fe sites with other metal ions.

Tavorite compounds

Tavorite is a derivative class of the olivine structure and shares many of the characteristics with the olivine series. The crystal structure of $LiMPO_4F$ is shown in Figure 2.4d. In Tavorite compound, lithium ions are surrounded by transition metal octahedra and phosphate tetrahedra. Tavorites have good thermal stability due to the strength of the phosphorus and oxygen bonds but suffer from low energy density. The introduction of fluorine into the structure opens up the 1D ionic pathways to multidimensional pathways for Li diffusion [57-58]. $LiFePO_4F$ represents the typical tavorite material, with crystal structure similar to the naturally occurring mineral amblygonite $LiAlPO_4F$. Multidimensional diffusion pathways for Li ion transport in tavorite materials are the distinguishing characteristics from olivine materials [57]. This material exhibits a discharge capacity around 151 mAh g^{-1} is delivered with average discharge voltage of 4.05 V. Such excellent cycling performance suggests great structural stability with no phase transformation. It also exhibits good rate capability, retaining 90 % of the capacity when charged at 2C rate. $LiFePO_4F$ represents a new class of material that has great capacity retention, rate capability, and thermal stability.

2.1.4 Electrolyte materials

The electrolyte in a lithium-ion battery is a critical component that facilitates the movement of lithium ions between the cathode and anode during charge and discharge cycles. It acts as a medium for ion conduction while preventing direct electrical contact between the electrodes, which could lead to a short circuit. The electrolyte's properties are crucial for battery performance, including its energy density, cycle life, safety, and operating temperature range. Innovations in electrolyte formulations, such as the development of solid-state electrolytes, gel electrolytes, or additives that enhance stability and performance, are ongoing to address challenges like flammability, thermal runaway, and compatibility with high-capacity electrode materials. Figure 2.5 illustrate the four typical types of electrolyte materials and also demonstrate the performance comparison of various electrolyte.

Liquid electrolyte

Liquid electrolytes are the most widely used type in commercial lithium-ion batteries. They typically consist of lithium salts, such as lithium hexafluorophosphate ($LiPF_6$), dissolved in organic solvent mixtures like ethylene carbonate (EC), dimethyl carbonate (DMC), and diethyl carbonate (DEC) [59]. These electrolytes offer high ionic conductivity and efficient ion transport, which are essential for achieving the high power and energy density required by lithium-ion batteries [60].

However, liquid electrolytes also present safety concerns due to their flammability and the risk of leakage, which can lead to thermal runaway and fires. Enhancing the safety of liquid electrolytes is a key area of research, with significant attention given to developing less flammable or non-flammable solvent systems. One effective strategy involves incorporating flame-retardant additives into conventional electrolytes [61]. These additives help prevent ignition and combustion by scavenging free radicals and employing other mechanisms to suppress flammability.

All-solid-state electrolyte

All-solid-state electrolytes can generally be categorized into three types: solid polymer electrolytes (SPEs), inorganic ceramic electrolytes (ICEs), and solid composite electrolytes (SCEs), as illustrated in Figure 2.5. SPEs are composed of a polymer matrix mixed with lithium salts, offering excellent processability, flexibility, enhanced safety, and good interfacial contact with electrodes [62]. However, they suffer from low ionic conductivity ($<10^{-4}$ S cm^{-1}), limited thermal and electrochemical stability, and poor suppression of lithium dendrite growth [63-64].

In contrast, ICEs provide higher ionic conductivity (10^{-3}–10^{-2} S cm^{-1}), a wide electrochemical stability window, and strong mechanical properties but face challenges in achieving good interfacial contact with electrodes [65-66]. These limitations in SPEs and ICEs significantly hinder their commercial use in power lithium batteries.

SCEs, which combine SPEs with inorganic fillers, merge the advantages of both, resulting in high ionic conductivity ($>10^{-4}$ S cm^{-1}), good flexibility, and improved electrode contact. As a result, SCEs are considered one of the most promising electrolyte options for the next generation of all-solid-state lithium batteries [67-69].

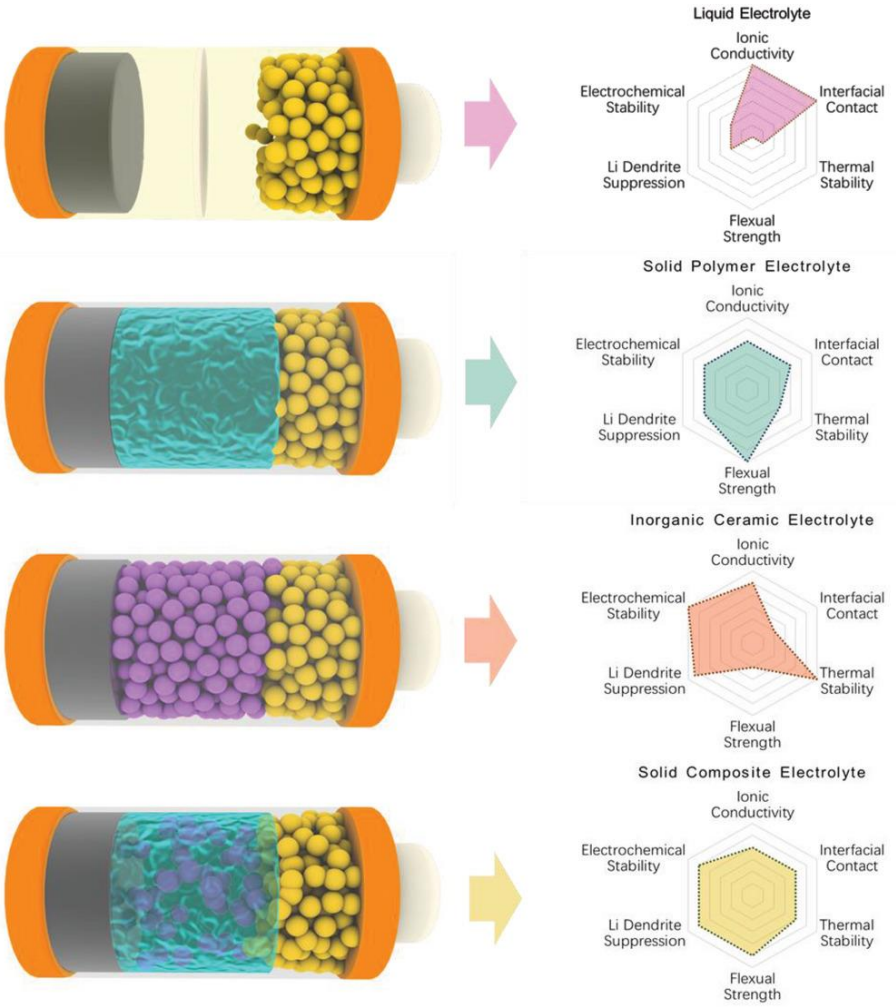

Figure 2.5. *Schematic illustration of different types of electrolyte materials and their performance comparison [70]. Copyright 2021 John Wiley & Sons*

2.2 Solid Composite Electrolytes

Solid composite electrolytes (SCEs) are advanced materials used in all-solid-state lithium batteries, combining the advantages of solid polymer electrolytes (SPEs) and inorganic ceramic electrolytes (ICEs). They consist of a polymer matrix integrated with inorganic fillers or ceramic particles, designed to enhance ionic conductivity, mechanical strength, and electrode compatibility. This section explores the components for solid composite electrolytes, the lithium-ion conduction mechanisms and the challenges associated with interfacial issues.

2.2.1 Components of solid composite electrolyte

The SCEs are composed of flexible polymer hosts, dissolved lithium salt, and rigid inorganic fillers. Figure 2.6 present the structure of common-used materials in SCEs.

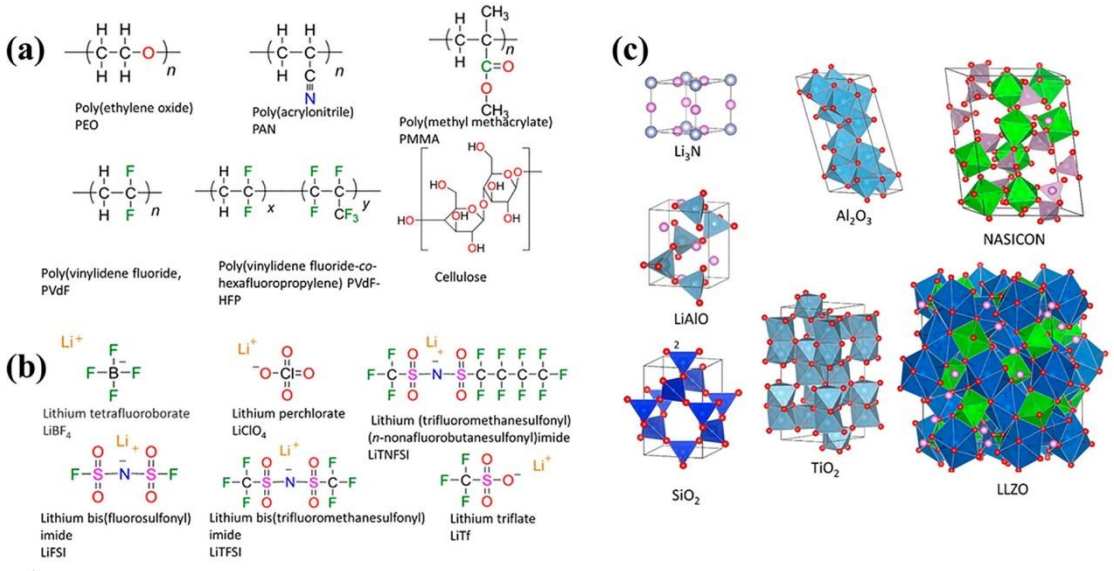

Figure 2.6. *Structures of (a) typical polymer electrolyte hosts, (b) lithium salts, (c) fillers [71]. Copyright 2020 American Chemical Society.*

Polymer matrix

Various polymers, such as polyethylene oxide (PEO), polyacrylonitrile (PAN), polymethyl methacrylate (PMMA), polyvinylidene fluoride (PVDF), etc., have been used as polymer matrices to develop solid composite electrolytes [72-74]. Figure 2.6a indicates the basic chemical structures of several extensively-studied polymer matrices. These polymers can generally be classified into three types: amorphous, semi-crystalline, and crystalline. The ionic transport in amorphous polymers (or the amorphous section of a polymer) is under the controlment of an external electric field that is induced by the formation and break-off of coordination bonds due to the segmental motion of polymer chains. In crystalline polymers (or the crystalline section of a polymer), it has been proposed that the transport of Li^+ ions is not related to the chain segments but depends on the ionic hopping over the spiral channels. In this case, the glass-transition temperature (T_g) and melting point (T_m) determine their temperature-dependent Li^+ ion conductivities. Specially, the glass-transition temperature plays as a critical parameter in polymeric electrolytes. The ionic conductivity is usually low at temperatures below T_g, but it could be significantly enhanced above or close to the T_g. Therefore, the reduction in T_g is a crucial strategy to

improve the ionic conductivity of polymeric matrix materials [75].

The use of polymer matrices in composite solid electrolytes has the following advantages: i) the incorporation of polymers can significantly improve the flexibility of solid composite electrolytes, ii) the presence of polymers can help minimize the resistance at the electrode-electrolyte interface; and iii) polymers are usually easier to process and more cost-effective than inorganic ceramic electrolytes, which are beneficial for the large-scale manufacturing processes. Among the above listed polymer electrolytes, PEO and PAN are the most widely studied ones for constructing polymer-ceramic composite electrolytes.

Lithium salts

Lithium salts for the investigation of polymer-ceramic composite electrolytes include $LiN(SO_2F)_2$ (LiFSI), $LiN(CF_3SO_2)_2$ (LiTFSI), and $LiClO_4$, etc., as shown in Figure 2.6b. These lithium salts are also widely used in liquid electrolytes due to their high solvability, good electrochemical stability, high thermal stability, and ability to promote the formation of a stable SEI [76-77].

Inorganic fillers

Incorporating inorganic fillers into the polymer matrix enhances the ionic conductivity of solid composite electrolytes by reducing crystallinity, improving the stability of the electrode-electrolyte interface, and increasing the cation transference number.

Inert fillers are mainly oxide ceramics with sphere particle shape like Al_2O_3, SiO_2, TiO_2, as shown in Figure 2.6c. The inert (passive) fillers are not able to provide ionic conductivity on their own, but these filler materials still play important role in the development of polymer-ceramic composite electrolytes [78-79]. With specific structures, inert filler materials are able to create more or low-energy conduction paths [80]. Some inert filler materials can also restrict the recrystallization of polymer chains due to their special surface groups and large surface area which can increase the size of local amorphous regions and thus promote Li^+ transport through preferential ion conduction pathways. In addition to the conductivity enhancement, inert fillers can support polymer matrix to improve the mechanical properties, such as Young's modulus and tensile strength [81].

Al_2O_3 and TiO_2 can act as cross-linking centers for the polymer segments to affect the recrystallization kinetics and decrease the crystallinity of polymer, thus enhancing the ion transport within the polymer chains [82]. However, despite the general roles in

crystallinity decrease, inert fillers also contribute to the Li ion transport behavior at the boundaries of the ceramic fillers, which comes from the Lewis acid interactions between the cations/anions from lithium salts and the surface groups of ceramic fillers [83]. Therefore, it is important to decrease the size of inert fillers to nanometer size and furthermore reduced the interfacial resistance between the polymer and the electrode, thus resulting in increased conductivity. With abundant hydroxyl groups on the surface, SiO_2 has also been extensively studied as an ionic conductivity enhancement material. Compared to other ceramic fillers, much stronger chemical/mechanical interactions coming from surface hydroxyl groups on the SiO_2 can lead to better stabilized interface between fillers and polymer matrix [84-85], thus effectively suppressing the crystallinity of the polymer matrix and increasing the ionic conductivity of solid composite electrolyte.

Furthermore, active fillers as ionic conductor are also used in the solid composite electrolyte, proved to be more effective in improving the electrolyte ionic conductivity than inert fillers. The active fillers commonly cover all the Li ion-conducting materials, such as NASICON-type (such as $Li_{1.5}Al_{0.5}Ge_{1.5}(PO_4)_3$ [LAGP] and $Li_{1.3}Al_{0.3}Ti_{1.7}(PO_4)_3$ [LATP]), garnet-type ($Li_7La_3Zr_2O_{12}$ [LLZO], La-site: Ca, Sr, Ba, K, etc., and Zr-site: Ta, Nb, etc.), and some other ceramics (LiPON, Li_3N), as illustrated in Figure 2.6c.

The corner-sharing tetrahedral PO_4 and octahedral MO_6 in the crystalline NASICON structure form a 3D network structure, which can be turned into a Li conductor when Na^+ is replaced by Li^+, with the sacrifice of ionic conductivity due to the ionic radius difference between those two ions [86]. The advantages of NASICON type ceramics include their excellent water and air resistance as well as the high electrochemical stability of up to 5 V versus Li+/Li, which is ideal for batteries [87]. On the other hand, the main drawbacks of NASICON type ceramics are their chemical instability when contacting with lithium metal, but this problem can be minimized to some degree when PEO polymer is incorporated into the electrolyte system. A garnet type ceramic with zirconium element was developed (LLZO), and it possessed a high conductivity of 2.44×10^{-4} S cm^{-1} with a low activation energy of 0.31 eV [88]. Garnet-type ceramic electrolytes are very stable and can stand higher thermal exposure up to 900 °C. Besides, unlike NASICON type electrolytes, which undergo reduction reactions with Li metal, the garnet-type is chemically stable against Li metal. However, the application of garnet-type ceramic electrolytes in all-solid-state Li metal batteries is hindered by the poor contact between the electrode-electrolyte interfaces. Hence, to improve the interfacial compatibility, surface modification techniques should be considered.

2.2.2 Lithium ion conducting mechanism

In solid electrolytes, Arrhenius and Vogel–Tammann–Fulcher (VTF) models are used to quantify the ionic conductivities, which corresponds to the different ionic conduction mechanisms in the solid conductors [89]. For inorganic solid electrolytes, the ion-conducting mechanism can be well described with Arrhenius behavior. The ionic conductivity with temperature dependence is given by:

$$\sigma = A\exp(^{E_a}/_{k_B T}) \tag{2.8}$$

where A is the pre-exponential factor related to the charge carrier, k_B is the Boltzmann constant, and E_a is the activation energy. The ionic conductivity is inversely proportional to the activation energy, where the activation energy is defined as the energy barrier between adjacent available sites. The diffusion of ions in inorganic solid electrolytes is generally realized by a hoping mechanism through the connected available vacancies and interstitial sites in the crystal, and therefore the concentration and distribution of point defects in crystals largely determine the conducting behavior of solid materials.

The Arrhenius equation describes the relationship between ion conductivity and temperature. However, the Arrhenius equation has great limitations due to the complexity of ion transport in polymers [90]. Then the VTF equation:

$$\sigma = {}^{1}/_{2}\, A \exp\left(^{-E_a}/_{k_B(T - T_g)}\right). \tag{2.9}$$

Here, the glass transition temperature is T_g. When the temperature T is less than the glass transition temperature T_g, the relationship between the ion conductivity and the temperature conforms to the Arrhenius equation; otherwise, it conforms to the VTF equation.

Ion conducting with polymer chain

There are three types of polymers: crystalline, semi-crystalline and amorphous polymer. Figure 2.7 shows the ion conduction mechanism within different polymers. In a polymer matrix, lithium salts interact with specific coordination sites to form complexes in accordance with Lewis acid–base theory. In this arrangement, anions and

cations dissociate, hop, and re-coordinate as local polymer segments regenerate new coordination sites nearby. This process is driven by the dynamic motion of amorphous polymer chains within the available free volume. When an external electric field is applied, it facilitates directional ion movement, a mechanism known as the ion conduction process, as shown in Figure 2.7a. Based on this reasoning, one can concluded that ion transport occurs in the amorphous phase with activated polymer chain segments above the polymer glass transition temperature (T_g).

In crystalline polymers, a different conduction mechanism occurs where Li^+ movement does not depend on the incompact chain segments but on hopping over spiral channels, as shown in Figure 2.7b. The crystalline polymer chains fold to form interlocked cylinders (channels) inside the ordered framework. The Li ions reside in the channels and the anions are located outside and are not coordinated to Li ions.

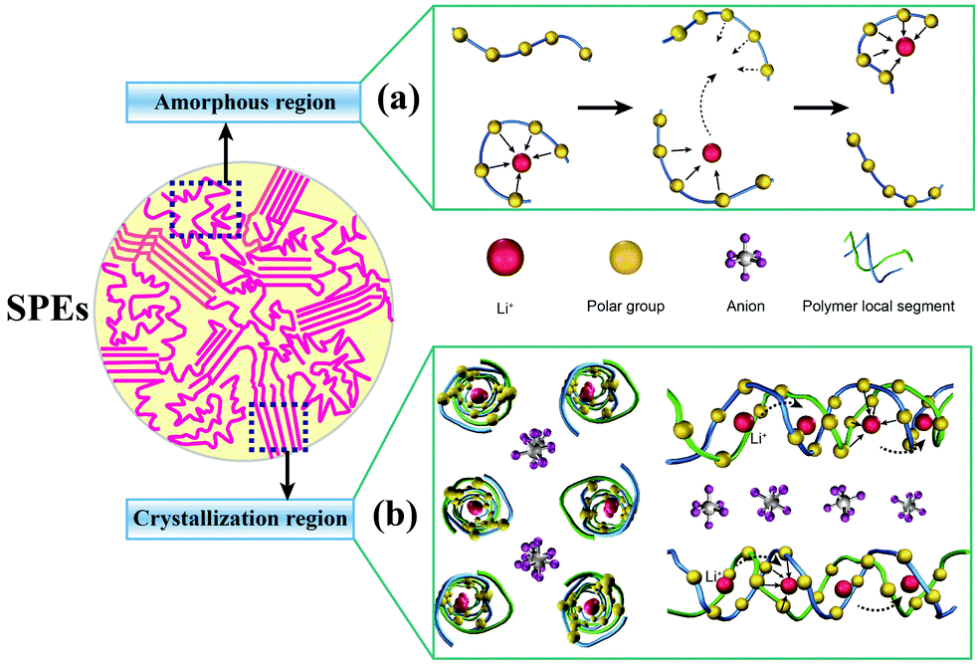

Figure 2.7. *Schematic of conduction mechanism in: (a) amorphous polymer electrolytes and (b) crystalline polymer electrolytes [91]. Copyright 2016 The Royal Society of Chemistry.*

Lithium ion conduction in solid composite electrolyte with inert fillers

With passive fillers such as SiO_2, Al_2O_3, and ZrO_2, the ion-conducting mechanism is the same as solid polymer electrolytes because the filler is Li^+ insulating. In these composite solid electrolytes, the function of the inorganic fillers originates mainly from

following two improvements: i) decrease in crystallinity and glass transition temperature of polymer matrix due to the modification of local structure of polymer chains, and ii) increase of free Li^+ because the functional groups of inorganic filler can help further dissociate Li salts based on the Lewis acid-base theory [92-93]. Although the ionic conductivities are greatly enhanced, the ion conduction in these composite solid electrolytes with passive fillers is still contributed by the segmental motions of polymer chains.

Figure 2.8 shows a schematic diagram of the ion transport pathways in inert filler doped composite electrolyte. As shown in Figure 2.8, the diffusion through the function of polymer electrolyte polar atoms is slow, which is ascribed to that the polymer is easy to crystallize at room temperature and ion conductivity is closely related to the amorphous region. Constructing composite electrolytes could add a high conductive interface. Furthermore, the continuous interface channel is the optimal choice to fabricate composite electrolyte with high ionic conductivity.

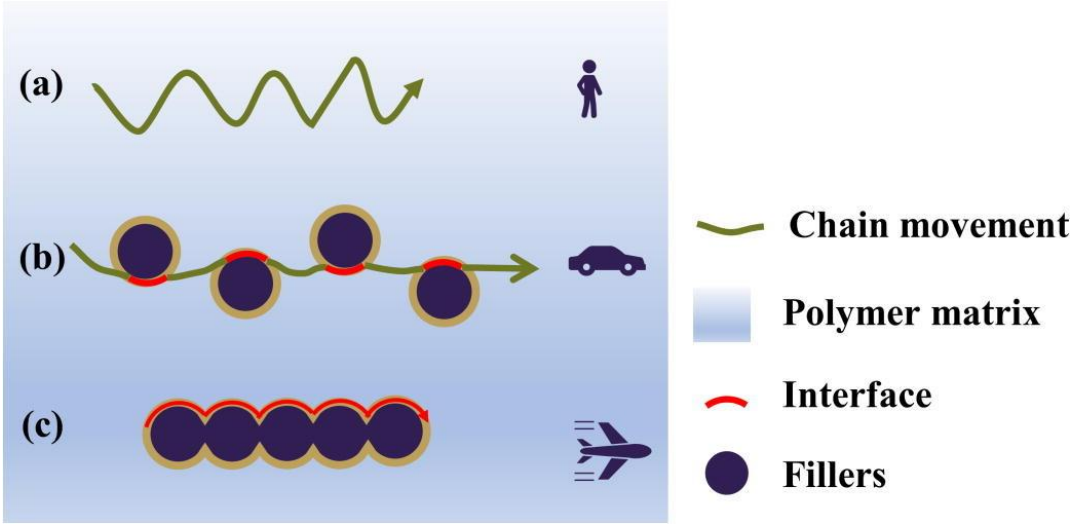

Figure 2.8. *Schematic of (a) ion transport in pure polymer electrolyte. (b) Ion transport in disconnected interface. (c) Ion transport in continuous interface [94]. Copyright 2022 Elsevier.*

Lithium ion conduction in solid composite electrolyte with active fillers

Lithium-ion transport in active filler occurs either via the vacancy mechanism or the interstitial mechanism. The vacancy mechanism normally relies on Schottky defects, the configuration of cation vacancies accompanied by anion vacancies. Due to this particular structure, a large number of vacancies are available for lithium ions to migrate through active fillers. As for the interstitial mechanism, it is mainly related to Frenkel

defects, the configuration of anion vacancies accompanied by cation interstitials [95].

Regarding the SCEs with active fillers, Li ions may migrate through three conducting pathways: 1) pure polymer electrolyte phase; 2) interfacial phase between active fillers and polymer chains; 3) a percolated network made of connected active fillers (Figure 2.9).

The Li ion migration pathways in SCEs normally depend on the concentration of the active filler in SCEs. At a low active filler content (<20 wt%), the ions mainly transfer in the PEO phase, which is the ion conduction behavior of CPE modified by active filler. When the concentration of active filler is above the percolation threshold (>20 wt%), a percolated network is formed by loosely connected active filler particles. The ion transport pathways gradually transition from polymer phase to the percolated network, whereby, the Li ion migration in active filler particles dominates ion conductance [96]. Consequently, when the active fillers are at a low concentration the ion migration mainly takes place in the polymer phase. As the concentration of active fillers is increased, the ion transport pathways in SCEs gradually change from the polymer phases to a percolated network of connected active fillers.

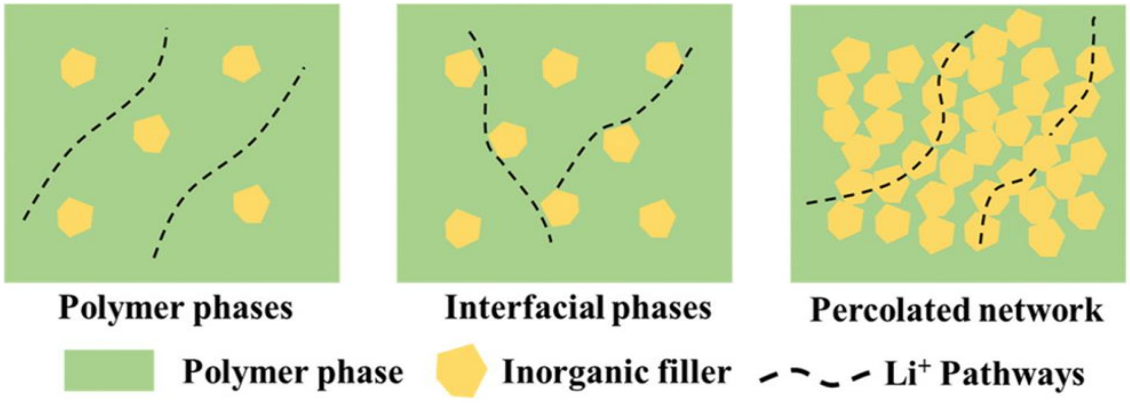

Figure 2.9. *Schematic of Li ion transport pathways in CPEs [97]. Copyright 2021 John Wiley & Sons.*

2.2.3 Interfacial issue: Lithium dendrite growth

As mentioned in Section 2.1.2, lithium metal is the ultimate choice for the anode in a Li battery due to highest theoretical capacity and lowest electrochemical potential. However, the battery system based on a lithium metal anode cannot last long because lithium dendrite growth upon cycling can trigger battery thermal runaway. Dendrites are generally rigid tree-like structures with needle-like projections (called whiskers)

that grow at the anode. The growth of dendrite structures at the anode penetrates through the electrolyte and reaches the cathode during the cell operation [94]. Also, the uneven plating and stripping of Li dendrites during long-term cycling peels off the dendrites from the current collector to produce "dead Li", which becomes electrochemically inactive and results in severe capacity decay. Therefore, the specific capacity deteriorates and causes short-circuiting of the battery, and finally damages the device and shortens its life span. When increasing the miniaturization and compactness of devices, the growth of dendrite structures is one of the significant threats that need to be eliminated for developing high energy density and long life in the battery.

Figure 2.10 shows the dendrite growth mechanism in solid electrolyte (SE), and can be concluded in to four parts: (I) dendrite grows at the tip and penetrates the SE through the soft part (Dendrite Growth at the Tip), (II) dendrite grows laterally and extends from the side of electrode and CPE (Lateral Growth of Dendrite), (III) subsurface structure buried under dendritic structure triggers the formation of dendrite (Subsurface Structure Triggers Dendrite Growth), and (IV) additional effect caused by the redistribution of charge in Li|SE interface induces Li dendrite (Redistributed Charges at Interface Accelerate Dendrite Formation) [98].

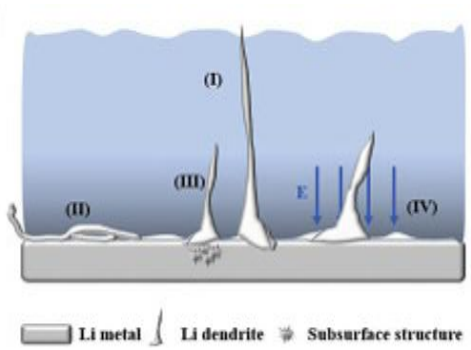

Figure 2.10. *Schematic illustrating the dendrite growth mechanism in solid electrolyte [98]. Copyright 2020 Cell.*

Tip deposition is usually used to explain dendritic growth. The protrusions at the surface of the electrode generate enhanced electric and ionic fields near the spherical tip, which strongly affect the deposition behavior. Needle-like dendrites gradually grow at the tip as the electrodeposition time increase and eventually pierce the electrolyte. Li deposition was more likely to happen at the dendrite tip, due to the relatively faster accumulation of electric charges than in the smooth region. The dendrite grows and penetrates through the polymer once activated, although lowering the current density

and enlarging the distance between electrodes that could slow the growth rate. Apart from this, the dendrite could also propagate laterally. As the deposition occurred, the dendrite can still growth even after the tip moves out of the electrolyte. Li ions deposit through the SEI laterally and thus accelerate dendrite growth. As a result, the lateral growth of Li dendrite leads to delamination between the electrode and electrolyte [99]. Also, the insufficient contact between SE and electrode is believed to induce dendrite protrusion due to the free space formed for dendrite growth. Furthermore, most dendrites are buried under the electrode but did not reside within the electrolyte in the early stage of dendrite development. Compared with dendrite growth in solid electrolyte at the tip and side, the subsurface structure greatly affects dendrite nucleation in the initial process. The additional phenomenon causes by redistribution of charges at the Li|SE interface also affects the Li deposition. In normal dual-ion SE, anions move freely and gather at the cathode side to form electric fields, which accelerates dendrite growth.

Combining the benefits of inorganic and organic solid electrolytes, SCEs can effectively prevent both stages of dendrite formation. During the nucleation stage, the polymer improves the electrode contact with traditional inorganic solid electrolytes [100]. Simultaneously, the polymer is capable of accommodating lithium metal expansion during cycling, ensuring that the composite electrolyte remains in close contact with lithium metal. Secondly, an interfacial reaction produces a dense, high ionic conductivity SEI film that uniformly deposits lithium ions on the negative side. Third, the composite electrolyte's low electronic conductivity ($< 10^{-10}$ S cm^{-1}) prevents Li^+ from being reduced to Li^0 by electrons. Finally, the transference number of Li^+ is a critical parameter for controlling the nucleation of lithium dendrites. If the anions' mobility is limited (i.e., only Li^+ ion transfer), the electric field caused by the charge redistribution can be eliminated [99]. As a result, dendrite growth caused by space charge can be successfully minimized.

2.2.4 Interfacial issue: Solid electrolyte interphase stability

The formation of SEI on Li is consisted of two major steps: The chemical reactions and the electrochemical reactions. Figure 2.11 illustrate the formation process. As stated, metallic Li electrode is chemically reactive toward almost all known chemicals upon immediate contact. When the electrolyte is in contact with the Li electrode during the cell assembly, chemical reactions between the Li metal and the electrolyte take place spontaneously and instantaneously. Consequently, insoluble products are formed on the

Li metal surface to constitute a passivation layer and further chemical reactions between the metallic Li and the electrolyte are effectively suppressed by this layer, namely "primitive SEI". After the cell assembly, the cells are connected to electrochemical workstations, where they are charged/discharged at a relatively low current density for a few cycles as formation cycles. During the formation cycles, the primitive SEI is not effective to prevent the electrochemical decomposition of the electrolyte. When the Li electrode is negatively charged, electrons can diffuse to the surface of the primitive SEI on the Li electrode, which can cause cathodic decomposition of electrolyte. In addition, because the formation cycles are accompanied by significant morphological change of the Li electrode, the primitive SEI formed by chemical reactions may break and lead to the exposure of fresh Li to the electrolyte. The exposed fresh Li can further react with the electrolyte chemically and electrochemically to generate additional SEI. The composition of SEI layer highly related to the lithium salts used in the electrolyte. For example, SEIs formed in electrolytes of Li hexafluorophosphate ($LiPF_6$) in organic carbonate solvents are comprised of species such as Li semicarbonates, Li dicarbonates, LiF, Li_2CO_3, Li_2O, and small amount of Li fluorophosphate ($LiPO_xF_y$) [101].

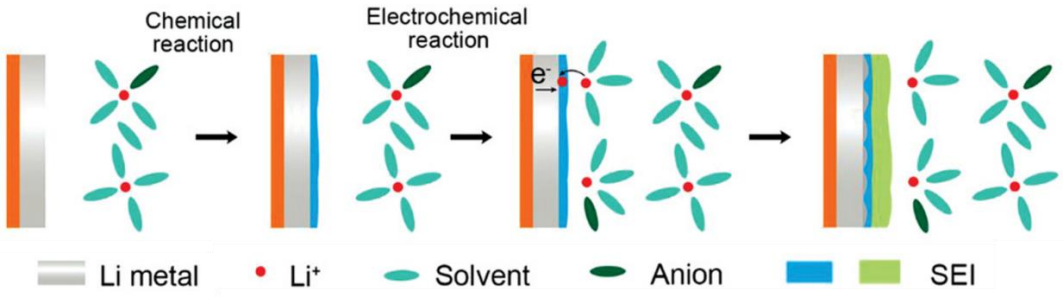

Figure 2.11. *Schematic illustration of SEI formation processes on the Li electrode [102]. Copyright 2020 John Wiley & Sons.*

The SEI can protect the lithium metal and prevent the continuous decomposition of the electrolyte. However, the infinite volume change and incessant growth of lithium dendrites are detrimental to the SEI and trigger the formation of cracks in the SEI. Due to the tip-effect, Li dendrites tend to grow through the cracks, further damaging the integrity of the SEI layer [103]. According to the mosaic model, the SEI consists of a dual-layer structure with an inner inorganic layer and an outer organic layer. Compared to the organic layer, the inorganic layer possesses higher shear modulus, which can maintain the structural integrity of the SEI layer and suppress the Li dendrite growth. Among various inorganic species in SEI, LiF has been identified as the key component due to its high chemical stability and high mechanical strength. To generate a robust

SEI layer and inhibit lithium dendrite formation/growth, forming a LiF-rich SEI layer for lithium metal anode protection is important. A stable and robust SEI layer between electrolyte and lithium metal is required to enable the intimate contact and reduce the interfacial resistance.

2.3 PEO based composite electrolyte

Poly(ethylene oxide) (PEO) is a polyether compound with a chemical structure of H–$(O–CH_2–CH_2)_n$–OH. PEO is often prepared by the cationic or anionic ring-opening polymerization of ethylene oxide depending on the catalyst type. PEO is a commercially available product with many applications from industrial manufacturing to medicine. PEO has low toxicity and thus is used in a variety of products, such as medical, chemical, biological, commercial, and industrial uses. As the polymer matrix, PEO owns strong electron donating ether oxygen (EO) groups which can provide a high donor number for Li^+, soft macromolecular backbone, good thermal stability and mechanical properties. The ion transporting mechanism of PEO based electrolyte has been depicted in Section 2.2.2. As a semi-crystalline polymer, the amorphous phase with activated chain segments in PEO (above T_g) aids ion transportation. Therefore PEO crystallization is considered to be detrimental to ion transport owing to the slowed down polymer chain dynamics upon crystallization [104-105]. The design criterion for PEO-based electrolytes is generally the suppression of PEO crystallinity to increase the percentage of the amorphous phase of PEO for ion transport.

PEO-LiX matrix

Lithium salts have a great impact on the whole ionic conductivity of PEO-LiX matrices. Some simple lithium salts, such as lithium chloride (LiCl), do not provide high ionic conductivity. Generally, the bulkier the anion of the lithium salt, the higher is the ionic conductivity. Therefore, an anion with a well delocalized negative charge and low basicity is preferred for improving the ion conductivity and playing a dominant role in the PEO–LiX matrix, as shown in Figure 2.13. Subsequently, $LiCF_3SO_3$, $LiBF_4$, $LiClO_4$, $LiPF_6$ and $LiAsF_6$, LiBOB, as well as $LiN(CF_3SO_2)_2$ (LiTFSI) have been used in PEO composite electrolyte [106-107]. Among them, LiTFSI is most widely used. The larger anions can easily dissociate in the PEO matrix and set off the free lithium cations, resulting in the increase of the ionic conductivity. The addition of a Li salt is known to reduce the crystallinity of PEO, but significantly increases the glass transition

temperature of PEO, reducing the mobility of EO segments. The melting point of PEO can be lowered using LiTFSI which shows a high salt dissociation level owing to the presence of a strong electron withdrawing group (SO_2CF_3), high flexibility of $–SO_2–N–SO_2–$ of TFSI, and excellent thermal, chemical and electrochemical stability. Thus PEO–LiTFSI complex exhibits a high ionic conductivity value [108].

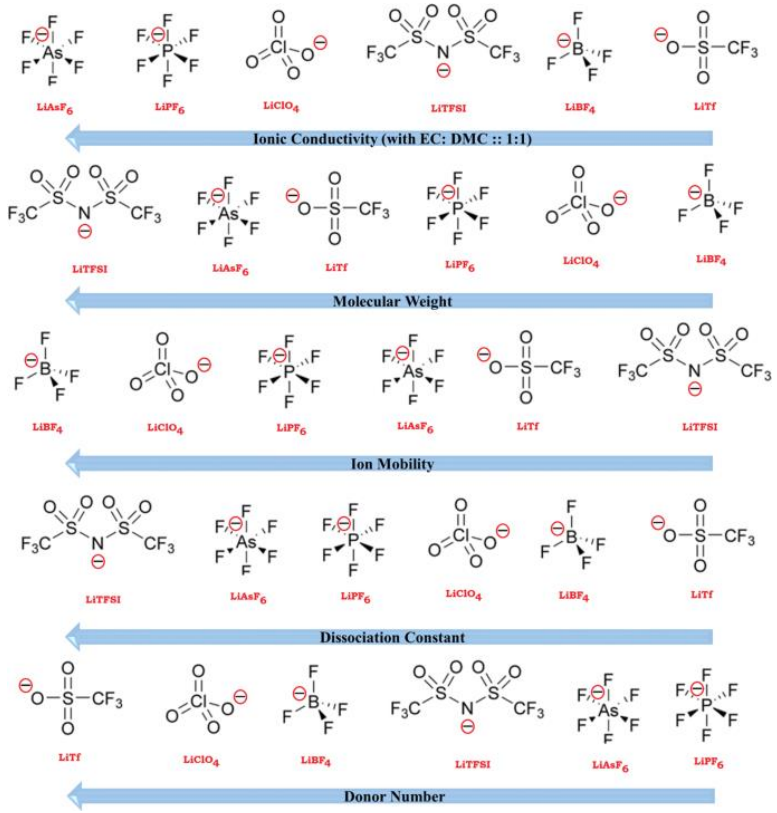

Figure 2.12. *Anion structures and comparison of different characteristics of lithium salt [109]. Copyright 2020 Springer Nature.*

It has been found that increasing the concentration of lithium salts can promote the migration of Li+. However, the high concentration of lithium salts is detrimental to the thermal movement of the PEO molecular chains, the migration of ions, the formation of films, and mechanical properties of the CPEs, resulting in a rise in T_g of the polymer and an increase in salt-ion complexation. The optimal ratio of EO/Li lies between 8 and 20. However, the inhomogeneity of the PEO-LiX composite electrolyte is a major problem, which can lead to high current density regions at the interface between the anodes, the PEO and internal short circuits (> 0.2 mA cm^{-2}) in LIBs. Addition of fillers and additives improve the physical and chemical properties of the composite electrolytes.

Plasticizer

The low ionic conductivity of the PEO–LiX system arises from the limited motion of polymer segments, which is a result of PEO's crystalline structure. Improved ionic conductivity in PEO-based electrolytes occurs primarily through ion transport within the amorphous regions of PEO. Based on the ion conduction mechanism, enhancing the mobility of PEO segments can significantly increase the ionic conductivity. However, the PEO–LiX electrolytes achieve practically useful ionic conductivity ($\sim 10^{-4}$ S cm^{-1}) only at elevated temperatures (60 – 80 °C). To address this limitation and improve room-temperature conductivity, plasticizers are commonly added. Plasticization is a well-established method to reduce crystallinity and increase the amorphous phase content in PEO–LiX electrolytes, thereby enhancing their ionic conductivity.

The widely used plasticizer in PEO composite electrolyte includes ionic liquid and organics with a small molecular weight. As a typical plasticizer, succinonitrile (SN) contains cyano groups which can dissociate alkali metal salts into ions through the coordination. Ionic liquid and conventional liquid electrolyte solvents such as $Pyr_{A,4}TFSI$, DMSO, ethylene carbonate and propylene carbonate can also act as effective plasticizers to increase the ionic conductivity of the PEO-based electrolyte and promote the interfacial lithium diffusion by a nano-wetting effect [110]. However, the liquid flammable plasticizer may sacrifice the safety, which needs further optimizations.

Ceramic filler

Adding fillers to PEO-based electrolytes to form composite polymer electrolytes is a popular research direction for batteries. The fillers not only promote the ionic conductivity and migration of Li^+, but also improve the mechanical properties of solid electrolytes and further inhibit the formation and the growth of lithium dendrites. As discussed before, inert fillers were studied at the beginning and they generally do not have Li^+ components and transport capacity. However, they can disrupt the crystalline morphology of PEO to improve the mechanical properties and the thermal stability of the electrolyte. Active fillers that contain Li^+ components and are capable of Li^+ transportation. The conductivity of the electrolyte is improved by providing an additional amount of Li^+ and broadening the electrochemical window [111-112].

The concentration, size, and shape of fillers significantly influence the performance of PEO composite electrolytes. Small inorganic nanoparticles enhance the ionic conductivity by suppressing the recrystallization of PEO molecular chains, thereby increasing the proportion of amorphous regions favorable for the ion transport.

However, an excessive concentration of fillers can lead to phase discontinuity, which negatively impacts the ionic conductivity. Lithium salts in the PEO matrix do not fully dissociate to produce free Li^+ ions; instead, a substantial number remains in the form of ion clusters of varying sizes [113]. Inorganic fillers help to mitigate this issue by inhibiting the formation of ion clusters and promoting the dissociation of lithium salts, resulting in an increased number of free Li^+ ions for conduction. Additionally, the repulsive surfaces of ceramic fillers facilitate the movement of polymer molecular chains, reducing the viscosity of the electrolyte and enhancing the transport rate of Li^+ ions. Smaller inorganic fillers are particularly effective due to their larger specific surface area, which amplifies these benefits. The shape of the fillers also plays a role; fillers with surface orientations aligned with the ideal transport pathway of Li^+ allow ions to move more efficiently with minimal disruption [114].

2.4 X-ray scattering

In this dissertation, X-ray scattering techniques are highlighted as powerful tools for analyzing the internal morphology and crystalline structures of films, delivering statistically robust insights. The fundamental principles underlying these scattering methods are introduced in Section 2.4.1. This is followed by comprehensive discussions on specific techniques, including grazing-incidence small-angle X-ray scattering (GISAXS), grazing-incidence wide-angle X-ray scattering (GIWAXS), and nanofocus wide-angle X-ray scattering (nWAXS), which are detailed in Sections 2.4.2, 2.4.3, and 2.5.4, respectively, offering an in-depth examination of their methodologies and applications.

2.4.1 Basic principles

X-ray scattering describes the interaction between an electromagnetic wave and the electrons within a material present in the sample. The scattering theory introduced in this thesis is based on elastic scattering. The electric field vector of a plane electromagnetic wave is described as a function of the position vector as [115]:

$$\vec{E}(\vec{r}) = \vec{E}_0 \exp\left(i\vec{k}_i \cdot \vec{r}\right) \tag{2.10}$$

where $\vec{E}(\vec{r})$ is the electric field vector, $\vec{r}$ is the position vector with $r = (x, y, z)$, $\vec{E}_0$ is

the polarization dependent amplitude, and $\vec{k}_i$ is the wave vector. This formulation captures the core principles of electromagnetic wave propagation through the spatial domain of a material. It clearly illustrates how the wave adapts to spatial coordinates, providing a deeper understanding of its interaction within the sample. These interactions are essential for uncovering the structural and compositional characteristics of the sample through X-Ray scattering techniques.

The modulus of the wave vector can be quantitatively described through the wave number k or the wavelength λ, as:

$$\left|\vec{k}_i\right| = k = \frac{2\pi}{\lambda} \tag{2.11}$$

This equation links the wave vector magnitude to the wave's physical properties, such as wavelength. The wave number k, defined as $2\pi/\lambda$, is key to understanding wave propagation and its interaction with the medium.

The scattering vector $\vec{q}$, plays a crucial role in the analysis of scattering phenomena, and gives the difference between the incident wave vector, $\vec{k}_i$, and the scattered wave vector, $\vec{k}_f$. This can be expressed by the equation:

$$\vec{q} = \vec{k}_f - \vec{k}_i \tag{2.12}$$

which represents the momentum transferred from incident beam to scattered beam. Since only elastic scattering is considered in this thesis, the scattering vector $\vec{q}$ represents the change in direction of the scattered beam relative to the incident beam.

The propagation of an electromagnetic wave through a medium with a position-dependent refractive index $n(\vec{r})$ is described by the following differential equation (Helmholtz equation) [115]:

$$\Delta\vec{E}(\vec{r}) + k^2 n^2(\vec{r})\vec{E}(\vec{r}) = 0 \tag{2.12}$$

The complex refractive index $n(\vec{r})$ is:

$$n(\vec{r}) = 1 - \delta(\vec{r}) + \mathrm{i}\beta(\vec{r}) \tag{2.13}$$

It depends on the dispersion $\delta(\vec{r})$ and absorption $\beta(\vec{r})$ [116]. In the case of a homogeneous medium and far away from absorption edges, one may simplify the expression of dispersion and absorption:

$$\delta(\vec{r}) = \rho(\vec{r})\frac{\lambda^2}{2\pi} \tag{2.14}$$

$$\beta(\vec{r}) = \mu(\vec{r})\frac{\lambda}{4\pi} \tag{2.15}$$

where $\rho(\vec{r})$ is the scattering length density (SLD) of the homogeneous medium and $\mu(\vec{r})$ is the linear absorption coefficient. Typically, $\delta(\vec{r})$ ranges from 10^{-5} to 10^{-6}, with values around 10^{-5} in solids and approximately 10^{-8} in air. The imaginary part $\beta(\vec{r})$ is generally smaller than $\delta(\vec{r})$, which results in the refractive index of X-rays being slightly less than 1. The scattering contrast Λ between two phases of different optical density is defined as:

$$\Lambda = (\delta_1 - \delta_2)^2 + (\beta_1 - \beta_2)^2 \tag{2.16}$$

The Scattering Length Density (SLD) is a crucial measure that indicates a material's ability to diffract or scatter incoming radiation. It is essential for revealing differences in scattering properties both within different regions of a single material and between various materials. The SLD for the X-ray measurement is defined by the formula:

$$\text{SLD} = \frac{n_e \rho_e N_A r_e}{M_w} \tag{2.16}$$

where n_e is the total number of electrons per molecule, ρ_e is the electron density, N_A is the Avogadro constant, and M_w denotes the molar mass of the material. This formulation underscores the relationship between the SLD and fundamental physical constants, as well as the material-specific properties such as electron density and molar mass.

At incidence angle below the critical angle ($\alpha_i < \alpha_c$), total external reflection occurs and only near-surface related information is obtained. In order to investigate the inner structure, an incidence angle above the critical angle has to be applied. In hard X-rays ($E > 5$ keV), where the refractive index n < 1, the X-ray beam undergoes reflection at the juncture between a medium of higher density like air or vacuum, and a medium of lower density like water. This reflective behavior adheres to Snell's law:

$$\cos(\alpha_i) = \frac{n}{n_0}\cos(\alpha_t) \tag{2.17}$$

where α_t is the refraction angle, and in the case of total reflection, $\alpha_t = 0$. The

incidence angle, denoted by α_i, is defined as the angle formed between an incoming wave and the boundary separating two distinct media.

When $\alpha_i = \alpha_c$, and $\alpha_t = 0$, assuming air is the incident medium where $n_0 = 1$, the equation is accordingly simplified can be written as:

$$\cos(\alpha_c) = n = 1 - \frac{\lambda^2}{2\pi} r_e \rho_e = 1 - \frac{\lambda^2}{2\pi} \mathrm{SLD} \tag{2.18}$$

When applying the small angle approximation according to the Taylor series:

$$\cos(\alpha_c) \approx 1 - \frac{\alpha_c^2}{2} \tag{2.19}$$

An approximation for the critical angle in terms of the SLD is then derived:

$$\alpha_c \approx \sqrt{2\delta} = \lambda \sqrt{\frac{\mathrm{SLD}}{\pi}} \tag{2.20}$$

When the incident angle α_i is less than the critical angle α_c, total external reflection takes place, causing the transmitted wave to weaken significantly. The X-ray then travels along the surface of the film with minimal penetration, which results in an attenuated wave. This region is referred to as the attenuation zone, as it provides structural information primarily about the near-surface region of the film. However, when α_i exceeds α_c, it allows for the acquisition of additional structural information from the bulk of the film.

2.4.2 Grazing-incidence small-angle X-ray scattering

Grazing-incidence small-angle X-ray scattering (GISAXS) offers a profound method to probe both the surface and inner morphologies of thin films. The reflection scattering geometry offers morphology information about films and surfaces, providing high statistical validity that accurately represents the average film structure. In GISAXS, a very shallow angle of incidence, typically $\alpha_i \ll 1°$, is used. Therefore, GISAXS can provide a strong signal from thin film due to the footprint effect of the grazing incident beam, thereby enhancing the interaction volume. The footprint length l in the direction of the beam is calculated by the formula:

$$l = \frac{h}{\tan(\alpha_i)} \tag{2.21}$$

where h is the size incident beam. For example, with an incidence angle of $\alpha_i = 0.4°$ and an X-ray beam size of 20 × 30 μm^2, the illumination area will be expanded by more than two orders of magnitude (1.5 × 10^3 μm^2). This amplification allows for detailed structural analysis at large length scales.

The basic scattering geometry for GISAXS is shown in Figure 2.14. The sample surface is defined as (x, y) plane, and x defined as the direction along the incident X-ray beam (α_i). Therefore, y is defined as the direction perpendicular to the incident beam direction. The $Z\ axis$ is introduced to build a (x, z) plane, which represent the scattering plane. As mentioned in Section 2.4.1, the specular scattering (S point) appears when $\alpha_i = \alpha_f$. The Yoneda scattering (Y point) occurs when $\alpha_i = \alpha_c$.

X-rays scatter in various directions, defined by the wave vector $\vec{k}_f$, with the scattering characterized by angles ψ (azimuthal angle) and α_f (scattered exit angle) relative to the surface. The scattering vector $\vec{q}$, representing the change in momentum of the X-rays due to scattering, is given by [117]:

$$\vec{q} = (q_x, q_y, q_z) = \vec{k}_f - \vec{k}_i = \frac{2\pi}{\lambda}\begin{pmatrix} \cos(\alpha_f)\cos(\psi) - \cos(\alpha_i) \\ \cos(\alpha_f)\sin(\psi) \\ \sin(\alpha_f) + \sin(\alpha_i) \end{pmatrix} \tag{2.22}$$

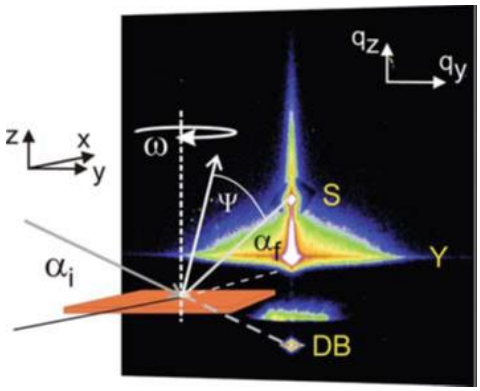

Figure 2.13. *Illustration of GISAXS geometry. Main characteristic features are the specular peak (denoted S), the Yoneda peak (denoted Y), and the direct beam (denoted DB). The incident angle is denoted α_i, the exit angle α_f, and the azimuthal angle ψ [118]. Copyright 2009 Springer, Berlin, Heidelberg.*

With grazing-incident geometry, additional reflections have to be considered, and the distorted wave born approximation (DWBA) is introduced as first order perturbation theory [119]. These perturbations cause multiple additional reflection events at the surface, as shown in Figure 2.14. The four terms involved are associated to different scattering events, including scattering (Term 1), reflection before scattering (Term 2), reflection after scattering (Term 3). Additionally, DWBA incorporates more complex interactions, including sequences of reflection at an interface, scattering by the object, and further reflections (Term 4). These waves interfere giving rise to the following form factors:

$$F_{DWBA}(q_{xy}) = F(q_{xy}, q_z)$$

$$+r(\alpha_f)F(q_{xy}, q_z) + r(\alpha_i)F(q_{xy}, -q_z) + r(\alpha_i)r(\alpha_f)F(q_{xy}, -q_z) \quad (2.23)$$

Therefore, the total cross section of scattering is denoted as [120]:

$$\frac{d\sigma}{d\Omega} = \frac{A\pi^2}{\lambda^4}|\Delta|^2|T_i|^2|T_f|^2P(\vec{q}) \quad (2.24)$$

where A is the illumination area. T is the Fresnel transmission coefficients for incident and scattered beam and P is the scattering factor. $|\Delta|^2 = \delta^2 + \beta^2$ is the scattering contrast function.

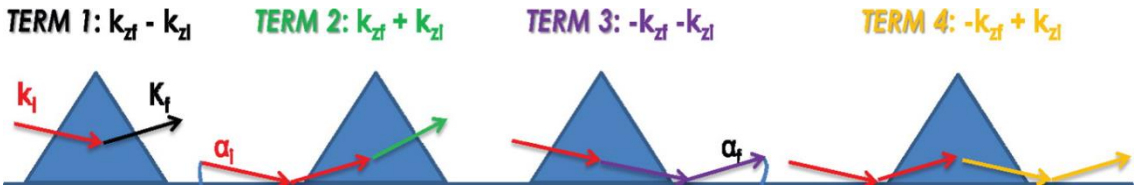

Figure 2.14. *Illustration scattering and reflection events taken into account in DWBA [121]. Copyright 2012 John Willey& Sons.*

Scattering intensity is heavily influenced by Fresnel transmissivity, which reaches its peak at the critical angle of the material. High scattering intensity occurs when the beam exits at an angle equal to the medium's critical angle. Since real scattering objects vary in size around an average value, several approximations are required. For polydisperse domains, an effective average form factor is introduced using either the local monodisperse approximation (LMA) or the decoupling approximation (DA). In LMA, The scattering cross section results from an incoherent sum of scattering from

monodisperse domains. Thus, kind and location of all scattering centers are strongly correlated. In contrast, DA assume that the size and shape of particles and their relative location are not correlated. In this thesis, a model based on LMA in combination with the effective interface approximation (EIA) is used to describe GISAXS data. Hence, the diffuse scattering according to DWBA, LMA and EIAcan be expressed as [122-123]:

$$P(\vec{q}) \propto N \cdot \langle |F(\vec{q}, R_i)|^2 \rangle \cdot S(\vec{q}, R_i) \tag{2.25}$$

where N is the number of scattering domains, $F(\vec{q})$ is the domain shape and size as the Fourier transform of their electron density (form factor), and $S(\vec{q})$ is the domain arrangement (structure factor).

2.4.3 Grazing-incidence wide-angle X-ray scattering

Grazing incidence wide-angle X-ray scattering (GIWAXS) is performed with the same scattering geometry as GISAXS but with a reduced sample-to-detector distance (SDD) down to hundreds of millimeters, as shown in Figure 2.15. This adjustment in the experimental setup enables the detection of scattered signals at large exit angles [124]. Such a configuration is crucial for accessing structural data at the sub-nanometer level, offering insights into the atomic arrangement within the material.

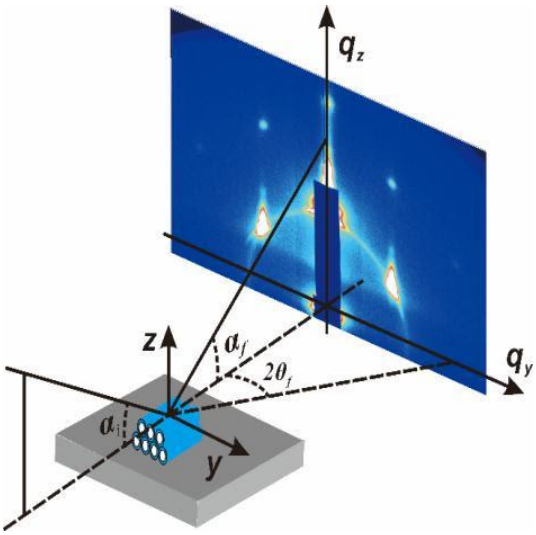

Figure 2.15. *Illustration of the GIWAXS geometry.*

Figure 2.16 illustrate the Bragg and Laue condition. The Laue condition, which is the reciprocal space counterpart of the Bragg condition in real space (Figure 2.16a),

governs the measurement of lattice spacing d_{hkl}. On the other hand, as shown in Figure 2.16b, the reciprocal lattice, which is the Fourier transform of the real-space crystal lattice, contains all wave vectors that can produce diffraction.

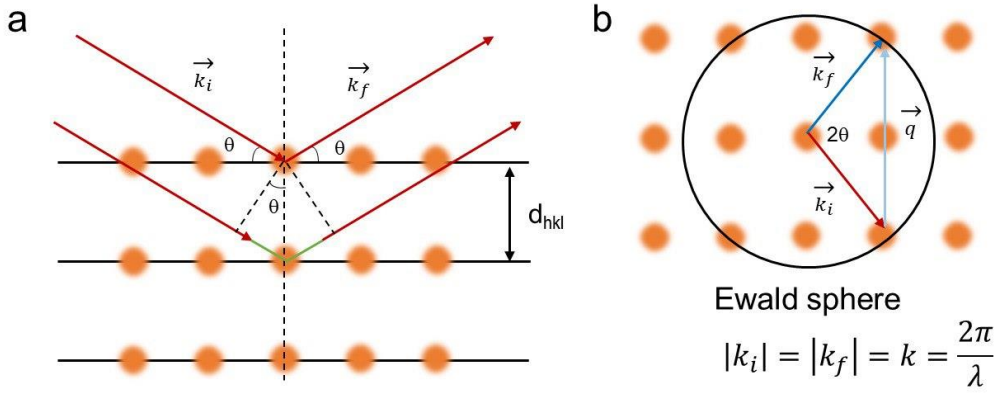

Figure 2.16. *Schematic illustration of the (a) real space and (b) Ewald sphere. Diffraction patterns occur when the Ewald sphere touches a reciprocal lattice point.*

A scattering signal arises when the Laue condition is fulfilled, indicating that the crystal lattice has diffracted the incident wave vector $\vec{k}_i$ into the final wave vector $\vec{k}_f$. In real space, the incident beam interacts with the scatterer, producing a reflection. The set of all possible incident and scattered wave vectors ($\vec{k}_i$ and $\vec{k}_f$) forms a geometric construct known as the Ewald sphere. The surface of the Ewald sphere represents the geometrical construct used in scattering experiments. Its intersections with reciprocal lattice points appear as reflections on the detector. Consequently, GIWAXS directly probes the reciprocal lattice. Constructive interference occurs when the path difference between the interfering X-rays equals a multiple of the wavelength λ, at a specific angle θ:

$$d_{hkl} = \frac{n\lambda}{2\sin\theta} \tag{2.26}$$

The Laue condition generalizes Bragg's law to three dimensions, offering a criterion for constructive interference that occurs when the change in the wave vector $\Delta\vec{k}$ is equivalent to a reciprocal lattice vector $\vec{Q}$ represented as:

$$\Delta\vec{k} = \vec{k}_f - \vec{k}_i = \vec{q} = \vec{Q} \tag{2.27}$$

and

$$\vec{Q} = h\vec{a}_1 + k\vec{a}_2 + l\vec{a}_3 \tag{2.38}$$

where $\vec{a}_1$, $\vec{a}_2$, and $\vec{a}_3$ are the reciprocal lattice vectors, and h, k, l are the Miller indices corresponding to the planes in the crystal lattice.

In GIWAXS measurement of multiply layer samples, the incident angle various, and by comparing with critical angle, different information can be obtained, as illustrated in Figure 2.17 [118]:

i. $\alpha_i < \alpha_{c(surface\ layer)}$, the crystalline structure information of surface-near region;

ii. $\alpha_{c(surface\ layer)} < \alpha_i < \alpha_{c(bottom\ layer)}$, the crystalline structure information of the whole surface layer;

iii. $\alpha_{c(bottom\ layer)} < \alpha_i$, the crystalline structure information of both surface layer and bottom layer.

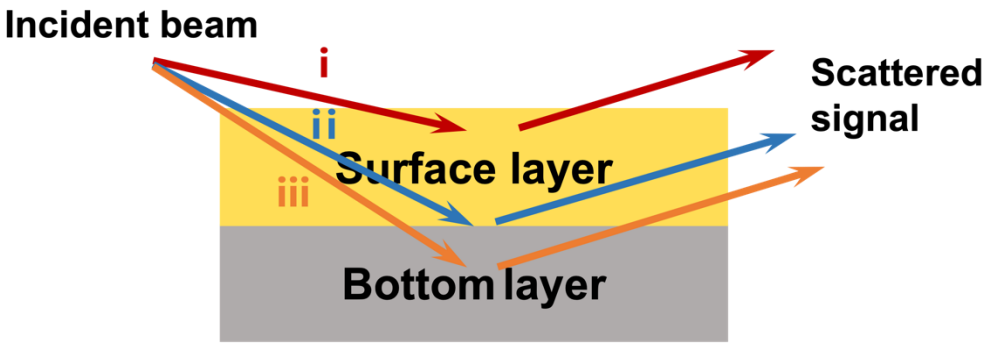

Figure 2.17. *Illustration of the GIWAXS signal obtained from multiply layer sample with various incident angle.*

The crystal orientation information can also be extracted when analyzing GIWAXS data. In semi-crystalline polymers, such as PEO, the polymer does not achieve complete crystallization. As a result, portions of the polymer chains remain amorphous and are not incorporated into the crystalline structure. The formed crystals can organize into larger hierarchical structures, such as lamellae or spherulites [125]. Figure 2.18 gives four typical types of crystal orientations. For a face-on orientation, where lamellae are vertically stacked and well-ordered without rotational disorder, the resulting Bragg peaks are predominantly one-dimensional and align along the q_z axis, as shown in Figure 2.18a. Similarly, if both face-on and edge-on orientated lamellae are present, the scattering signal will be observed along the q_z and the q_r axis (Figure 2.18b). In a more textured film with domains exhibiting an angular distribution around the horizontal alignment, the Bragg peaks in the vertical direction become broader (Figure 2.18c). As

shown in Figure 2.18d, if the film has a random orientational order among the crystallites, the Bragg peaks diffuse into Debye-Scherrer-like rings.

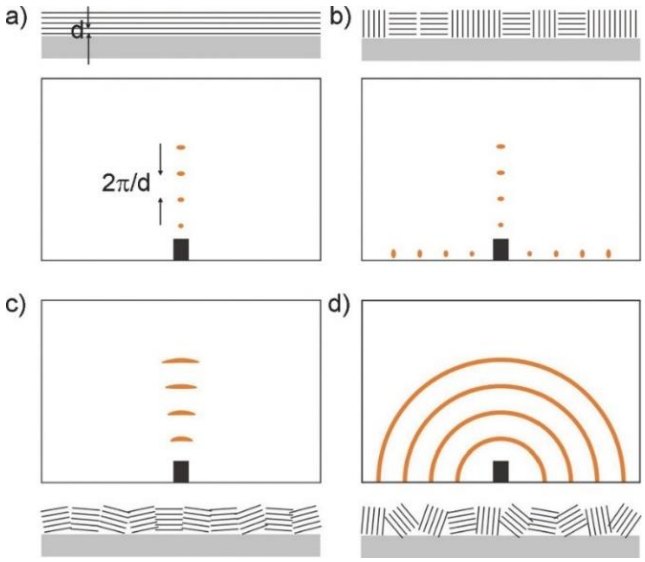

Figure 2.18. *Sketch of different orientations in a thin film and the corresponding GIWAXS scattering signal: (a) vertical stacking, (b) vertical and horizontal stacking, (c) oriented domains, and (d) full rotational disorder of crystallites [126]. Copyright 2014 John Wiley & Sons.*

Through GIWAXS, these Bragg peaks enable the determination of key crystallographic parameters such as lattice spacing, crystallite size, and orientation. Additionally, the degree of crystallinity within the sample, which correlates with the intensity of the scattered signal, can be assessed.

2.4.4 Nano-focus wide-angle X-ray scattering

Nano-focus wide-angle X-ray scattering (nWAXS) is a valuable tool for characterizing the crystallinity, structural order, and phase composition of materials [127]. It provides detailed insights into both crystalline and amorphous materials and is essential for understanding short- to medium-range order in a wide range of substances, from polymers to nanomaterials. nWAXS is similar to GIWAXS in providing crystalline structure information, but it uses a transmission geometry instead. nWAXS provides valuable information on the atomic or molecular arrangement in the material, especially the short-range order, and is widely used in various fields. nWAXS involves directing X-rays onto a sample and measuring the scattering pattern that results from the

interaction between the X-rays and the sample. The angle at which the X-rays scatter, along with their intensity, provides insights into the material's structure.

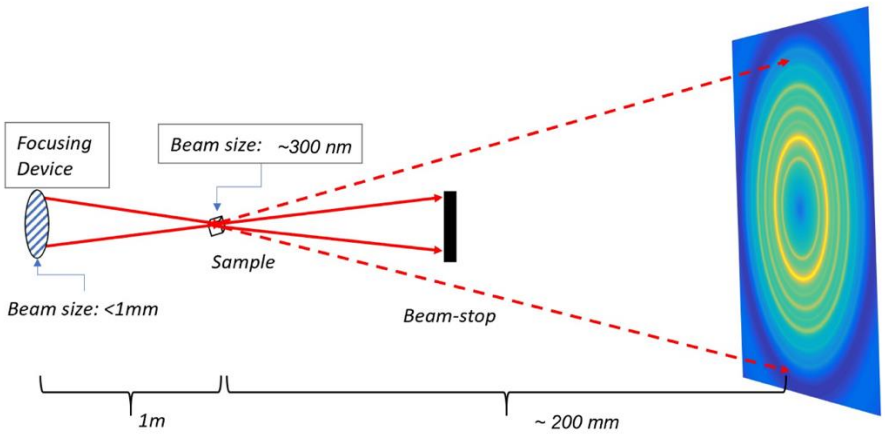

Figure 2.19. *Illustration of transmission scattering geometry of nWAXS.*

Figure 2.19 illustrate the scattering geometry of nWAXS, the SDD of nWAXS is hundreds of milometers, and beam size normally smaller than 500 nm. Nanofocused Wide-Angle X-ray Scattering (nWAXS) performed in transmission geometry, utilizing a nanoscale X-ray beam, enables the probing of local structural information with high spatial resolution at varying depths within a sample. This capability allows for precise mapping of structural variations across different regions of a material. By conducting scanning measurements, one can generate detailed structural maps, making nWAXS an invaluable tool for in situ and operando studies. These measurements provide real-time insights into dynamic processes, such as phase transitions, strain evolution, crystallization, or chemical reactions, under actual operating conditions. This makes nWAXS particularly useful for applications in materials science, especially battery research, where understanding nanoscale structural heterogeneity is crucial. The scattering pattern in WAXS corresponds to the material's reciprocal space, and features like diffraction peaks can be analyzed to determine the arrangement and periodicity of the atoms or molecules within the material. Same as GIWAXS, the observed scattering pattern corresponds to points in reciprocal space, which is the Fourier transform of the real-space lattice. The reciprocal lattice is a mathematical representation of the periodicity of the crystal. Each point in the reciprocal lattice corresponds to a set of crystal planes in real space, defined by the Miller indices (h, k, l) [128].

3 Characterization and analytical methods

This chapter describes various techniques used in characterizing solid composite electrolytes. Section 3.1 covers structure characterization, including both real- and reciprocal-space imaging methods for investigating the structures. Thermal properties characterization methods are elaborated in Section 3.2. Spectroscopic characterization techniques are detailed in Section 3.3. Finally, Section 3.3 discusses the principles of potentiostatic electrochemical impendence spectroscopy (PEIS), cyclic voltammetry (CV), liner sweep voltammetry (LSV), chronoamperometry (CA), and galvanostaic charge-discharge (GCD) cycling measurements.

3.1 Structural characterizations

3.1.1 Scanning electron microscopy

Scanning electron microscopy (SEM) is one of the most versatile techniques available for the examination and analysis of the microstructure morphology and chemical composition of the top 1 μm of specimen. In the SEM technique, electrons are used instead of light in a microscope because they have much shorter wavelengths than visible light, enabling far higher resolution. This allows electron microscopes to reveal nanoscale details of a sample surface or structure that are impossible to resolve with light microscopes due to the diffraction limit of light. Therefore, the resolution of SEM instruments can range from < 1 nanometer up to several nanometers.

The schematic and operational principles of a typical SEM instrument are depicted in Figure 3.1. The SEM starts with an electron source (e.g., tungsten filament, LaB_6, or Field Emission Gun) that generates a beam of high-energy electrons. These electrons are accelerated and pass through a series of electromagnetic lenses. As electrons pass

through this magnetic field, off-axis electrons are bent toward the optic axis which causes a beam crossover to form at a specified distance from the lens. This process demagnifies the size of the electron source (~50 µm for a tungsten filament) down to the final required spot size (1–100 nm). Scanning coils deflect the beam in a raster pattern across the sample's surface, enabling detailed imaging of specific regions. A high-vacuum environment, which allows electron travel without scattering by the air, is needed.

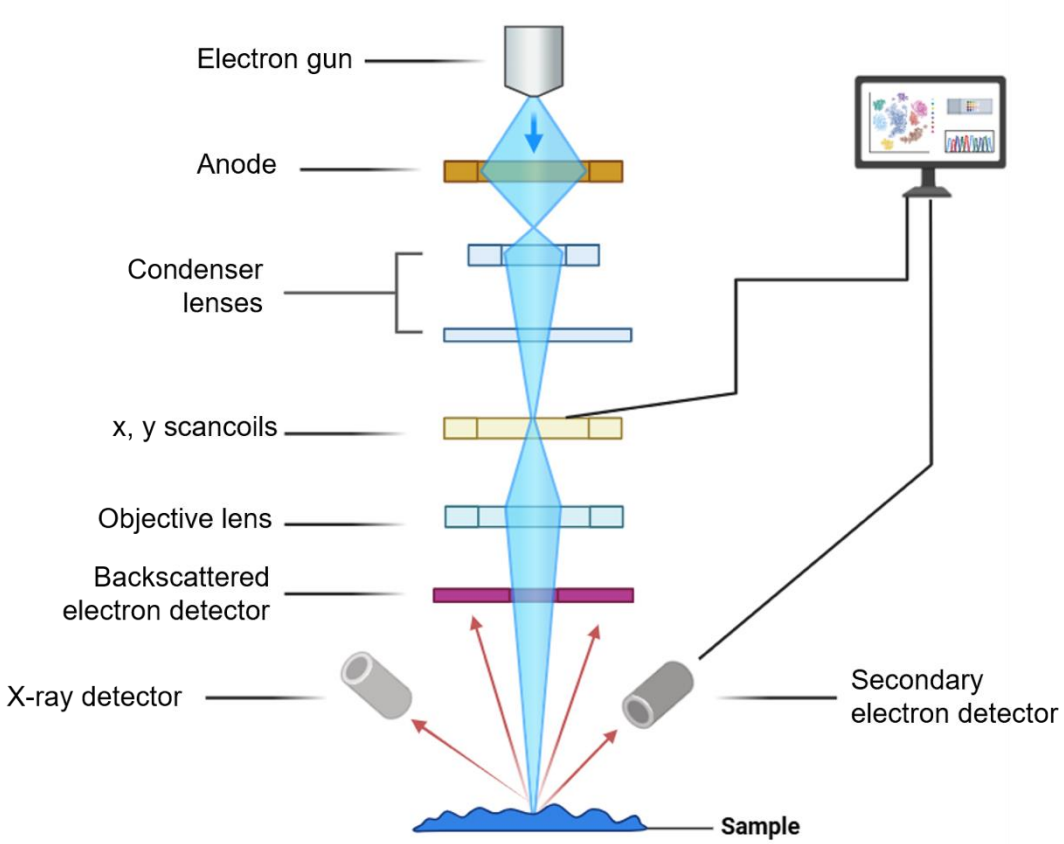

Figure 3.1. *Schematic illustration of a Scanning Electron Microscope (SEM). This figure is produced by biorender.com*

Various detectors are used in SEM. When the electron beam hits the surface of the sample, interaction happened, generating different signals [129]. The most used signals in the SEM are secondary electrons (SE), backscattered electrons (BSE), and characteristic X-rays, along with their corresponding detectors. SE signals are primarily used for topographical images because they are generated closer to the surface of the sample. Images collected with secondary electrons will also possess the best lateral resolution due to the relatively small interaction volume that is approximately the size

of the beam diameter. BSE signal originates from below the surface of the sample; therefore, the resolution of BSE image is worse compared to an image acquired with an SED. Using a BSD allows for lower vacuum levels, reducing sample preparation requirements and minimizing beam damage. Characteristic X-rays are emitted when the electron beam displaces an inner shell electron (that belongs to an atom in the sample) that is replaced by an outer shell electron. Because each element has a unique energy difference between outer and inner electron shells, the X-rays that are detected are at specific energies that can be correlated with an elemental identification. The characteristic X-ray signal can be collected to the X-ray detector and used to analyze the elemental composition of the sample through energy dispersive spectroscopy (EDS). It is a fast, accurate, and non-destructive method for identifying elemental composition on the micron scale.

All SEM measurements conducted in this thesis utilize a SEM EVO 15 instrument from Carl Zeiss, operated with the SmartSEM software. The instrument is housed at the Walter-Schottky-Institut/ZNN of TU Munich. For measurement parameters, the electron beam accelerating energy is 20 keV with a working distance of 11 mm. All obtained SEM images are analyzed with the ImageJ software.

3.1.2 Grazing incidence small-angle X-ray scattering

Grazing incidence small-angle X-ray scattering (GISAXS) stands as a powerful and specialized X-ray scattering method, allowing for the exploration of surface and buried structures across a wide range of length scales, spanning from nanometers to micrometers. In the present thesis, GISAXS is used for investigating the structures of PEO based composite electrolyte during the voltage sweepd. The GISAXS measurements conducted in this study are executed at the MiNaXS beamline P03, situated at the PETRA III storage ring within DESY (Hamburg, Germany).

Beamline operando setup

In the context of the operando GISAXS measurement outlined in Chapter 5, the incident X-ray photon energy is set at 12.9 keV, corresponding to a wavelength of 0.96 Å. The sample-to-detector distance (SDD) is maintained at 4090 mm. The 2D GISAXS data are captured utilizing a Pilatus 1M detector (Dectris Ltd., Switzerland), with each pixel measuring 172 µm × 172 µm. In terms of incident angle (α_i) choosing, the deep penetration depth is needed to obtain more information from the electrolyte. A moderate footprint has to be considered to avoid background noise. Therefore, the incident angle is set as 0.4°. The background noise is excluded by utilizing high beam energy and high

incident angle. To mitigate the risk of X-ray-induced damage to the sample, a beam-damage scan is conducted. As is shown in Figure 3.2, the incident X-ray beam hit on the sample in operando chamber and the scattering beam was reach to the GISAXS detector after traveling through the flight tube. The measurement is conducted at the P03/MiNaXS beamline of the PETRA III storage ring at DESY.

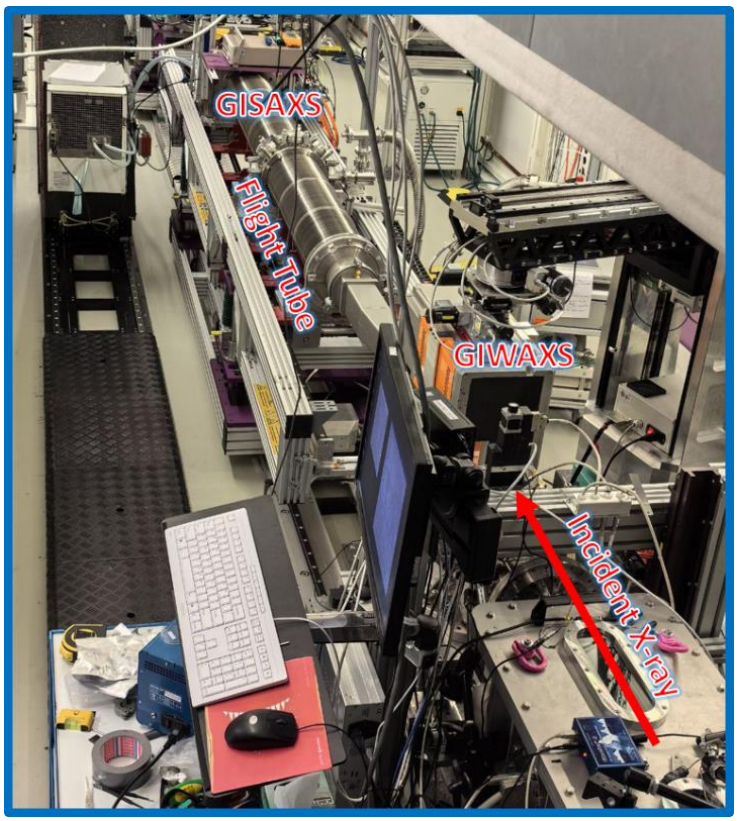

Figure 3.2. *Photograph of operando GISAXS/GIWAXS setup at the P03/MiNaXS beamline of the PETRA III storage ring at DESY, Hamburg.*

Operando chamber

Figure 3.3 shows the operando chamber in side view, back view, and top view. The operando chamber consists of a homemade cell with two attached Kapton windows on both the front and backside and connected to a VMP150 Biologic electrochemical workstation. A gas tube is connected to the chamber and the Argon gas bottle to assure the inherent ambient conditions, maintaining a gas flow of approximately 1 mbar. By adding a temperature control circulator (Julabo GmBH), the temperature can be adjusted from room temperature to up 100 °C. In the operando chamber, two clamps are used to fix the sample, and also act as current collect channel. A Li||Cu cell was used to investigate the lithium deposition process. Copper sheet was used as the substrate

and the electrolyte was deposited on it to realize a flat surface. In order to detect the changes within the electrolyte, a slit was made on the lithium chip and the stainless steel current collector. The cell was connected to the electrochemical workstation to record the cyclic voltammetry curve from 2.5 to 0 V with a scan rate of 5 mV/s.

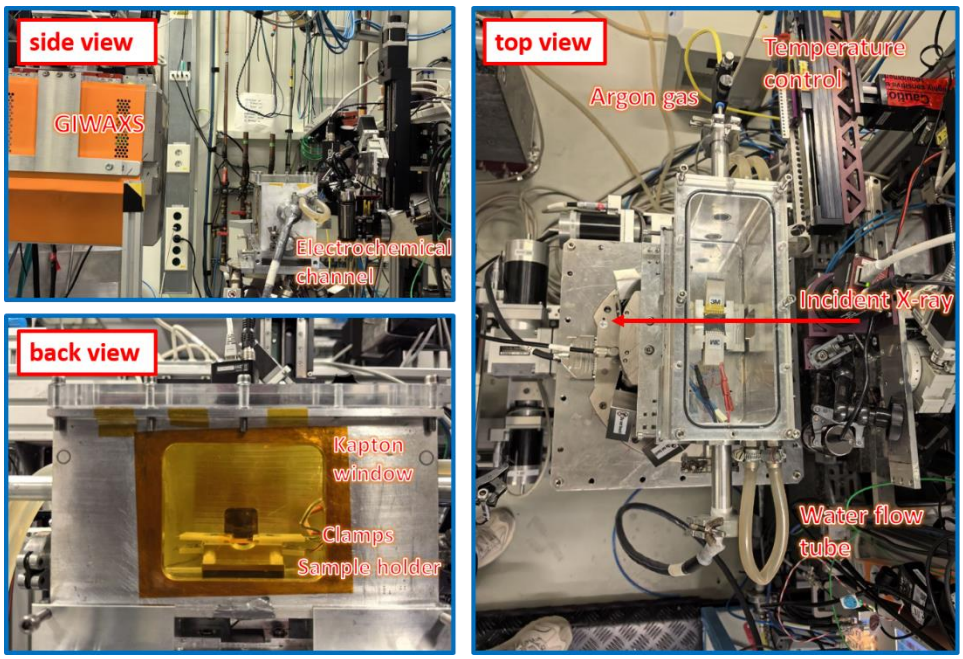

Figure 3.3. *Photograph of operando GISAXS/GIWAXS sample chamber at the P03/MiNaXS beamline of the PETRA III storage ring at DESY, Hamburg.*

Data treatment

For quantitative analysis of the GISAXS data, horizontal line cuts are conducted at the material-specific Yoneda peak region, using the DPDAK software. These line cuts contain valuable information regarding the lateral structure of the examined film. To extract characteristic length scales of the structure, these cuts are modeled using the distorted wave born approximation (DWBA), incorporating the local monodisperse approximation (LMA), and a 1D paracrystalline lattice.

In this thesis (Chapter 5), the materials used are LiTFSI, PEO, and Al_2O_3, and more detail will be discussed in Chapter 4. The theoretical critical angles for LiTFSI (0.1078°), PEO (0.1021°), and Al_2O_3 (0.1025°) at the abovementioned X-ray energy were calculated by the SLD python package. Analysis of GISAXS the data was performed via DPDAK software [130]. The Yoneda peak position was identified via the vertical line cuts of the 2D GISAXS data. Horizontal line cuts were taken at the Yoneda region to obtain the structural information. The horizontal line cut data was modeled in

the framework of DWBA using the LMA model [117-131].

Figure 3.4 depicts an illustrative example of a horizontal line cut extracted from the 2D GISAXS data of the PEO composite electrolyte. I assumed that the scattering objects possessed a cylindrical shape with a radius (R) and with a Gaussian distribution of sizes. A 1-dimensional para-crystalline model was applied to extract the distances between neighboring objects (center-to-center distance D). This analysis will be particularly beneficial for the investigation into the buried morphology evolution of PEO composite electrolyte with voltage sweep and will be further elaborated upon in Chapter 5.

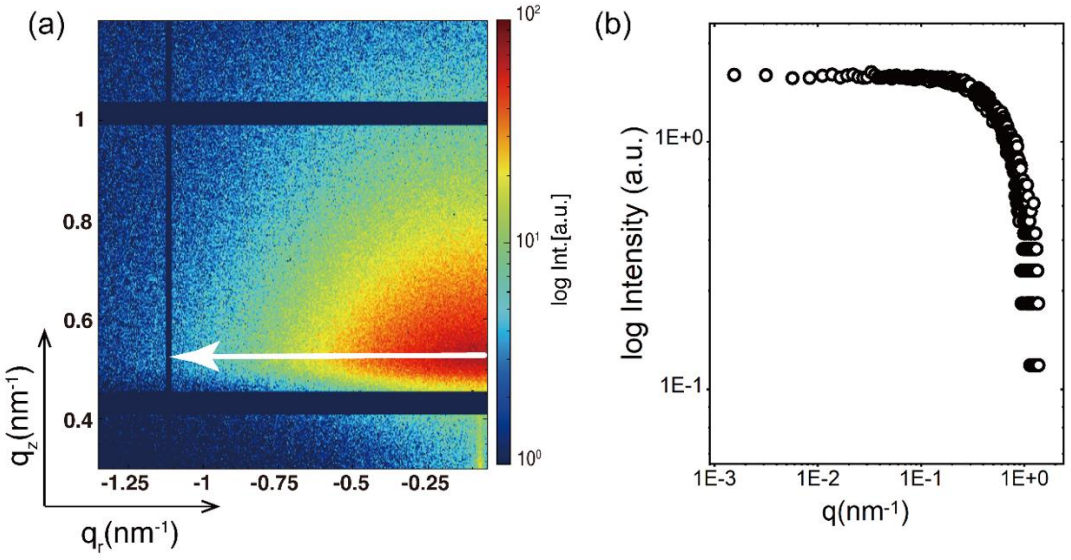

Figure 3.4. *Example of GISAXS data modeling of a horizontal line cut of the 2D GISAXS data: (a) Example 2D GISAXS data with the white arrow representing the cut direction and (b) resulting horizontal line cut profile [19]. Copyright 2024 by the authors. Published by American Chemical Society.*

3.1.3 Grazing incidence wide-angle X-ray scattering

Grazing incidence wide-angle X-ray scattering (GIWAXS) is a powerful tool for investigating the atomic-scale structure of materials. It is particularly effective in examining the crystallinity, lattice spacings, and lattice orientation distributions of both single-crystal and poly-crystalline samples. In this thesis, operando GIWAXS measurements are conducted at the P03/MiNaXS beamline of the PETRA III storage ring at DESY. Notably, due to differences in SDD between GIWAXS and GISAXS setups, simultaneous operando GIWAXS and GISAXS measurements can be carried

out during the CV sweep on Li||Cu cells, and the setup is shown on Figure 3.2. Consequently, the photon energy of the X-ray beam and the incident angle (α_i) remain consistent with those of the operando GISAXS measurements, as they are conducted concurrently. In the context of the operando GISAXS measurement outlined in Chapter 5, the incident X-ray photon energy is set at 12.9 keV, corresponding to a wavelength of 0.96 Å. The SDD of operando GIWAXS measurements in Chapter 5 are set at 293.15 mm, and the corresponding 2D data is captured using a Lambda 9M detector (X-Spectrum GmbH, Germany) with a pixel size of 55 µm × 55 µm.

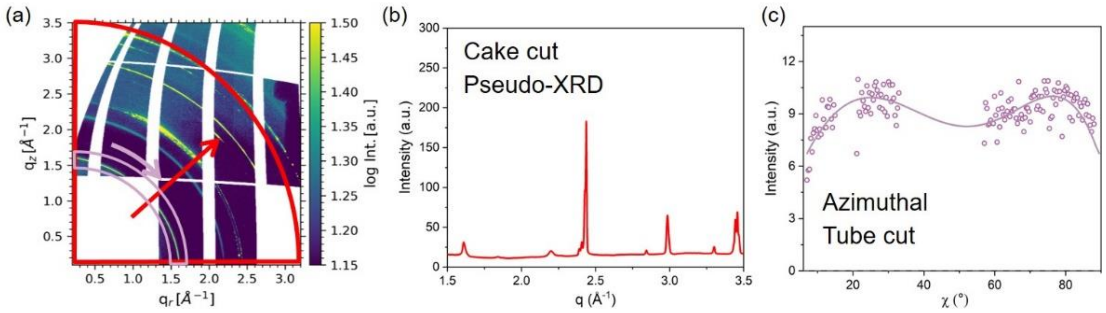

Figure 3.5. *Examples of "cuts" in GIWAXS data analysis. (a) Exampled 2D GIWAXS image, with the red area represent cake cut area and the arrow represent the cut direction; the purple ring area represent the azimuthal tube cut, and the arrow represent the cut direction. (b) Pseudo-XRD profile obtained from the cake cut of (a). (c) Orientation information obtained from the azimuthal tube cut of (a) [19]. Copyright 2024 by the authors. Published by American Chemical Society.*

The collected GIWAXS data were further processed by the python-based heuristic tool INSIGHT [132]. The correction of the SDD was realized by calibrating the (111) Cu Bragg reflex to 3.0103 $Å^{-1}$ (2 theta = 43.297°), and the background subtraction was done by INSIGHT. Figure 3.5 gives the example on how to conduct the abovementioned cuts in 2D GIWAXS data. Cake cuts of the 2D GIWAXS data for pseudo-XRD were done with the limits of χ = [0, 90°] and q = [1.49, 4.01] $Å^{-1}$. The cut results are plotted in a q versus intensity curve, namely pseudo-xrd cut. By analyzing the pseudo-XRD cut, the crystallinity, lattice distance, and crystal size can be obtained. Moreover, azimuth tube cuts were conducted with the limits of χ = [0, 90°] and q = [1.55, 1.65] $Å^{-1}$, and plotted in a χ versus intensity curve, as shown in Figure 3.5c. By analyzing the azimuth tube cut, the preferred crystallite orientation information can be obtained. The analyzing results and discussions are depicted in Chapter 5.

3.1.4 Nano-focus wide-angle X-ray scattering

Nano-focus wide-angle X-ray scattering (nWAXS), which has similar scattering geometry as GIWAXS (nWAXS is in transmission mode), is a powerful tool for investigating the crystalline structure of materials with nanometer size X-ray beam. Unlike GIWAXS, nWAXS using transmittance X-ray beam, which offers the opportunity to mapping the structure evolution while batteries cycling. In this thesis, operando nWAXS measurements are conducted at the nanofocus endstation, P03/MiNaXS beamline of the PETRA III storage ring at DESY (Hamburg, Germany).

Beamline operando setup

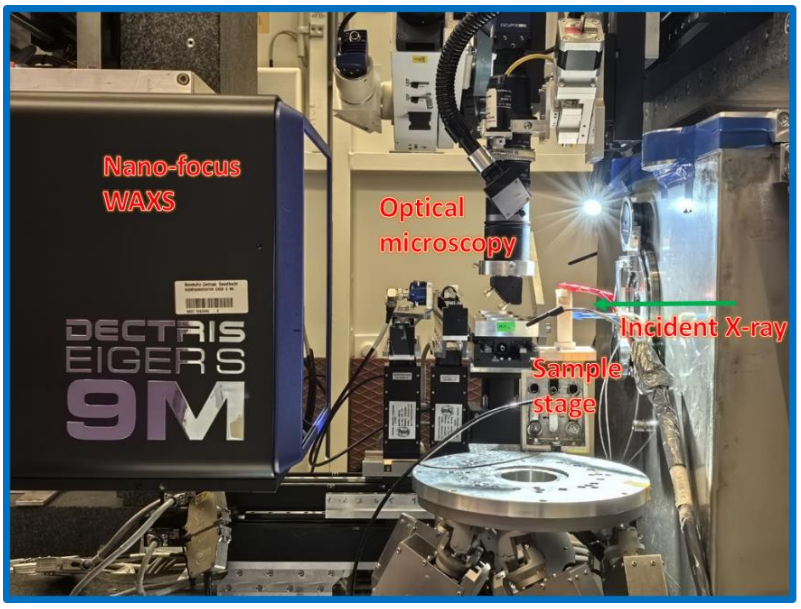

Figure 3.6. *Photograph of operando nWAXS setup at the P03/MiNaXS beamline of the PETRA III storage ring at DESY, Hamburg.*

The *operando* setup is shown in Figure 3.6. The incident X-ray beam with a beam energy of 12.62 keV into the sample, and scattering signal is captured by the Dectris Eigers 9M detector (Detrics AG, Switzerland) with a pixel size of 75 μm × 75 μm. The SDD of *operando* nWAXS measurements is set at 220 mm, and the nanobeam size is 350 nm × 330 nm (H × V). An optical microscopy is placed in front of the sample position for beam focusing and moves out when the measurement starts. The whole nWAXS scan area was recorded in 4 × 16 frames with 0.5 μm step size, which corresponds to the scanned sample area of 2 μm length ×8 μm height on the sample.

Operando chamber

The operando chamber for the nWAXS measurement in this thesis is designed by Fabian A. C. Apfelbeck and Dr. Gilles E. Wittmann. The operando setup consisted of a homemade battery cell with two attached Kapton windows on both the front and backside, which was suitable for X-ray transmission measurements at large-scale facilities, and the electrochemical characterization with a VMP150 Biologic electrochemical workstation. A Li||Li symmetric cell was used to observe the lithium dendrite growth and SEI layer formation process. Two long screws were used to fix the sandwiched sample and to connect with the VMP150 Biologic electrochemical workstation. The operando cells were assembled and sealed in Ar-filled glovebox. Two galvanostatic charge/discharge cycling were applied on each sample with a current density of 0.05 mA cm^{-2}. The scan area and the operando chamber are shown in Figure 3.7.

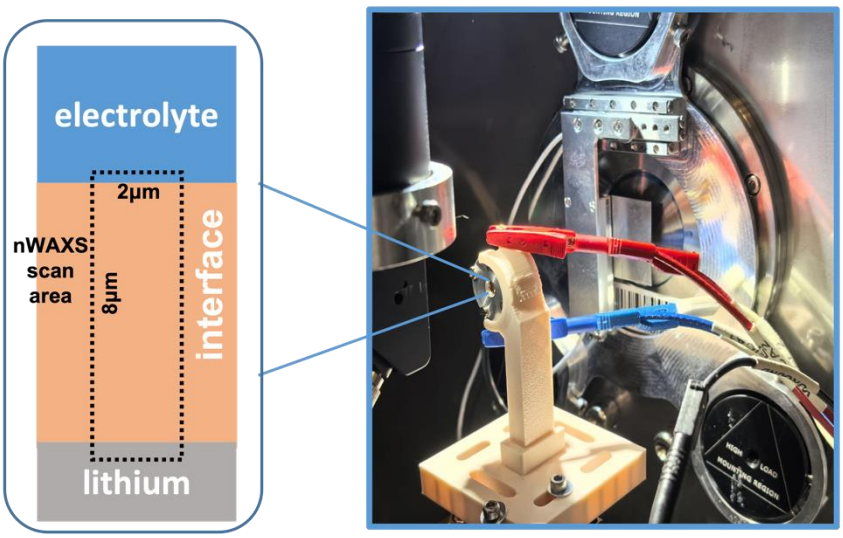

Figure 3.7. *Photograph of operando nWAXS sample chamber at the P03/MiNaXS beamline of the PETRA III storage ring at DESY, Hamburg.*

Data treatment

The collected nWAXS data were further processed by the DPDAK software. The correction of SDD induced by the chamber thermal expansion was realized by calibrating Kapton tape reflex to 0.5 $Å^{-1}$. Figure 3.8 shows the 2D nWAXS data and the corresponding cake example. Cake cuts of the 2D nWAXS data for pseudo-XRD were done with the limits of χ = [0, 360°] and q = [0.6, 3.8] $Å^{-1}$. The cut results are plotted in a q versus intensity curve, namely pseudo-xrd cut. By analyzing the pseudo-XRD cut, the crystallinity, lattice distance, and crystal size can be obtained. The analyzed results

and discussions are depicted in Chapter 6.

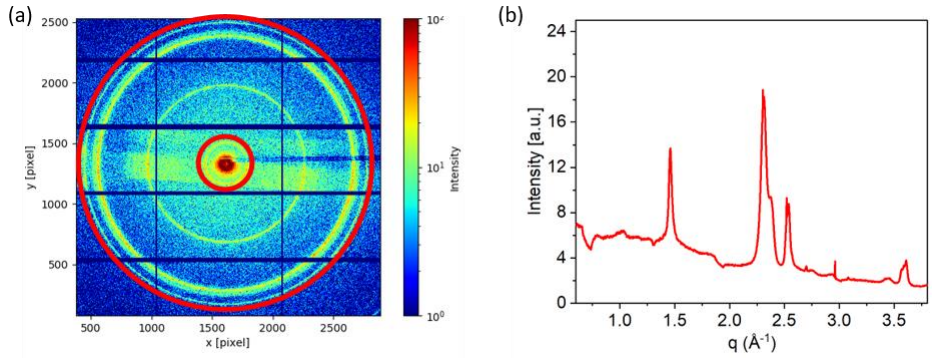

Figure 3.8. *Examples of cake cuts in nWAXS data analysis. (a) Exampled 2D nWAXS image, with the red area represent cake cut area. (b) Pseudo-XRD profile obtained from the cake cut of (a). Copyright 2025 by the authors. Advanced Science published by Wiley-VCH GmbH.*

3.2 Thermal properties characterization

3.2.1 Differential scanning calorimetry

Differential scanning calorimetry (DSC) is a method which simultaneously detects the heat flow rate of a sample and an inert reference. With the difference of two collected data, the information about phase transition can be gathered. The first order phase transition includes endothermic and exothermic behavior, and a peak should appear in DSC curve. During endothermic transition, the heat flows into the sample, resulting to an up facing peak; while the exothermic transition reversed this process and causing a down facing peak. The second order phase transition can not result in a peak but in a step. For the polymer samples, the first order transition (melting and crystallization), and second order transition (glass transition) are determined with DSC measurement.

Glass transition

If a polymer in its molten state is cooled it will at some point reach its glass transition temperature (T_g). Across this temperature the polymer chain mobility will be changed so that the polymer will change from elastic to brittle. It is important to note that the transition does not occur suddenly at one unique temperature but rather over a range of temperatures. The temperature in the middle of the inclined region is taken as T_g.

Crystallization

Crystallization is an exothermic process, and the polymer is releasing heat when undergoing crystallization. The crystallization temperature (T_c) is normally higher than T_g so that the polymer chain can have enough energy to form ordered arrangements.

Melting

Melting is an endothermic process, and the polymer is absorbing heat when undergoing melting. When reaching the melting temperature (T_m), the crystalline region gets molten and the chains can move freely. The ordered arrangements are broken. Figure 3.9 shows the DSC signals of T_g, T_c, and T_m.

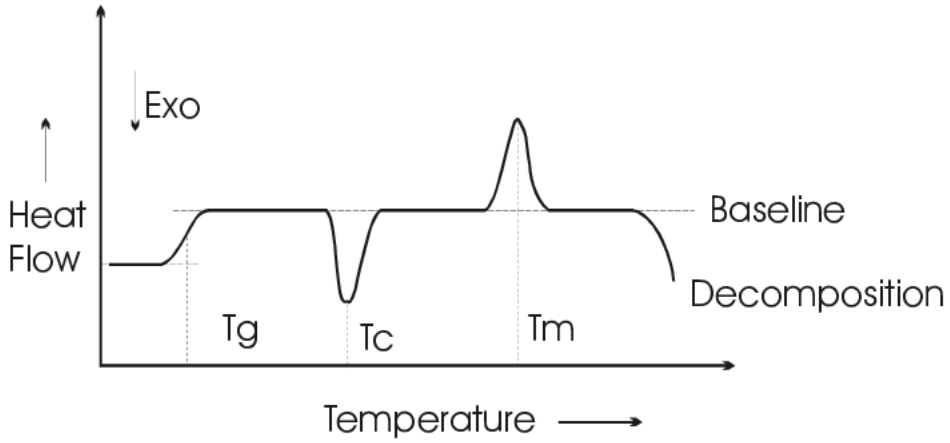

Figure 3.9. *Illustration of T_g, T_c, and T_m peaks in the DSC curve.*

Crystallinity

The crystallinity of polymers can be calculated by analyzing the endothermic melting process. The enthalpy of the melting process (ΔH_f) is used for the calculation:

$$\Delta H_f = \int_{T_i}^{T_f} C_p \, dT \tag{3.2}$$

where C_p is the heat capacity (constant pressure), T_i is the temperature of melting process begins and T_f is the temperature where the melting process is completed. With the assistance of equations 3.2 and 3.3, the enthalpy equation can be reformed to a more useful format (equation 3.4).

$$C_p = (\frac{dQ}{dT})_p \tag{3.3}$$

$$\Phi = \frac{dQ}{dT} = C_p \frac{dT}{dt} \tag{3.4}$$

where Q is the heat and Φ is the heat flux.

$$\Delta H_f = \frac{1}{hr} \int_{T_i}^{T_f} \Phi \, dT \tag{3.5}$$

where hr is the heating rate of DSC measurement. With this, the crystallinity can be obtained by the equation:

$$X_c = \frac{\Delta H_f}{\Delta H_f^0} \tag{3.6}$$

where ΔH_f is the enthalpy of the sample at the melting point and ΔH_f^0 is the enthalpy of the totally crystalline polymer measured at the equilibrium melting point.

In this thesis, the DSC measurement (Chapter 6) is done with a scan range of -80 to 100 °C and the heating rate of 10 °C min^{-1}. The sample is placed in a pan (sample holder) and inserted into the instrument for testing and data collection after sealing it and puncturing a hole for the gas to eject. The weight of sample normally should between 5 - 10 mg for better measurement. The output of a DSC test of a polymeric material typically presents a graph with temperature on the horizontal axis and heat flow on the vertical axis. The heat flow is normalized per unit weight of the sample.

3.2.2 Thermogravimetric analysis

Thermogravimetric analysis (TGA) is a technique in which the mass of the substance is monitored as a function of temperature as the sample is subjected to a controlled temperature program in a controlled atmosphere. With the TGA measurement, one can not only evaluate the thermal stability of materials, but also understand the physical and chemical phenomena, such as phase transition, thermal decomposition and oxidation/reduction [133-134].

The following features of the TGA curve can be identified:

i. A horizontal plateau, which is indicative of constant weight;
ii. A curved portion. The sloop of the curve is indicative of the rate of weight loss and will reach a maximum value.

iii. An inflection, which may indicate a formation of an intermediate compound.

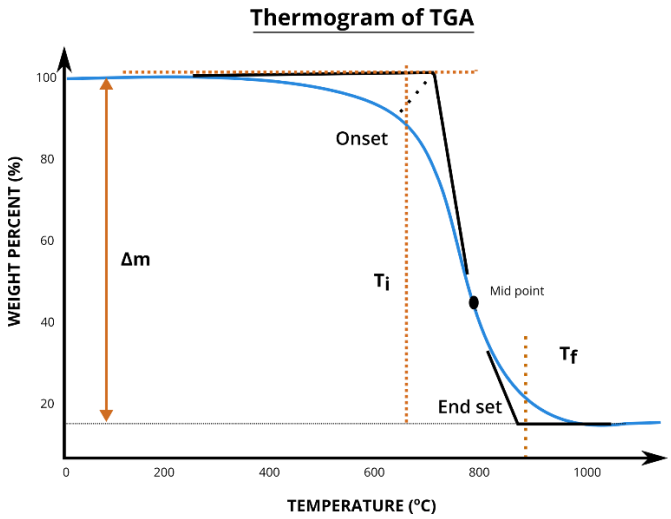

Figure 3.10. *Illustration of TGA curve.*

Figure 3.10 shows a typical TGA curve. In the TGA curve, mostly displays weight losses, which are typically caused by chemical reactions such as decomposition, combustion, and loss of water of crystallization, and physical reactions such as vaporization, sublimation and evaporation. Occasionally, a gain in weight is observed, which originats from the chemical reactions such as reactions with gas substance and the physical transitions such as absorption of gas substance. A generic thermogram normally have multiple sections [135]:

i. Below 150 °C: physisorbed water, low molecular weight volatile compounds, solvents, and trapped gases evolve;

ii. Between 150 °C to 250 °C: mass loss due to chemisorbed water and low molecular weight compounds like additives and volatile decomposition products;

iii. Above 250 °C: compounds begin to decompose between the onset and endset temperature. Multiple onset and endset temperatures are possible for multi-component systems and for reactions with intermediate steps.

iv. The remaining material above the endset temperature includes non-volatile inorganic ashes and metals.

In this thesis, the TGA measurement (Chapter 6) was conducted on the Mettler Toledo TGA/DSC 3 ± MS machine. The measurements were conducted from room temperature to 600 °C, with a ramp of 10 °C min^{-1} under Argon gas.

3.3 Spectroscopic characterization

3.3.1 Fourier-transform infrared spectroscopy

The infrared (IR) regions are lying between visible and microwave end region of the electromagnetic radiation spectrum. The mid-wavelength IR region ranges from 400 – 4000 cm^{-1}. It contains the most important group frequency region and fingerprint region and can be used as analytical tool that investigates the structural chemistry of the sample by irradiating with IR radiations. IR measures the amount of radiations absorbed by the molecule and their intensity. The absorption of the IR radiations causes various molecular motions in the molecule, including molecule vibration, molecule rotation, and electronic excitation, which create a net dipole moment. Therefore, a molecule is described as IR active should contains a net dipole moment, otherwise this molecule is IR inactive.

The atoms in polymers are covalently linked and these bonds are flexible, acting like elastic springs, resulting in different types of vibrations, and each molecule has unique vibration spectrum. For a molecule with n atoms, there will be (3n – 6) degrees of vibrational modes. There are two typical vibration modes: stretching and bending vibration. Figure 3.11 gives the major stretching and bending vibrational modes.

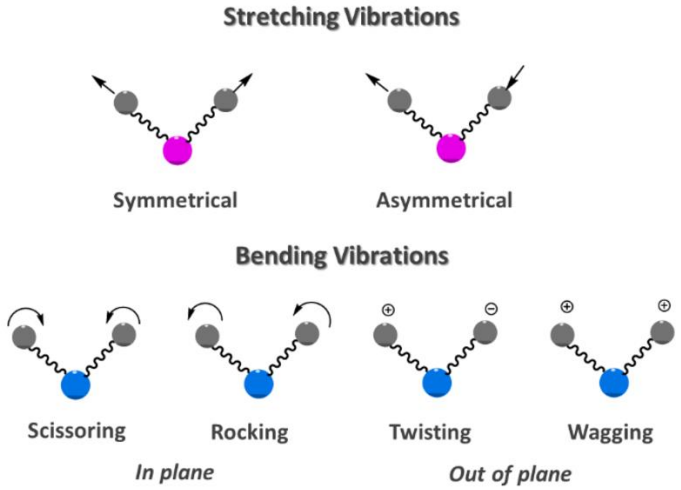

Figure 3.11. *Major stretching and bending vibrational modes [218]. Copyright 2021 by the authors. Licensee MDPI, Basel, Switzerland.*

Symmetric (ν_s) and asymmetric (ν_{as}) vibration are the typical starching vibration, and

these will arise when a molecule possesses a minimum of two equivalent bonds. In the symmetric stretching the dipole moment of participants will increase/decrease simultaneously; while, in the asymmetric stretching, the bond length changes on versus direction. The asymmetric stretching possesses higher energy than the symmetric stretching.

Bending vibration is a deformation vibration that the bond angle will change, and the bend length remains.

i. In plane bending vibration: in the in-plane bending mode, the bond moves in one dimension. Scissoring vibration (δ) involves two atoms, connected to the same center atom, moving further apart or closer together, thus altering the angle. In another in plane bending vibration, rocking vibration (ρ), the bond angle remains unchanged, because the moment of two atoms are moving in same direction.

ii. Out-of-plane bending vibration: in the in-plane bending mode, the bond moves in two dimensions. This vibration mode includes wagging (ω) and twisting (τ) vibration, and the bond angle will change. In wagging vibration, the adjacent atoms move toward a common side of the plane. While in twisting vibration, both the atoms go opposite to each other, orthogonal to the molecular plane.

In a dispersed IR spectroscopy experiment, each wavelength has to be detected individually, therefore, the experiment is a slow process and spectra is easily disturbed by stray light, as well as the poor accuracy and repeatability. This problem was solved with the advent of Fourier transform infrared spectroscopy (FTIR). As shown in Figure 3.12, the typical FTIR spectrometer consists of an IR light source, interferometer, sample compartment, detector, amplifier, and computer. The radiation is generated from IR light source, through the interferometer and strike on the sample. The signal is amplified and converted to a digital signal, and translated to its spectrum through the fast Fourier transform algorithm. The interferometer, which contains a beamsplitter, a fixed mirror and a movable mirror, is the core component of FTIR spectrometer. The single light beam is split into two light beams through the two mirrors, which travel at different path, and the difference is defined as optical path difference (OPD, δ). The interference appears from the two light beams, and it could be constructive ($\delta = n\lambda$) or destructive ($\delta = (n + 1/2)\lambda$), and will generate large intensity and small intensity, respectively. Therefore, as the position of moving mirror changes, the resultant beam intensity grows dimmer and brighter and passes through maximum and minimum. Therefore, the interferogram is plotted with the light intensity versus OPD.

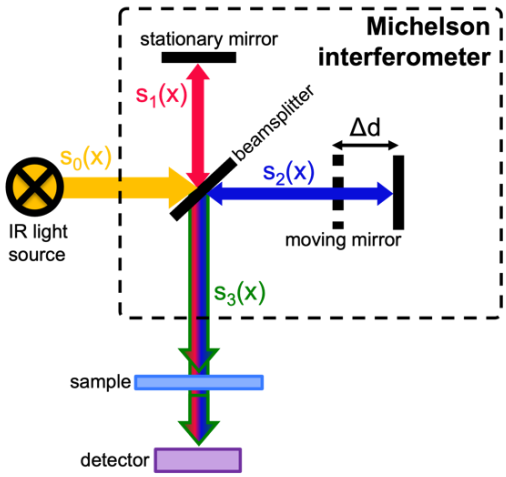

Figure 3.12. *Illustration of a typical FTIR spectrophotometer simplified configuration and working principle.*

Consequencely, the spectrum of the infrared beam that is measured by the detector can be obtained by Fourier transforming (FFT) an interferogram. Mathematically, this relationship is expressed as:

$$I(\Delta d) = \int_{-\infty}^{+\infty} I(\nu)\cos(2\pi\nu\Delta d)d\nu \tag{3.7}$$

where $I(\nu)$ is the intensity of the spectrum, Δd is the OPD.

By using Euler's formula:

$$cos\theta - isin\theta = e^{-i\theta} \tag{3.8}$$

the FFT equation can be expressed as:

$$I(\Delta d) = \int_{-\infty}^{+\infty} I(\nu)\exp(2\pi i\nu\Delta d)d\nu \tag{3.9}$$

During the FTIR measurement, the background spectrum is needed before the sample scan to eliminate characteristic bonds contributed from instrument and atmosphere. Consequently, the transmittance spectrum can be obtained:

$$\%T = \frac{I_{sample}(\nu)}{I_{bkg}(\nu)} \tag{3.10}$$

where %T is the transmittance, $I_{sample}(\nu)$ is intensity of the measured sample in the beam (single-beam spectrum), and $I_{bkg}(\nu)$ is intensity of the background spectrum. Meanwhile, the absorbance spectrum can be calculated from the equation:

$$A(\lambda) = -log_{10}(\%T(\nu)) \tag{3.11}$$

here, $A(\lambda)$ is the absorbance.

In Chapter 6, FTIR measurement focus on both the transmittance and absorbance signal of composite electrolyte deposited on Si wafer substrate. The FTIR measurements was conducted using an Equinox 55 spectrometer, from Brucker, USA. The frequency is adjusted from 4000 to 400 cm^{-1} with a resolution of 2 cm^{-1}. 256 times spectra were acquired for an acceptable signal–to–noise level. Peakfit software was used to fit the spectra with Gaussian functions.

3.4 Electrochemical characterization

The performance of a battery is decided by the actual cell potential, the current delivering capacity and specific energy. The practical cell potential is much less than the theoretical cell potentials due to various overpotentials at anode and cathode plus the electrolyte resistance. The current produced by the battery depends on the electrochemical properties of the electrodes materials plus electrochemical battery reaction. In Section 3.4, various electrochemical characterizations are explained from the evaluation of batteries performance.

3.4.1 Potentiostatic electrochemical impendence spectroscopy

Impedance spectroscopy evaluates the electrochemical behavior of materials and their interface with electrodes by observing their response to an electrical stimulus. Their response depends on a number of fundamental processes. In the case of an electrode-electrolyte system, these include the transport of electrons through the electrodes and cables, the transport of ions in the electrolyte and the exchange of electrons at the electrode-electrolyte interface with the cell materials or a reaction with the environment [135-136]. Besides the Ohmic resistance of the electrodes and the electrolyte and the reaction rate at the interface, which are dominating the current, grain boundaries and

point defects can also have an influence. Hence, we can obtain information about ionic and electrical conductivity (high frequency region), mobility of charges (high-middle frequency region), capacitance of interface (high-middle frequency region), and diffusion coefficients (low frequency region).

In this thesis, potentiostatic elecrtochemical impedance spectroscopy (PEIS) is used to determine the resistance of certain processes of an electrochemical cell. In a PEIS experiments, a small sinusoidal single frequency perturbation voltage is applied:

$$U(t) = U_0 sin(\omega t) \tag{3.12}$$

where U_0 is the amplitude of the signal and ω which equals to 2πf is the applied frequency. The amplitude is kept low to guarantee a linear response. This means the resulting response is an AC current with the same sinusoidal form and frequency but the curve may be shifted:

$$I(t) = I_0 sin(\omega t + \phi) \tag{3.13}$$

where I_0 is the dissimilar magnitude and ϕ is the phase shift dependent on the frequency $\omega = 2\pi f$. Using Fourier transformation simplifies the further treatment, so we use $U(\omega) = U_0\pi$ and $I(\omega) = I_0\pi\, exp(i\phi)$. Now the relations for capacitors and inductors which are $I(t) = C\frac{dU(t)}{dt}$ and $U(t) = L\frac{dI(t)}{dt}$ in real space, become:

$$I(\omega) = U(\omega) i C_\omega \tag{3.14}$$

and

$$I(\omega) = \frac{U(\omega)}{iL(\omega)} \tag{3.15}$$

They have a form similar to Ohm's law, if introduce the impedance function $Z(\omega)$ which is R for a resistor, $\frac{1}{iC\omega}$ for a capacitance and $iL\omega$ for an inductance. The value at a specific ω is referred to as impedance Z of the circuit. For the impedance of a circuit with multiple elements, the same rules apply as with multiple resistors. As Z is a complex quantity, it can be written as:

$$Z = Re(Z) + jIm(Z) = |Z|(\cos\phi + jsin\phi) \tag{3.16}$$

with

$$|Z| = \sqrt{Re(Z)^2 + Im(Z)^2} \tag{3.17}$$

and

$$\phi = \arctan(\frac{Im(Z)}{Re(Z)}) \tag{3.18}$$

PEIS measures the amplitude $|Z|$ and the phase shift θ for varying frequencies. A common way to visualize the obtained data is to plot $-Im(Z(\omega))$ versus $Re(Z(\omega))$, known as a Nyquist plot.

In order to analyze a Nyquist plot, an equivalent circuit consisting of resistors, capacitors, inductors and distributed impedance elements is needed which can then fit the PEIS data. The simple RC circuits and the corresponding Nyquist plots can be found in Figure 3.13. The simple resistor (Figure 3.13a) in a Nyquist plot is a point where the resistance value can be read directly. For a serial arrangement of a resistor and a capacitor as displayed in Figure 3.13b left, the impedance can be written as:

$$Z = \mathrm{R} - \frac{i}{\omega C} \tag{3.19}$$

Then the real part of impedance is constant, independent of the frequency, while the imaginary part depends on the frequency. For very small frequencies, the imaginary part is very large, and this value decreases inversely with frequency. For frequency approaches to infinity, the imaginary part of impedance closes to zero and the impedance value at this very high frequency equals to resistance. Thus, the Nyquist plot for this arrangement appears as a vertical straight line, starting from a lower frequency value at the upper part downwards when the frequency increases, as shown in Figure 3.13b right. The intersection of this line with horizontal axis (the real value of impedance) corresponds to the resistance.

For a parallel arrangement of resistor R and capacitance C, as appearing in Figure 3.13c left, the real and imaginary parts of the impedance are given by

$$Z' = \frac{\mathrm{R}}{1 + (\omega RC)^2} \tag{3.20}$$

and

$$Z'' = R\frac{\mathrm{R}}{1 + (\omega RC)^2} \tag{3.21}$$

and the corresponding Nyquist plot appears as an arc, seen Figure 3.13c right. The intersection of this arc with the vertical axis at a low frequency (right arc) corresponds to the resistance. From the intersection point at the low frequency region and the

position of the arc peak, the resistance and the capacitance of the system can be determined.

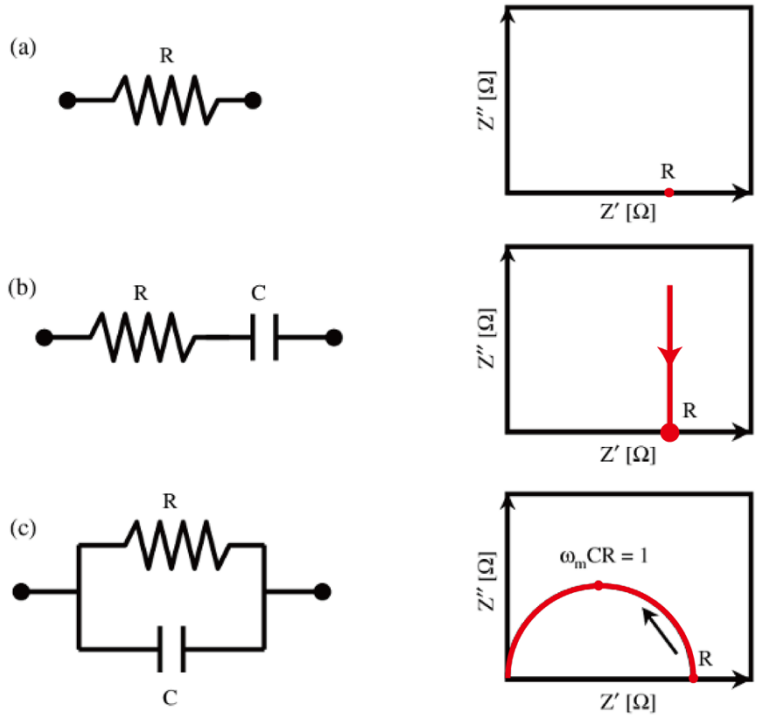

Figure 3.13. *Examples of simple RC circuits and the corresponding impedance (Nyquist) plots: (a) resistor, (b) serial arrangement of a resistor and a capacitor, and (c) parallel arrangement of resistor and a capacitor. Information is required from [137]. Copyright 2004 American Scientific Publishers.*

Figure 3.14 shows a Nyquist plot and its equivalent circuit model in the sandwiched battery framework. The initial point at high frequency represent the resistance of electrolyte. With decreasing frequency, the charge transfer happens and induction interface forms, act as the double-layer capacitance and charge transfer resistance in the equivalent circuit. Continuously the frequency decreasing, diffusion becomes domain process in the battery rather than the charge transfer, thereafter the diffusion resistance appears, namely Warburg resistance.

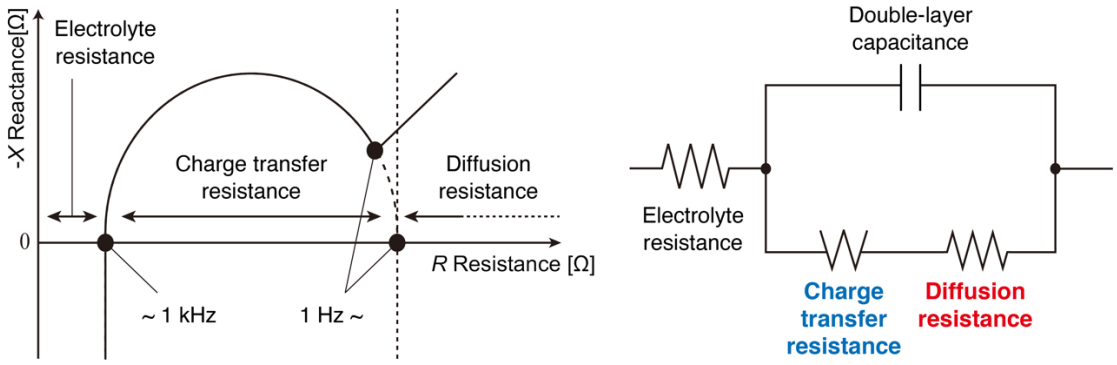

Figure 3.14. *Illustration of a typical battery Nyquist plot and its equivalent circuit when sweep from high frequency to low frequency.*

In this thesis, the EIS measurements were carried out on a VMP300 Biologic electrochemical workstation (Biologic, America). For ionic conductivity, the frequency range was from 1 MHz to 1 Hz with an AC voltage amplitude of 10 mV and was applied to a symmetric cell with two stainless steel electrodes. The ionic conductivity σ was calculated following a previously reported approach, according to the following equation:

$$\sigma = \frac{l}{RS} \tag{3.22}$$

, where l refers to the thickness of electrolyte, R refers to the resistance, and S refers to the electrode area.

3.4.2 Cyclic voltammetry

Cyclic voltammetry (CV) is to qualitatively analysis the electrochemical reactions by measuring the current flow between electrodes. In CV test, the potential is scanned and the tests are presented as current-voltage curves, and also called voltammograms [138]. In the voltammogram, the x-axis represents the parameter that imposed on the system, here the applied potential (E); while the y-axis is the response, here the resulting current (I) [135]. Figure 3.15 gives the example of a ferrocenium (Fc^+) to ferrocene (Fc) voltammetry curve. Two peaks can be observed: a catholic reduction and an anodic oxidation of the ions. The point A, D, G and arrow show the initial potential, switching potential, end potential, and the scan direction, respectively. The two peaks in the CV curve can be explained with the Nernst equation, which relates the potential of electrochemical cell (E) to the standard potential (E_0) and the relative activities of the oxidized (Ox) and reduced (Re) analyte in the system:

$$E = E^0 + \frac{RT}{nF}\ln\frac{(Ox)}{(Re)} = E^0 + 3.3026\frac{RT}{nF}log_{10}\frac{[F_c^+]}{[F_c]} \quad (3.23)$$

here, F is Faraday's constant, R is the universal gas constant, n is the number of electrons, and T is the temperature.

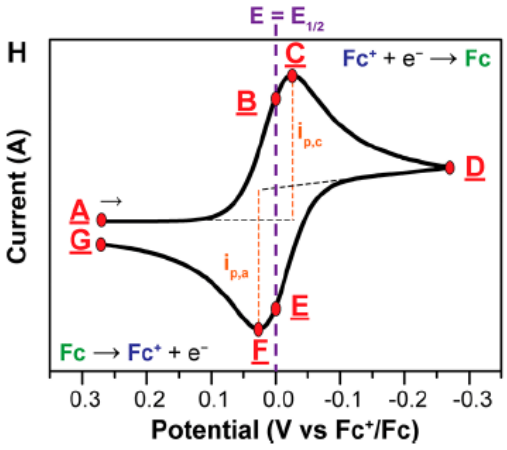

Figure 3.15. *Illustration of a typical voltammogram of the reversible reduction of a 1mM Fc^+ solution to Fc, at a scan rate of 100 mV s^{-1} [139]. Copyright 2018 American Chemical Society.*

The Nernst equation provides a powerful way to predict how a system will respond to a change of concentration of species in solution or a change in the electrode potential. In the example, when the potential is scanned during the CV experiment, the concentration of the [Fc^+] and [Fc] in solution near the electrode changes over time in accordance with the Nernst equation. More importantly, the concentrations of [Fc^+] vs [Fc] relative to the distance from the surface of the electrode are dependent on the potential applied and how species move between the surface of the electrode and the bulk solution. Therefore, the peaks in CV curve exist. In the example curve, from point A to C, Fc^+ is reduced to Fc in the surface with an increased fast diffusion of Fc to the electrode. The higher the oxidation potential applied to the electrode, the higher the current and higher ratio of [Fc^+]/[Fc] till the electrode potential reaches point B, whose potential is $E_{1/2}$, where [Fc] = [Fc^+]. The diffusion rate continues growing until point C (E_p), where the peak cathodic current ($I_{p,c}$) is observed. With more Fc^+ is reduced to Fc in the surface, the diffusion layer expands and slows down the transport of Fc^+ to the electrode, resulting in a decreased current as the scan continue (point C to D). The current decreases, as the electrooxidation becomes diffusion controlled. At point D, the

current converges to the value of "diffusion-limited current". The same process occurs when scanning Fc in a negative direction, resulting in a reduction peak.

One can easily distinguished that the peaks are not in reflection but separated, peak-to-peak separation (ΔE_p), which can be attributed to the diffusion of the analyte to and from the electrode. The separation degree is a parameter to evaluate the electrochemcial reversibility of the process, which is related to the electron transfer kinetics between the electrode and the analyte [140]. When there is a low barrier of electron transfer (electrochemical reversibility), the Nernstian equilibrium is established immediately upon any change in applied potential. By contrast, when there is a high barrier of electron transfer (electrochemical irreversibility), electron transfer reactions are sluggish and more negative (positive) potentials are required to observe reduction (oxidation) reactions, giving rise to larger ΔE_p.

The scan rate of CV measurements also controls the voltammeogram. Faster scan rate leads to a decreased in the size of the diffusion layer; as a consequence, higher currents are observed [139]. For the electrochemical reversible electron transfer process, the relationship can be described by the Randles-Sevcik equation:

$$i_p = 0.4463\, nFAC\left(\frac{nFvD}{RT}\right)^{1/2} \tag{3.24}$$

where i_p is the current maximum in amp, n is the number of electrons transferred in the redox event, F is the Faraday constant in C mol^{-1}, A is the electrode area in cm^2, C is the concentration in mol cm^{-3}, D is the diffusion coefficient in $cm^2\ s^{-1}$, v is the scan rate in V s^{-1}, R is the gas constant in J K^{-1} mol^{-1}, T is the temperature in K.

In Chapter 5, CV measurement is applied on the Li||Cu cells with the PEO composite materials as electrolyte. The CV measurements was conducted using a VMP300 Biologic electrochemical workstation (Biologic, USA). The sweep sequence is from 2.5 V to 0 V for reduction process, and 0V to 2.5 V for oxidation process. The scan rate is 5 mV s^{-1}.

3.4.3 Liner sweep voltammetry

Liner sweep voltammetry (LSV) is similar as CV but differs in that it uses one direction single sweep from initial potential to end potential. In LSV measurement, the ion-blocking electrode is used to surpass the migration of charge reactants and products so that any transfer of electroactive species to and from electrodes surface can only realize

by diffusion. As shown in Figure 3.16a, the working electrode potential is linear changed with time, starting from the potential site where no reactions occur on electrodes, and sweeping to the potential site where the oxidation (more positive value) takes places. Then the current-potential curve was plotted, seen Figure 3.16b, where i_p and E_p represent the peak current and peak potential, respectively, and $E_{p/2}$ is the half-peak potential, corresponding to the potential at $i = i_p/2$.

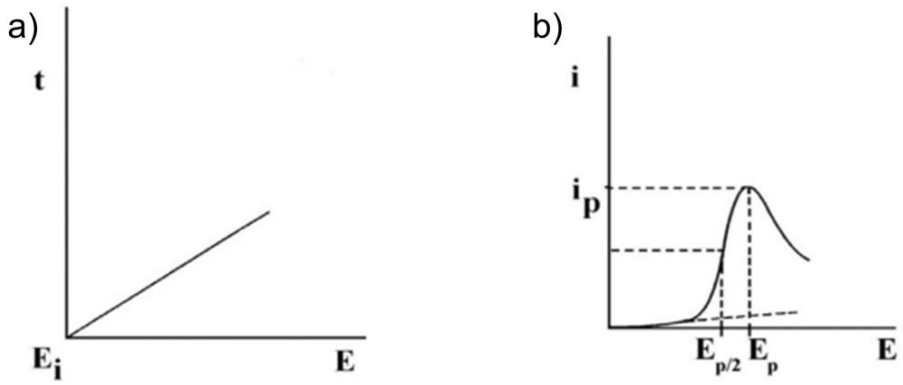

Figure 3.16. *Illustration of a typical LSV voltammogram of in (a) potential-time curve and (b) potential-current curve [141]. Copyright 2016 Elsevier*

The peak potential (E_p) position determined the formal potential of redox process, while the peak current (i_p) provides information on the analyte concentration, number of electrons involved in the electrochemical process and possible presence of coupled chemical reactions. When sweeping in the region where no charge transfer occurs (from initial potential site to before the rising part), only a little capacitive current can be recorded, and the electrode-electrolyte interphase behaves like capacitor. When sweeping to the region where the electrochemical reaction occurs, a faradic current is recorded which increased sharply until maximum is reached; thereafter the current decreases steadily enough. The electron transfer process remaining in the rising portion of the peak, as the potential becomes more suitable for it occurrence; with the increasing thickness of the diffusion layer caused by the progressive depletion of the depolarizer at an ever-increasing distance from the electrode surface (prevailing in the descending branch).

In Chapter 5 and Chapter 6, LSV measurement was applied on the Li||SS cells with various types of PEO composite materials as electrolyte. The LSV measurements was conducted using a VMP300 Biologic electrochemical workstation (Biologic, USA). The sweep sequence is from 2 V to 7 V with the scan rate of 1 mV s^{-1}.

3.4.4 Chronoamperometry

Chronoamperometry (CA) is an amperometry technique where a constant potential is applied and the resulting current is recorded over time. A single potential step is used: from a potential where no redox reactions are occurring to a high positive potential to drive the turnover of the target species, and this potential normally smaller than 0.5 V. A spike current is observed in the very initial time (~ 10 ms) and followed by a decay in current to a constant value, as shown in Figure 3.17. This behavior can be described by the Cottrell equation:

$$i = \frac{nAFD^{1/2}C}{(\pi t)^{1/2}} \tag{3.25}$$

where i is the current, n is the number of electrons, F is the Faraday constant, A is the area of the electrode, C is the initial concentration of the reducible analyte, D is the diffusion coefficient for species, and t is the time.

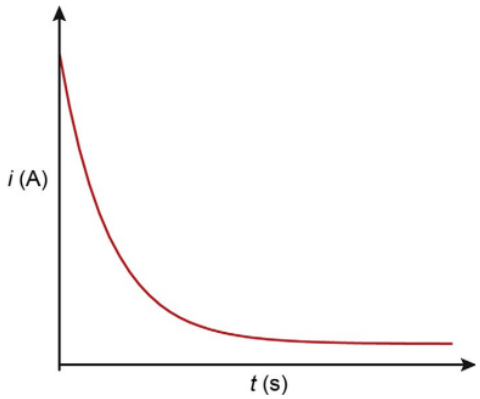

Figure 3.17. *Typical current-time curve from chronoamperometry experiment [142]. Copyright 2020 Elsevier.*

In Chapter 5 and Chapter 6, The Li^+ transfer number was calculated by the potentiostatic polarization method with 10 mV constant voltage on a Li||Li symmetric cell with various PEO composite materials as electrolyte. The electrochemical impedance spectroscopy (EIS) measurement was performed on the cell before and after polarization, and polarization process was realized by CA measurement. The measurements is conducted using a VMP300 Biologic electrochemical workstation, from Biologic, USA. The Li^+ migration number t_{Li+} is then calculated using the following equation:

$$t_{Li^+} = \frac{I_s(\Delta V - I_0 R_0)}{I_0(\Delta V - I_s R_s)} \tag{3.26}$$

where I_0 and I_s represent the initial and steady state current after polarization, which can be obtained from CA measurement. R_0 and R_s represent the interfacial resistance before and after polarization, which can be obtained from EIS measurement, and ΔV is the polarization voltage, which in this thesis is 10 mV.

3.4.5 Galvanostaic charge-discharge cycling

Galvanostaic charge-discharge (GCD) cycling is the most practical way to assess capacity, reversibility, stability and rate capacity of electrode materials. Different from voltammetry measurement, which observes the current changes, GCD cycling using current as parameter and the voltage and capacity as response. In addition, the initial and terminal voltage have to be determined [143]. In a typical single charge-discharge cycle, constant current is applied, and the oblique line with a roughly recognizable plateau is obtained as voltage-capacity profile, as shown in Figure 3.18a and b. The starting potential and terminal potential are recognized as E_1 and E_2, and the charge/discharge plateau corresponds to the potential E_C and E_D, respectively. To better illustrate the plateau, differential capacitive curve (dQ/dV versus V profile) is plotted, seen Figure 3.18c. The charge/discharge plateau is converted to the cathodic/anodic peaks, and both of them are correlated with the thermodynamics of the electrode reactions. When there are several sequential process in the overall electrode reactions and can be captured by the reaction voltage, there will be the same number of plateaus (voltage profile) and peaks (differential capacitive curve). Consequencely, the coulombic efficiency (CE) can be determined by the GDC cycle. CE is the ratio of the total charge extracted from the battery to the total charge put into the battery over a fill cycle. For cathode materials which act as charge carries donors, CE is the ratio of discharge to charge capacity. In an example towards anode materials, CE described the percentage up to which charge carriers can be extracted after they are inserted and corresponded to the ratio of the charge to discharge capacity. The total amount of charge carriers available in a battery is limited and unrecoverable, therefore, CE is an important factor to assess the lifespan of batteries in respect to the charge sustainability.

In GCD cycling, the constant current is normalized to be specific current (in the unit of A g^{-1}) or C-rate current, where 1C is defined as the necessary current to reach full capacity in one hour. Apart from the C-rate current, current density (in the unit of mg

cm^{-2}) which defined as the amount of charge per unit time that flows through a unit area of a chosen cross section is widely used when running the Li symmetric cell cycling. By repeatedly charging/discharging batteries, one can easily evaluate the cycle life, which is often referred to the cycle number when the reversible capacity fades to 80% of its initial value. By altering the C-rate current range, the rate capability can be assessed. As current rate is rising, the capacity decreases due to aggravated polarization, see Figure 3.18d. It should be emphasized that rate performance tests are only meaningful when charge/discharge profiles at any given rate significantly overlap. If the capacity decreases rapidly at some rate, then there is no need to perform cycling at higher rates.

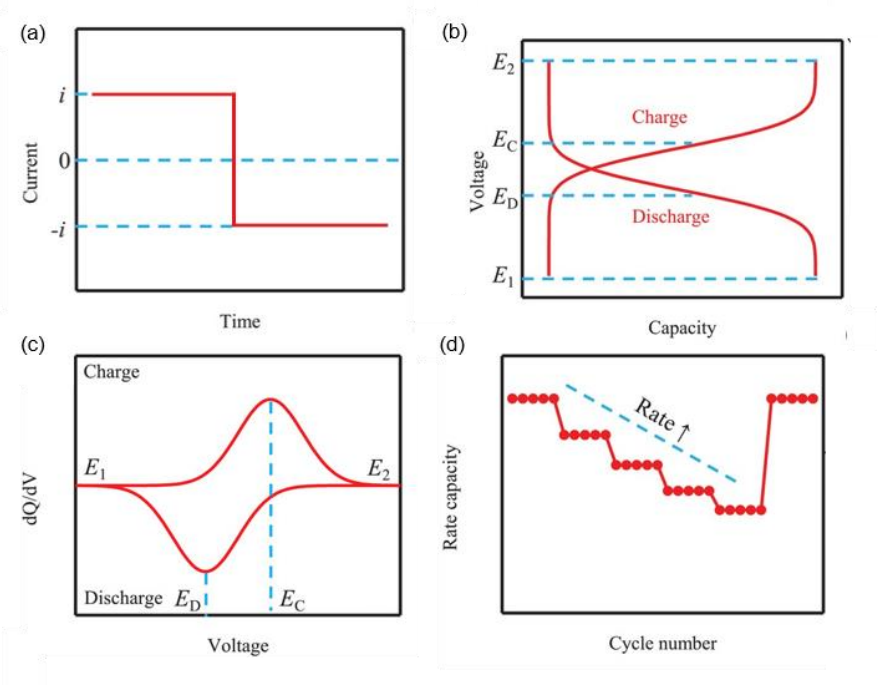

Figure 3.18. *GCD cycling: (a) applied current profile, (b) typical voltage response versus capacity profile, (c) differential capacity curve for charge and discharge cycle in GCD measurement, and (d) rate capability performance. Information taken from [143]. Copyright 2019 John Wiley & Sons.*

The GCD cycling in this thesis is using the Neware battery testing system (Neware, China). In Chapter 5, the GCD cycling is applied on Li||Li symmetric cells with PEO composite materials as electrolyte, at a current density of 0.1 mA cm^{-2} for 1 h per cycle, and the working temperature is 55 ºC. In Chapter 6, the GCD cycling is applied on Li||Li symmetric cells with modified PEO composite materials as electrolyte, at a current density of 0.1 – 0.7 mA cm^{-2} for 1 h per cycle. Furthermore, the GCD cycling

on Li||$LiFePO_4$ cells with modified PEO composite materials as electrolyte also performed at the 0.05 C for activation and 0.1 C for long time cycling. The working temperature for all the GCD cycling is 55 ºC.

4 Sample preparation

This chapter introduces the sample preparation conducted before all experiments described in this thesis. Accordingly, Section 4.1 lists the materials. Section 4.2 give the preparation of PEO based composite electrolyte, including the PEO-Al_2O_3 electrolyte fabrication and PEO-Al_2O_3-SN electrolyte fabrication. An explanation of $LiFePO_4$ electrode fabrication is presented in Section 4.3. Section 4.4 explains the assembly of coin cells. The standard Si wafer cleaning process for the FTIR measurement is given in Section 4.5.

4.1 Materials

Poly(ethylene oxide) (PEO)

Poly(ethylene oxide) (PEO, average M_w = 600,000 g/mol) was obtained from Sigma-Aldrich (Germany) and used as the polymer matrix for the synthesis of PEO based composite electrolyte. Initially, the obtained PEO powder was dried in the vacuum oven at 60 °C to remove the absorbed moisture, and then sealed in the Argon-filled glovebox for further use.

Aluminum oxide (Al_2O_3)

Aluminum oxide (Al_2O_3, < 50 nm nanopowder) was obtained from Sigma-Aldrich (Germany) and used as an inorganic filler for the synthesis of PEO based composite electrolyte. The obtained powder was dried in the vacuum oven at 60 °C to remove the absorbed moisture, and then sealed in the Argon-filled glovebox for further use.

Lithium bistrifluoromethanesulfonimidate (LiTFSI)

Lithium bistrifluoromethanesulfonimidate (LiTFSI, 99.95 % trace metals basis),

procured from Sigma-Aldrich (Germany), functioned as the lithium salt in the synthesis of PEO based composite electrolyte.

Succinonitrile (SN)

Succinonitrile (SN, 99 %), sourced from Sigma-Aldrich (Germany), was used as the plasticizer in the PEO based composite electrolyte, which can reduce the crystallinity of PEO.

Acetonitrile (ACN)

Acetonitrile (ACN, battery grade, 99.999 % trace metals basis) was bought from Sigma-Aldrich (Germany) and utilized as the solvent for the synthesis of PEO based composite electrolyte.

Polyvinylidene difluoride (PvDF)

Polyvinylidene difluoride (PvDF, average M_w = 534,000 g/mol), acquired from Sigma-Aldrich (Germany), was used as binder for the synthesis of $LiFePO_4$ cathode. The obtained powder was dried in the vacuum oven at 60 °C to remove the absorbed moisture, and then sealed in the Argon-filled glovebox for further use.

Carbon black (Super P)

Carbon black (Super P, 99 %), sourced from Shenzhen Kejing Star Technology Company (China), was used as the conductive agent in the synthesis of $LiFePO_4$ cathode.

Lithum ferro-phosphate ($LiFePO_4$)

Lithum ferro-phosphate ($LiFePO_4$), sourced from Shenzhen Kejing Star Technology Company (China), was used as the main active material in the synthesis of $LiFePO_4$ cathode.

N-methyl-2-pyrrolidone (NMP)

N-methyl-2-pyrrolidone (NMP, anhydrous, 99.5 %) acquired from Sigma-Aldrich (Germany) was utilized as solvent for $LiFePO_4$ cathode.

Lithium (Li)

Lithium (Li, 99.9 %) with 15.6 mm diameter and 0.25 mm thick was purchased from MSE Supplied LLC (America). The chips are sealed in the can in the Argon-filled glovebox. The Li chips was used as electrode in the coin cells.

Aluminum (Al) foil

Aluminum (Al, 99.9 %, foil) with 200 mm width and 9 µm thick was obtained from Shenzhen Kejing Star Technology Company (China). The Al foil was cut into a round shape with a diameter of 14 mm and employed as both electrode and current collector in the coin cells.

Stainless steel (SS)

Stainless steel (SS, Grade 304), procured from Shenzhen Kejing Star Technology Company (China), served as both electrode and current collector in the coin cells.

Copper (Cu) foil

Copper (Cu, 99.9 %, foil) with 180 mm width and 9 µm thick was obtained from Shenzhen Kejing Star Technology Company (China). The Cu foil was cut into a round shape with a diameter of 14 mm and employed as electrode in the coin cells.

Isopropanol (IPA)

Isopropanol (99.9 %), sourced from Carl Roth (Germany), was employed in the ultrasonic cleansing of Si substrates.

Deionized water (DI water)

Deionized water (99.9 %), sourced from Carl Roth (Germany), was employed in the ultrasonic cleansing of Si substrates

Hydrogen Peroxide (H_2O_2)

Hydrogen peroxide (H_2O_2, 30 %), procured from Carl Roth (Germany), was utilized as an oxidizing agent for the acid cleaning of Si substrates.

Sulfuric Acid (H_2SO_4)

Sulfuric acid (H_2SO_4, 96 %), obtained from Carl Roth (Germany), was employed for the acid cleaning of Si substrates.

Silicon wafers

Silicon wafers (Si 100, p-type) were acquired from Silchem Handels GmbH (Freiberg, Germany). These wafers were cut into segments measuring 2 cm × 2 cm and subjected to acid cleaning prior to their use as substrates for the FTIR measurement.

4.2 Preparation of PEO-based electrolyte

4.2.1 Synthesis of PEO-Al_2O_3 composite electrolyte

The PEO composite electrolyte is fabricated by the solution casting method. The weight amount of PEO and LiTFSI are determined based on the EO: Li molar ratio. The optimum molar ratio of EO:Li (R) is somewhere between 10 and 16. In this thesis, we use the optimized R value of 14. The weight amount of PEO and LiTFSI is calculated by the following equations:

$$R = \frac{n(Li^+)}{n(EO)} = \frac{n(LiTFSI)}{\chi \cdot n(PEO)} = \frac{n(LiTFSI)}{\frac{M(PEO)}{M(EO)} n(PEO)} = \frac{1}{14}, \tag{4.1}$$

where $\chi = \frac{M(PEO)}{M(EO)}$ is the number of EO segment per PEO molecule.

$$\frac{m(LiTFSI)}{m(PEO)} = 0.0714 \frac{M(LiTFSI)}{M(EO)} \tag{4.2}$$

Using the molarity formula, with the molar mass of LiTFSI being 287.08 g/mol and the molar mass of EO (monomer of PEO) being 44.05 g/mol, 1 g of PEO is used. The concentration of PEO in ACN is 60 mg/ml.

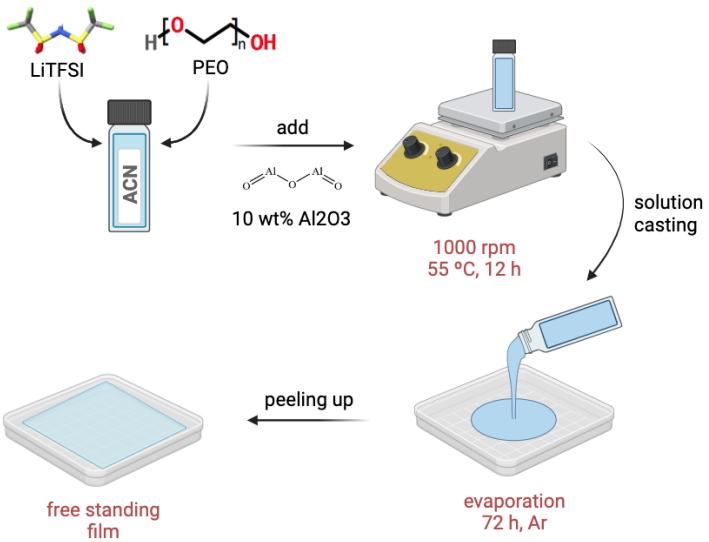

Figure 4.1. *Schematic illustration of the experimental procedure of the PEO composite electrolyte fabrication. This figure is produced by biorender.com.*

The preparation of PEO-Al_2O_3 composite electrolyte is shown in Figure 4.1. The PEO powder and LiTFSI powder are mixed in the ACN with the above mentioned ratio. Afterward, 10 wt% of Al_2O_3 nanopowder is added, and the above mentioned solution is constantly stirred at 55 ºC for 12 h to obtain a homogenous solution. Then the solution is poured on a Teflon plate by the solution casting method, followed with the evaporation at the Argon atmosphere for 72 h to obtain a homogeneous free-standing electrolyte.

4.2.2 Synthesis of PEO-Al_2O_3-SN composite electrolyte

The synthesis process of the PEO-Al_2O_3-SN composite electrolyte is similar with the PEO-Al_2O_3 composite electrolyte. PEO and LiTFSI are dissolved in the ACN with a ratio of EO: Li = 14. Afterward, 10 wt% of Al_2O_3 and 10 wt% SN are added, and the solution is constantly stirred for 24 h. Then the solution is poured on a Teflon plate, followed by the solution evaporation at the Argon atmosphere for 72 h to obtain a homogeneous free-standing electrolyte.

4.3 Preparation of $LiFePO_4$ cathode

For the $LiFePO_4$ (LFP) cathode preparation, lithum ferro-phosphate ($LiFePO_4$) is used as the active materials, with conductive carbon black (Super P) used as conductive agent and polyvinylidene fluoride (PvDF) served as binder to connect the Super P and $LiFePO_4$. The weight ratio of active material, conductive agent and binder is 8:1:1. Initially the PvDF is dissoved in the N-methyl-2-pyrrolidone (NMP), and the weight ratio of PvDF and NMP is calculated by the equation:

$$\frac{m(PvDF)}{m(NMP)} = 3.5\ \% \tag{4.3}$$

The mixture is stirred at 600 rpm for 3 h to obtain a well-dissolved solution. Subsequently, the Super P is added in the solution and stirred at 600 rpm for 30 min, followed by the stirring at 1100 rpm for 3 h to obtain a homogenous suspension. Subsequently, 50% of $LiFePO_4$ powder is added to the suspension and stirred at 600 rpm for 10 min to fully disperse the active materials. Another 50% of $LiFePO_4$ powder is added and directly stirred at high speed of 1300 rpm for 5 h to obtain a dispersed suspension.

The product then stands for 30 min to eliminate bubbles. This suspension is then poured on the Al foil, a doctor blade is used to spread the slurry on the Al foil, adjusting the thickness of the blade to 200 μm. After spreading the solution, place the glass plate in an oven set to 60 ºC to facilitate drying. The synthesis diagram of $LiFePO_4$ cathode as illustrated in Figure 4.2.

After drying the $LiFePO_4$ cathode, the film undergo calendaring to further reduce the porosity and improve the tap density. The calendaring pressure is set to 1 ton and the film is feed through on both directions. The last step for making a cathode is to punch it out of the strip. To minimize the edge effects, the film is sandwiched between two weight papers. The basic requirement is that the diameter of working cathode is smaller than that of lithium chip, and both are smaller than the composite electrolyte. For the 2032 type coin cells, 15 mm punch for the cathode is used.

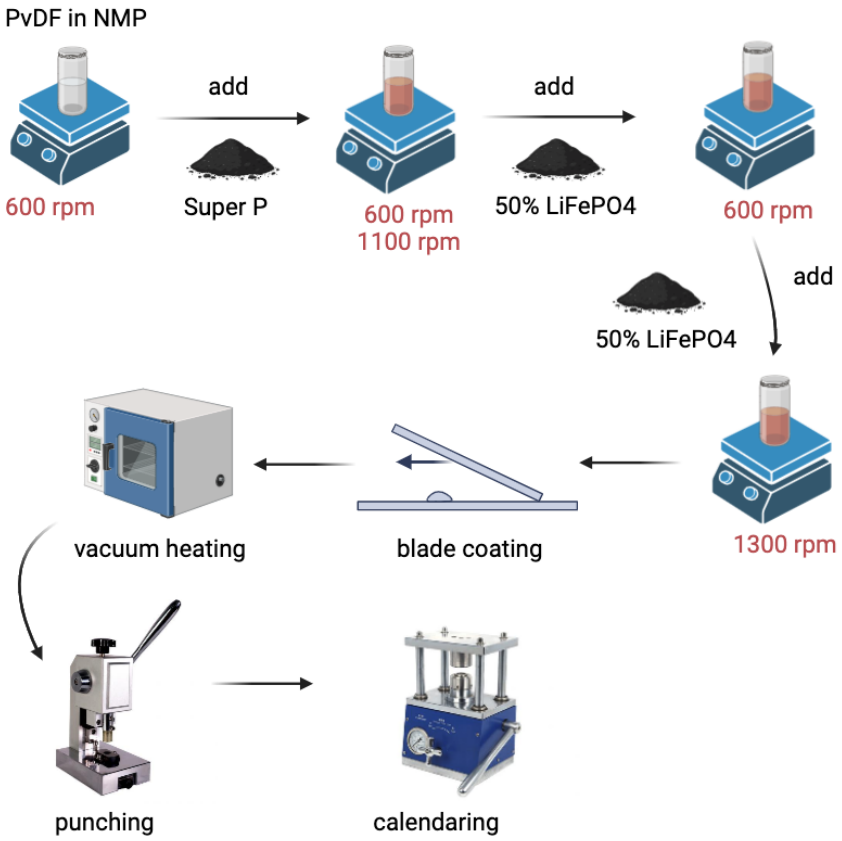

Figure 4.2. *Illustration of the process for preparing $LiFePO_4$ cathode. This figure is produced by biorender.com.*

4.4 Build lithium metal batteries

The batteries are using the CR2032 type coin cell with a diameter of 20 mm and a thickness of 3.2 mm. Due to the high reactivity of lithium metal, the coin cell assembly process is taken place within the Argon-filled glovebox where the H_2O and O_2 value is less than 0.1 ppm.

The coin cell cases are made of stainless steel to ensure optimal current record and to protect the internal components of the coin cell. An o-ring is placed on the top case to avoid any possible short circuit from the shell. Inside the coin cell case, there is a spring to apply uniformed pressure across various cell layers. This pressure is crucial for maintaining solid contact between the various components, ensuring efficient ionic and electronic conduction during the battery's operation. The spring's role is to keep the layers firmly in place, which helps to prevent shifts or gaps that could degrade the cell's performance over time. Next to the spring is the anode and its current collector. In the lithium metal batteries, the lithium metal chip is used as anode materials and the corresponding current collector is stainless steel. The lithium metal is soft and easy to shape, therefore a stiff stainless steel chip can maintain the lithium to avoid deformation when apply pressure.

At the heart of coin cells is the composite electrolyte which is made of PEO, LiTFSI, Al_2O_3 and additives, as explained in Section 4.2. The electrolyte is punched to the diameter of 19 mm to insulate the electrode and transport lithium ions when cycling. Following are the cathode and its current collector. In different types of coin cells, the cathode and current collector will be different. The cathode material is usually made from lithium iron phosphate (LFP) coated on an Al foil (current collector), lithium metal (stainless steel as current collector), or stainless steel (SS). In the coin cells, we use the configuration of "anode||cathode cells" to distinguish the component in the batteries. Accordingly, in this thesis, the following coin cells configurations are used: Li||Li cells, Li||SS cell, and Li||LFP cells. These electrodes are essential for the battery's energy storage capabilities, dictating its capacity, voltage, and overall performance. Figure 4.3 illustrates the coin cells components with the example of Li||LFP coin cell.

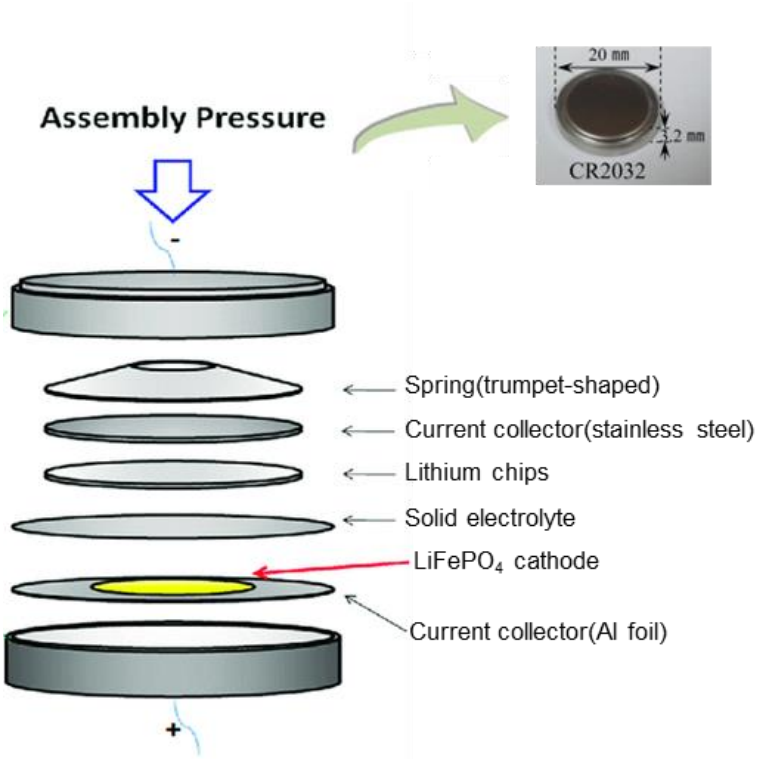

Figure 4.3. *Illustration of the coin cell component.*

To assemble coin cells, all the parts are aligned on top of a non-conductive surface (to avoid accidental shorting of the cell) in the argon-filled glovebox. The large cap is placed on the bottom and the put the cathode in. The composite electrolyte is placed on top of the cathode part, followed by the lithium disk and stainless steel current collector. Try to center the lithium disk as much as possible to avoid uneven current densities. Place the spring on top of stainless steel, then carefully put the small cap (with o-ring on) on top. For the crimper, the large cap will go on the bottom, and center it in the crevice. With a force of 100N, the coin cell was properly sealed with a press. The edge of sealed coin cell should be curved otherwise there will be leakage risk.

4.5 Si wafer cleaning protocol

Si is served as substrate for the FTIR measurements and underwent a standard cleaning procedure. To remove contaminants or organic residues from the surface of the Si substrate utilized in this thesis, the Si substrates are subjected to cleaning via a hot acid bath. Consequently, a solution comprising 50 mL of deionized water, 180 mL of H_2SO_4, and 80 mL of H_2O_2 is prepared in a beaker, which is then placed in a water bath to gently

heat the acidic mixture to a temperature of 80 °C.

To prevent evaporation, the beaker containing the acid solution is covered with a watch glass. Si substrates within a sample holder, are immersed in the acid bath. Following a 15 min treatment, the substrates are extracted from the acid solution and rinsed sequentially in DI water. Each substrate is then thoroughly rinsed with deionized water and dried under a steady stream of N_2. For extended storage, all substrates are kept in a sealed sample box for future use. In case the Si substrates that have been stored for a long period, it is necessary to re-clean the substrates. This involves securing them onto a holder and subjecting them to a cleansing process with isopropanol for 20 min in a water bath maintained at 30 °C. After this cleaning procedure, the substrates are dried with N_2 gas. Subsequently, oxygen plasma cleaning is performed using a NANO PLASMA CLEANER (Diener Electronic). The substrates are placed inside a vacuum chamber that is filled with oxygen, and plasma treatment is administered for 20 min at 0.45 mbar, 40 Hz, and 250 W. This oxygen plasma treatment increases the hydrophilicity of the surfaces. Afterwards, the electrolyte solution is diluted 20 times and spin coated with a ramp of 100 rpm on the cleaned Si wafer for FTIR measurement.

4.6 Sample preparation for X-ray scattering measurement

GISAXS/GIWAXS measurement

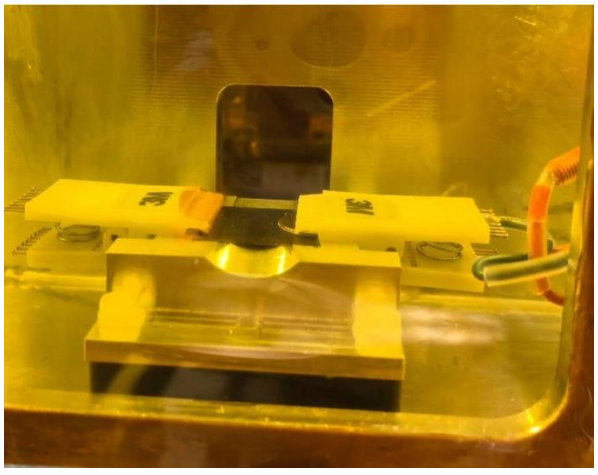

Figure 4.4. *Illustration of operando chamber of GISAXS/GIWAXS.*

The operando cell is shown in Figure 4.4. For GISAXS/GIWAXS measurements, the operando cell adopts a sandwich structure. A large aluminum stage stabilizes the entire

cell and also serves as the current collector. A 1 mm-thick copper foil is cut into a 2.5 cm × 2.5 cm square to construct the Li||Cu cell. The electrolyte, cut to the same shape, is then placed on top of the copper chip. To allow X-ray transmission, both the Li chip and the SS chip are cut into half-circle shapes and positioned accordingly on top of the electrolyte. After assembling all components, two clamps secure the sample to the stage. One of the clamps is connected to the cable of the VMP150 Biologic electrochemical workstation to apply a voltage sweep.

nWAXS measurement

The operando cell is shown in Figure 4.5. The sample is secured at the center of the Kapton window using long screws for measurement. The sample design resembles a coin cell, consisting of an Al current collector, Li metal, electrolyte, Li metal, and another Al current collector from top to bottom. To fit within the chamber, all components are cut to a size of 0.5 cm × 0.7 cm. Once assembled, four small screws are used to seal the cell, while the long screws allow for positional adjustments. The assembly of nWAXS cells is carried out inside an argon glovebox to prevent exposure to H_2O and O_2. The X-ray beam is focused on the Li/electrolyte interface and an area of 2 μm × 8 μm (width × length) is scanned in 4 ×16 steps to locally resolve structural changes. In combination with a counting time of 20 s. The cells are connected with potentiostat to realize charging/discharging cycling at the current density of 0.05 mA cm^{-2}. The X-ray beam transmitted through the Li/electrolyte interface and reached the detector.

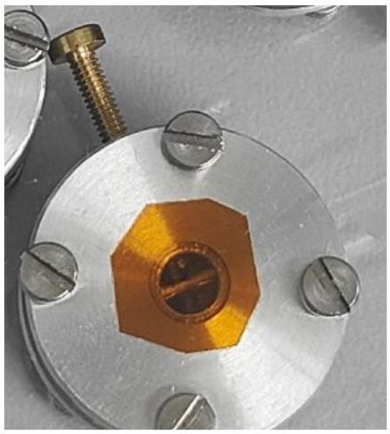

Figure 4.5. *Illustration of operando chamber of nWAXS.*

5 Lithiation/Delithiation Process Observation by GISAXS/GIWAXS

This chapter is based on the published article: Operando Study Insights into Lithiation/Delithiation Processes in a Poly(ethylene oxide) Electrolyte of All-Solid-State Lithium Batteries by Grazing-Incidence X-ray Scattering [19]. Reproduced with permission from (Y. Liang, T. Zheng, K. Sun, Z. Xu, T. Guan, F. A. C. Apfelbeck, P. Ding, I .D. Sharp, Y. Cheng, M. Schwartzkopf, S. V. Roth, and P. Müller-Buschbaum, ACS Applied Materials & Interfaces 2024, 16, 33307–33315, DOI: 10.1021/acsami.4c01661).

Polyethylene oxide (PEO)-based composite electrolytes (PCEs) are considered as the promising candidates for next generation lithium metal batteries due to its high safety, easy fabrication, and good electrochemical stability. Here, I utilize operando grazing-incidence small-angle and wide-angle X-ray scattering to probe the correlation of electrochemically-induced changes and the buried morphology and crystalline structure of the PCE. Results show that the two irreversible reactions, PEO-Li^+ reduction and $TFSI^-$ decomposition, cause changes in the crystalline structure, array orientation, and morphology of the PCE. In addition, the reversible Li plating/stripping process alters the inner morphology, especially the PEO-LiTFSI domain radius and distance between PEO-LiTFSI domains, rather than causing crystalline structure and orientation changes. This work provides a new path to monitor a working battery in real time and to detail understand the Li^+ diffusion mechanism, which is essential for developing interface stable lithium metal batteries.

5.1 Preface

Rechargeable lithium ion batteries (LIBs) are central to the revolution of energy storage technologies and have been successfully commercialized for a wide range of applications, from cell phones to electric vehicles (EVs) [22-144-145]. The low theoretical capacity of the dominant anode material, graphite (372 mAh g^{-1}), has spurred the development of lithium metal batteries (LMBs), in which the anode in replaced by metallic lithium, thereby yielding substantially increased theoretical capacity, reduced density, and low electrode potential [7-18-146-148]. While LMBs with liquid electrolyte have reached high conductivities and good interfacial performance characteristics, however, the combustible and toxic electrolyte still suffers from safety hazard and leakage issues [11-149]. Switching from the liquid electrolytes to solid-state electrolytes, such as polymers and ceramics, can not only solve these safety concerns, but also facilitates the commercialization of LMBs. In particular, flexible composite polymer electrolyte, consisting of a polymer matrix, lithium salts, and ceramic fillers, provide good mechanical properties and high electrochemical performance, and improved better interfacial compatibility, while also overcoming safety limitations [150]. Within this class, polyethylene oxide (PEO) based composite electrolytes (PCEs) are considered among the most promising systems due to their low cost, non-toxicity and good compatibility with lithium salts [151]. Within LMBs, the PCE can react with the metallic lithium anode and form a solid electrolyte interface (SEI) layer, while enabling transport of Li^+. However, the unstable SEI limits the columbic efficiency (CE) and is ineffective at inhibiting the harmful dendrite growth [152-154]. Despite its importance, the Li platting/stripping process is still not clearly understood and requires further investigation to overcome these hurdles. Indeed, improved understanding of how the structure and morphology of the PCE evolves during the Li platting/stripping process is of particular significance for realization of high-performance all-solid-state LMBs via rational design and modification of electrolytes.

Synchrotron radiation-based X-ray probes are among the most effective methods for in-situ or operando studies of LMBs, offering high luminance and flux, a large range of photon energies, as well as non-destructive ability. Previous studies showed the possibility of utilizing synchrotron-radiation based X-ray analytical facilities to take insights into LIBs. For instance, by using the synchrotron-radiation based X-ray absorption spectroscopy (XAS), Zhang et.al. [155] obtained information on the Li-ion

transport and chemical environment of xLi_2O-MCl_y materials; while Conder et.al. [156] using synchrotron-radiation based X-ray diffraction (XRD) to identify the absorption of polysulfide on the surface of separator and the behavior at the electrode/electrolyte interface. Nevertheless, the abovementioned techniques mainly focus on the Li/electrolyte interface instead of providing more details about the inner morphology and the crystal orientation evolution of the electrolyte during cycling. When tuning the incident angle of the X-ray beam to grazing incidence conditions (< 1°), methods such as grazing incidence small-angle X-ray scattering (GISAXS) and grazing incidence wide-angle X-ray scattering (GIWAXS) can provide more valuable information from a larger area due to the large footprint on the buried morphology, structure, and orientation of the bulk film. With this in mind, I utilize simultaneous operando GISAXS and GIWAXS measurements to Li||Cu cells together with cyclic voltammetry (CV) electrochemical testing to probe the morphology and structure evolution within the electrolyte. The sample position system with specific detector pixel size and sample-to-detector distance help us to realization the spatial resolution. The high brilliance synchrotron X-ray source and fast readout time of detector supported the temporal resolution. To exclude any additive effects on the lithium plating/stripping process, a basic PCE electrolyte consisting of the PEO matrix, LiTFSI salt, and Al_2O_3 inorganic filler without further modification is used in a Li||Cu cell. Through a comprehensive approach that incorporates CV sweeps, I investigate the mechanisms underlying the crystalline/crystallite orientation and morphology evolution of electrolytes and their interaction with electrochemical reactions in the nanoscale. This research focus on elucidating the properties and behavior of the electrolyte with real-time GIWAXS/GISAXS monitoring and completing the blank area on composite electrolyte research. Our investigation not only sheds light on these fundamental mechanisms but also opens up new paths for the designing of composite electrolytes tailored for next-generation lithium metal batteries.

5.2 Set-up for operando GISAXS/GIWAXS measurements

Figure 5.1a shows a sketch of the operando setup, where the electrochemical cell is connected to the CV test and the X-ray beam directly impinges on the electrolyte by a cut slit in the metallic lithium anode. Figure 5.1b shows the CV curve recorded during the GISAXS and GIWAXS measurements. The CV test and GISAXS/GIWAXS measurements have been discussed in Chapter 3. In the cathodic sweep, the broad and

weak peak observed at around 1.95 V belongs to the initial formation of Li_xCuO. With sweeping, the peaks at around 1.57 and 1.15 V correspond to the reduction of PEO-Li^+ where the coordination bond is degraded under voltage [157], and the decomposition of $TFSI^-$ [158] happens for the SEI layer formation, respectively. The peaks at around 0.62 V and in the 0.03 – 0.25 V region correspond to the Li^+ deposition process. In the oxidation process, the peak at 0.88 V is considered as the Li^+ stripping process, corresponding to the Li^+ depositing process at around 0.62 V of the reduction process. The two decomposition peaks are not observed from the oxidation process due to an irreversible electrochemical reaction. Two broad peaks at 2.07 and 2.41 V can be attributed to the oxidation of Cu to Cu_2O and CuO. In the following sections, four representative CV peaks are select to analyze. Selected typical 2D GISAXS and 2D GIWAXS data are shown in Figure 5.1c at the initial, middle, and final operation voltage obtained during the operando measurement. I note that due to the simultaneous GISAXS/GIWAXS measurement setup, the 2D GIWAXS data have a missing square (for the GISAXS detector) at lower q values (Figure 5.1c). To assess the consistency of our operando setup and coin cell configuration, a CV sweep is conducted on a Li||Cu coin cell (Figure 5.2). Despite the different currents, the electrochemical reactions remain consistent with those depicted in Figure 5.1b, demonstrating the effectiveness of our operando setup.

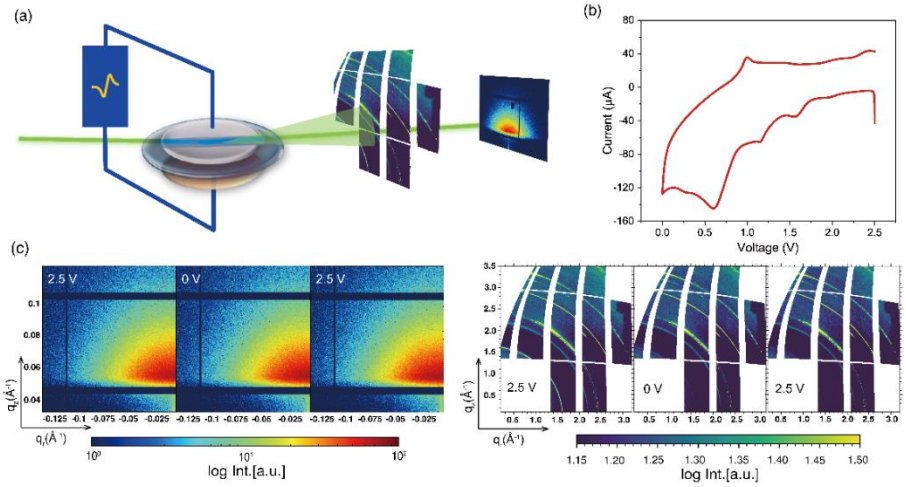

Figure 5.1. *Overview of the operando experiment. (a) Sketch of the operando study of a Li|PEO composite electrolyte|Cu cell by synchrotron-radiation-based simultaneous GISAXS and GIWAXS measurements, (b) recorded CV profile of the above-mentioned cell during the GISAXS/GIWAXS measurement, and (c) selected operando 2D GISAXS and 2D GIWAXS data. Reproduced with permission from [19]. Copyright 2024 by the authors. Published by American Chemical Society.*

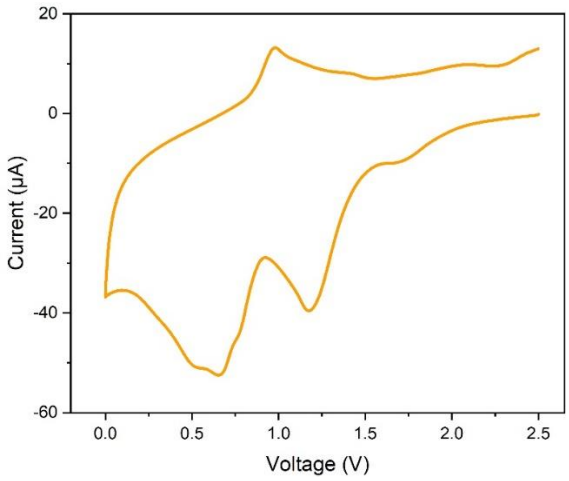

Figure 5.2. *Cyclic Voltammetry profile of Li||Cu coin cell with a scan rate of 5 mV/s. Reproduced with permission from [19]. Copyright 2024 by the authors. Published by American Chemical Society.*

5.3 Crystalline structure evolution

The evolution of the crystal structure of the PCE is investigated by operando GIWAXS during electrochemical CV measurements. For each scattering image, the data acquisition time is 1 s, and the time interval between two images is 12.5 s.

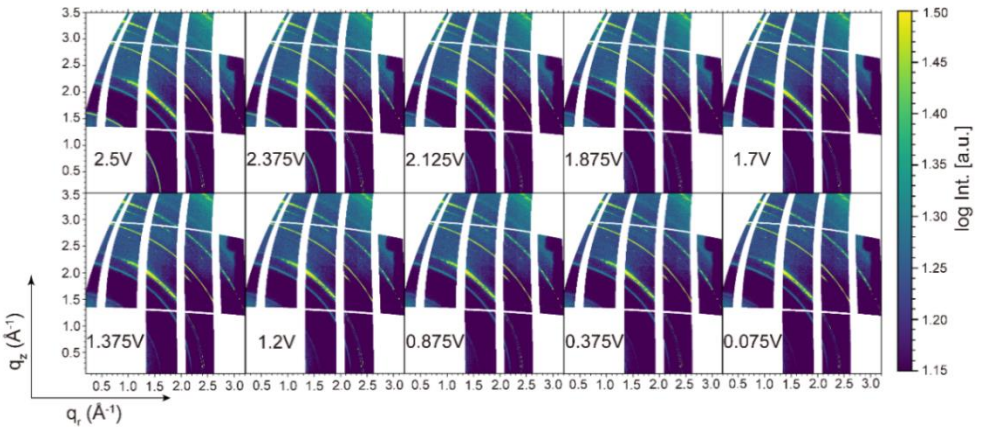

Figure 5.3. *Selected 2D GIWAXS data of the Li| PEO composite electrolyte |Cu cell at different operational voltages from 2.5 to 0 V. Reproduced with permission from [19]. Copyright 2024 by the authors. Published by American Chemical Society.*

The reshaped 2D GIWAXS data from 2.5 to 0 V and from 0 to 2.5 V are shown in Figures 5.3 and 5.4, respectively. The Bragg rings in the 2D GIWAXS data originate

from the crystalline part in the PCE. From the 2D GIWAXS data, we observe a diminishing intensity ring located at 1.6 $Å^{-1}$ (Figure 5.3) in the reduction process of the CV (2.5 V – 0 V).

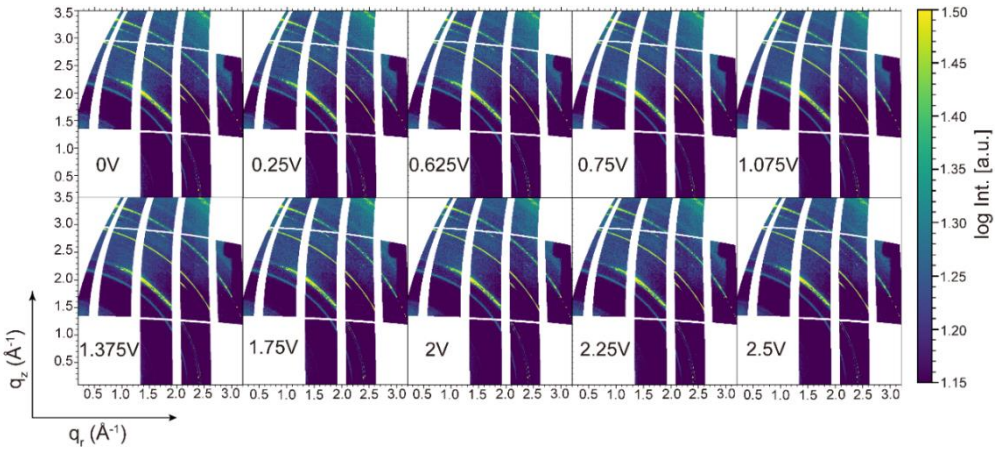

Figure 5.4. *Selected 2D GIWAXS data of the Li| PEO composite electrolyte |Cu cell at different operational voltages from 0 to 2.5 V. Reproduced with permission from [19]. Copyright 2024 by the authors. Published by American Chemical Society.*

To visualize the changes, a contour plot of the cake cuts of 2D GIWAXS data in the range of (0°, 90°) in the χ direction is performed. The whole range of contour plot is given in Figure 5.5a, and the Pseudo-XRD data is extracted from the 2D GIWAXS data as seen in Figures 5.5b. The enlarged contour plot and Pseudo-XRD data at 1.6 $Å^{-1}$ is shown in Figure 5.6a and b, respectively [159-160]. By comparison with the literature, it is widely recognized that the peaks observed at q = 1.6 $Å^{-1}$ and q = 2.2 $Å^{-1}$ correspond to the coordination peak of the PEO-LiTFSI coordination group [161-163]. For further analysis, we designate the peak at q = 1.6 $Å^{-1}$ as our domain peak. The intensity decrease is attributed to the reduction process of the PEO-Li^+ group at 1.57 V in CV (Figure 5.1b) where the coordination bond unfolds to release free Li^+ for further deposition. Notably, this commonly used coordination peak needs two subpeaks for modeling the intensity peak at 1.6 $Å^{-1}$, indicating the existence of both, the PEO subpeak (green line) and the LiTFSI subpeak (red line), as shown in Figure 5.4c. In addition, with the applied voltage changing, also the intensity of both subpeaks changes. Initially, the coordination peak originates from LiTFSI because less EO chains can participate in the coordination with LiTFSI due to the semicrystalline nature of PEO [164-165].

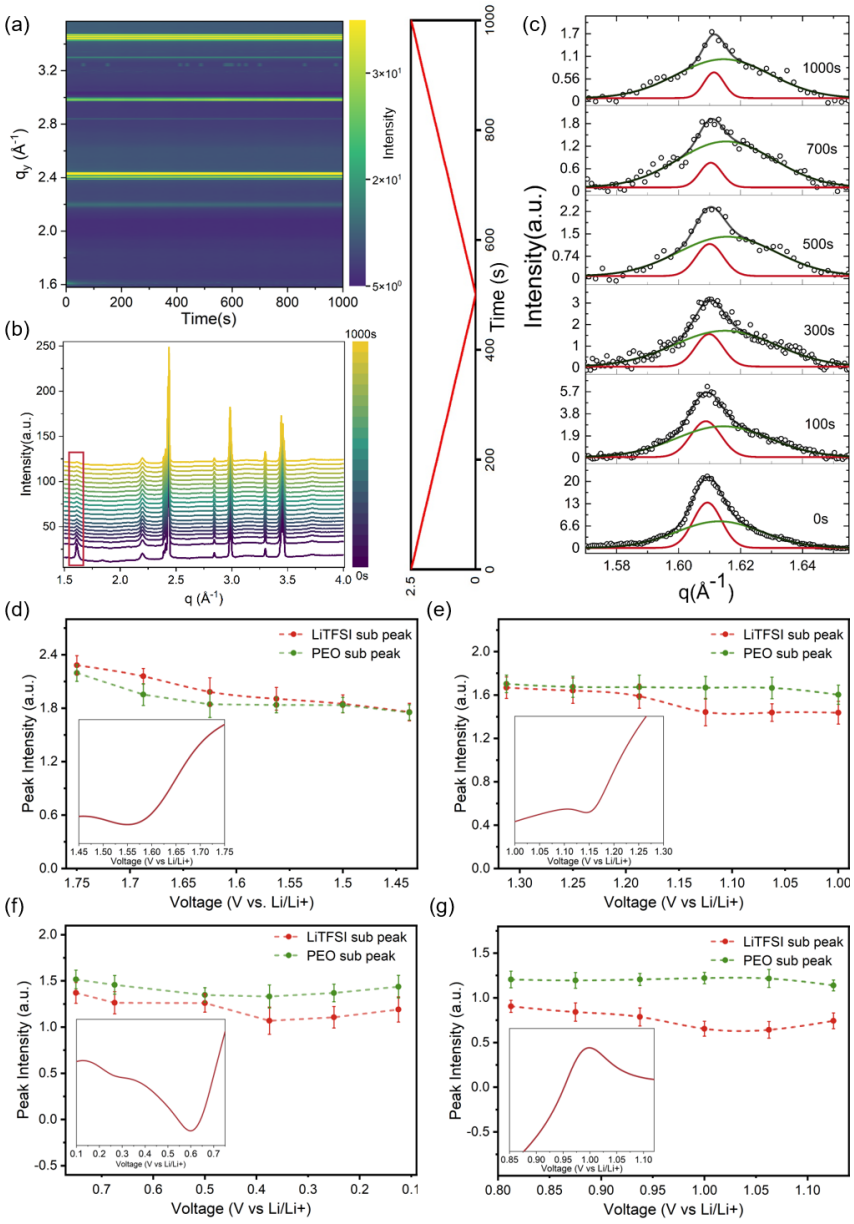

Figure 5.5. *Crystalline structure evolution of the PEO composite electrolyte. (a) Temporal contour 2D plot and (b) pseudo XRD curves acquired from cuts of the 2D GIWAXS data, with time-voltage function on the right. (c) Zoom-in of the peak at q_y = 1.6 Å^{-1} probed at different CV operation times. This peak originates from the PEO-Li coordination peak. The data (symbols) are shown together with their fits (lines), which have contributions from LiTFSI sub-peak (red) and PEO sub-peak (green). (d-g) Intensity of the LiTFSI sub-peak and the PEO sub-peak as function of the CV voltage sweep with inserted corresponding electrochemical reaction peak in the CV curve. Reproduced with permission from [19]. Copyright 2024 by the authors. Published by*

American Chemical Society.

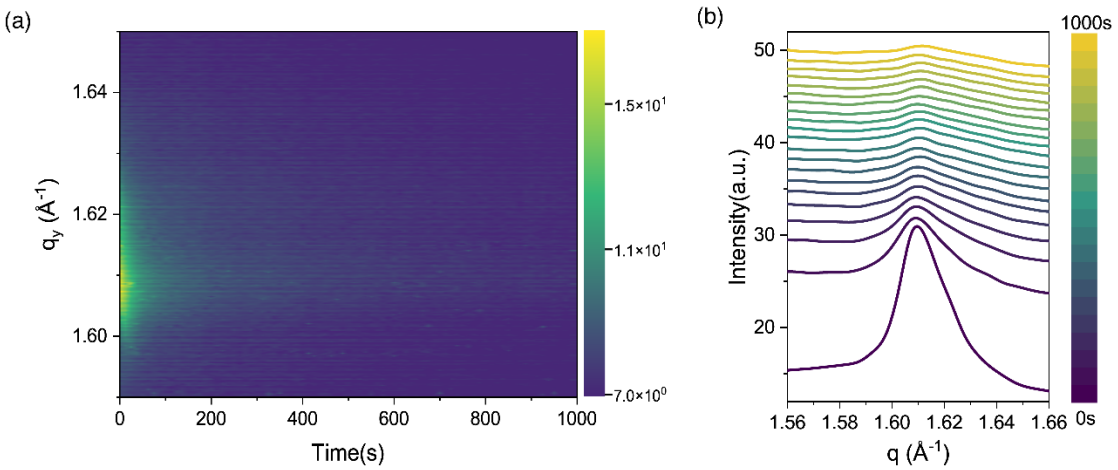

Figure 5.6. *Enlarged contour plot (a) and pseudo XRD cuts (b) in the q_y = 1.6 Å^{-1} region. Reproduced with permission from [19]. Copyright 2024 by the authors. Published by American Chemical Society.*

During the voltage sweep, the PEO contribution to the coordination peak becomes dominant. To quantitatively analyze the evolution of both sub-peaks, we model the pseudo XRD data and extract the intensity, full width at half maximum (FWHM), and peak position shifts of two sub peaks during the CV test, as shown in Figure 5.7-5.9, respectively. The electrochemical process modifies the coordination interaction between PEO and LiTFSI, as evidenced by the scattering results. To visualize the relationship of sub-peaks intensity evolution and reduction/oxidation peaks observed in the CV curve, as shown in Figure 5.5d-g, we select four representable CV peaks accompanied by the intensity of both peaks across different voltage intervals. As shown in Figure 5.5d, when the voltage decrease from 1.75 V to 1.45 V, the peak is mainly caused by LiTFSI, and the intensity of both PEO and LiTFSI sub-peaks is decreasing, indicating that both phase joined the first electrochemical reaction in the PCE, namely the PEO-Li^+ reduction reaction, under the driving force of the applied potential. When the voltage is further decreased from 1.3 V to 1 V (Figure 5.5e), the $TFSI^-$ reduction reaction and the SEI formation starts as indicated by the decreased intensity of the LiTFSI sub-peak. In contrast to LiTFSI, the intensity of PEO sub-peak becomes dominant in the coordination peak and its intensity remains stable. In the lithiation process, the intensity of the PEO sub-peak shows a slight decline followed by an increase, while the sub-peak of LiTFSI shows the opposite trend within the voltage range from 0.7 V to 0.1 V of Li platting process (Figure 5.5f). This phenomenon can be

attributed to the diffusion of Li ions from Li metal side to Cu side. When the last clear Li stripping CV peak is reached, as shown in Figure 5.5g, the intensity of the LiTFSI sub-peak decreases from 0.8 to 0.6 while the intensity of the PEO sub-peak increases. This trend suggests that Li^+ from Cu side diffused through the PEO segment to the Li side. However, the intensity of coordination peak not increases again, meaning that the free Li ions cannot be incorporated again within EO chains to form the PEO-Li^+ bond. Thus, throughout the entire CV sweep, the evolution of LiTFSI and PEO sub-peaks align consistently with the electrochemical reactions. Apart from the intensity change, the increased FWHM is attributed to the lower crystallinity of the PEO in the coordination peak induced by the voltage stimulus (Figure 5.8). These observations collectively suggest the presence of a more amorphous phase within the PCE, facilitating the Li+ transport process. Moreover, the decreased FWHM of the LiTFSI sub-peak originates from residual LiTFSI, which cannot coordinate with the PEO chains at room temperature. The shrink of lattice distance, inferred from the peak position in Figure 5.9, indicates the existence of stress within the electrolyte, as well as the irreversibility of both components following the processes of Li plating and stripping, leading to adverse effects on the electrochemical performance of the cell.

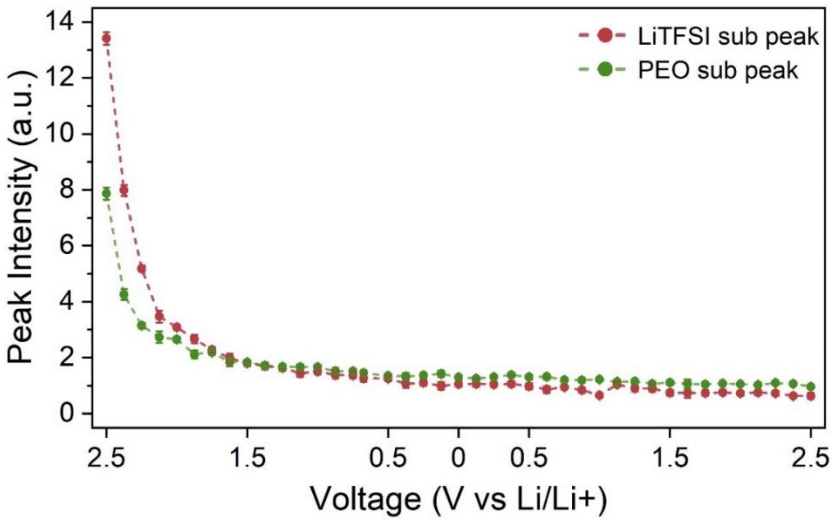

Figure 5.7. *Peak intensity of the LiTFSI sub-peak (red) and the PEO sub-peak (green) as function of the CV voltage sweep. Note that the sweep direction was reversed at 0 V. Reproduced with permission from [19]. Copyright 2024 by the authors. Published by American Chemical Society.*

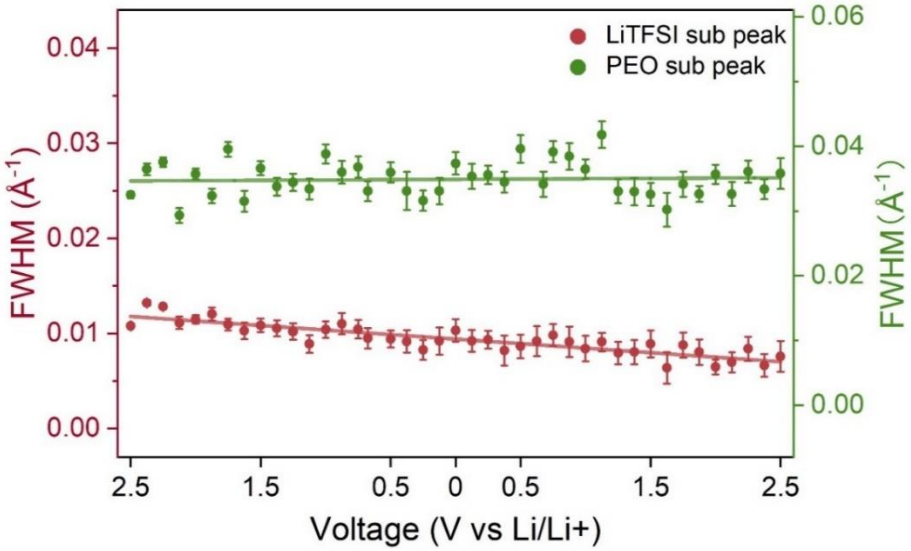

Figure 5.8. *Full width at half maximum (FWHM) of the LiTFSI sub-peak (red) and the PEO sub-peak (green) as function of the CV voltage sweep. Note that the sweep direction was reversed at 0 V. Reproduced with permission from [19]. Copyright 2024 by the authors. Published by American Chemical Society.*

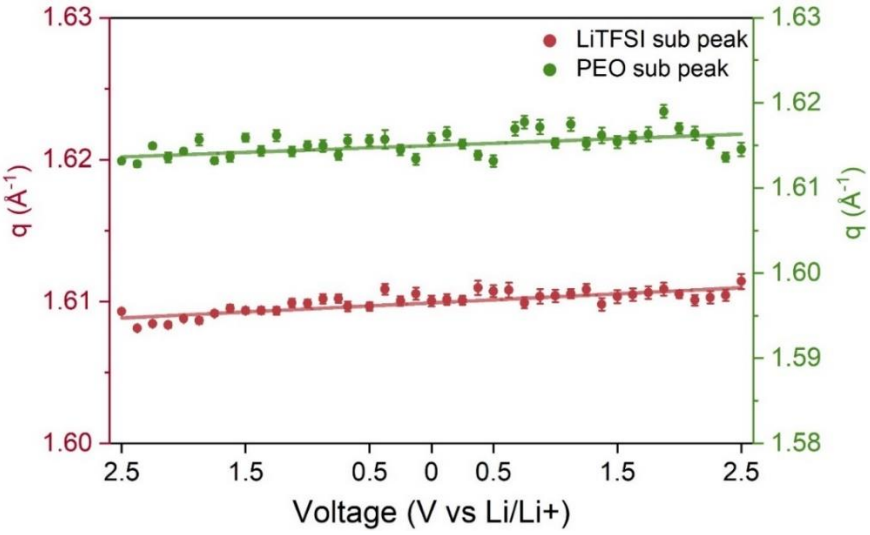

Figure 5.9. *Peak position evolution of the LiTFSI sub-peak (red) and the PEO sub-peak (green) as function of the CV voltage sweep. Note that the sweep direction was reversed at 0 V. Reproduced with permission from [19]. Copyright 2024 by the authors. Published by American Chemical Society.*

In contrast to powder X-ray diffraction (XRD), GIWAXS offers insights into the preferred crystal orientations. Therefore, in addition to the cake cuts, azimuthal tube cuts are performed at q_y = 1.6 Å^{-1} to obtain the preferred crystallite orientation

information. The schematic representation of edge-on and isotropic oriented crystallites is given in Figure 5.10a. In edge-on oriented structure, the crystallite is in a perpendicular direction to the film, while in isotropic oriented structure, the arranging of crystalline is disordered, and the crystalline is in all directions to the film [166]. The PEO-Li demonstrates an edge-on orientation at approximately χ = 20° and 80°, as shown in Figure 5.10b, aligning with crystals oriented in a 20° and 80° direction to the substrate before the voltage sweep. The crystallite orientation as a function of voltage change manifests a more disordered status in the PCE, as shown with the tube cuts at different voltage in Figure 5.10c-e, transforming from an edge-on dominant to an isotropic structure. The isotropic orientation exhibit that the EO chains arrange in all directions therefore provide more Li^+ transport pathway, which is beneficial for the Li^+ plating and stripping process. The observed orientation transformation is attributed to electrochemical reactions within the PCE, specifically PEO-Li^+ reduction and $TFSI^-$ decomposition. These processes result in the breakdown of large oriented polymer chains into smaller disordered segments, facilitating subsequent Li^+ transport. It is important to note that an irradiation damage test was conducted on the PCE for 1000 s before the *operando* measurements to rule out any possible damage caused by the X-ray beam (contour plot of horizontal line cuts in Figure 5.11).

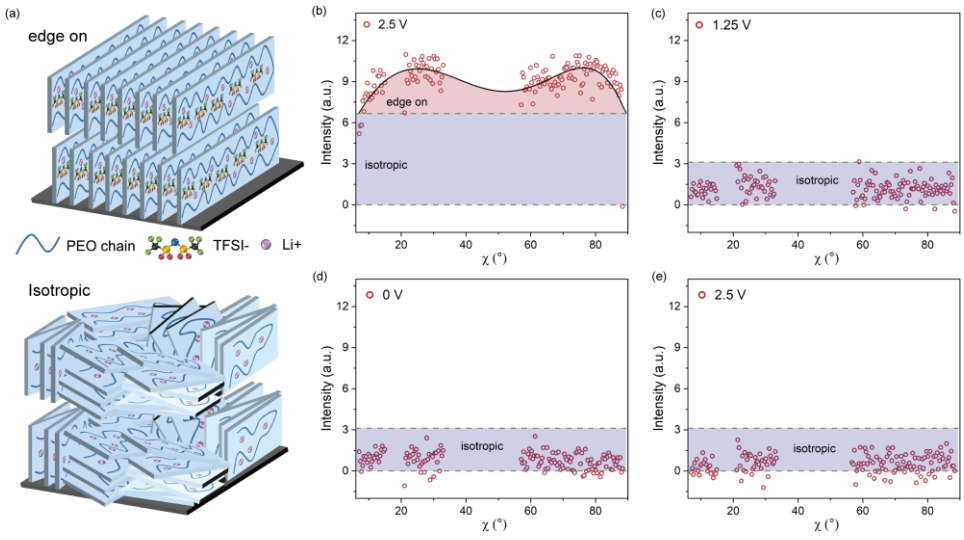

Figure 5.10. *Crystalline orientation evolution of the PEO composite electrolyte. (a) Illustration of the orientation changes from edge on orientation to isotropic arrangement. Azimuth tube cuts (points) with fits (lines) of 2D GIWAXS data at qy = 1.6 Å^{-1} during the CV sweep: (b) 2.5 V (0s), (c) 1.25 V (250s), (d) 0 V (500s), and (e) 2.5 V (1000s). Reproduced with permission from [19]. Copyright 2024 by the authors. Published by American Chemical Society.*

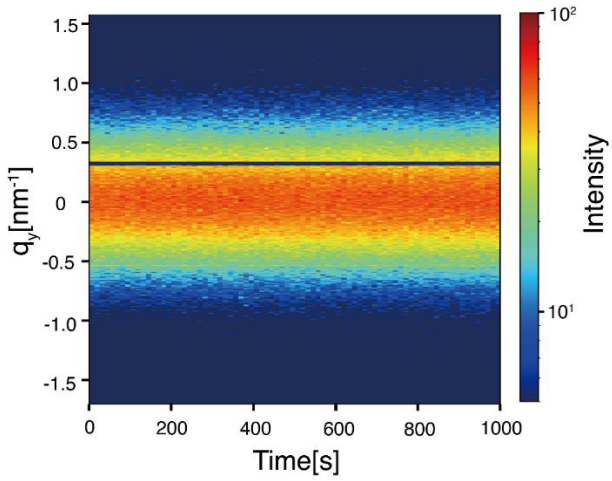

Figure 5.11. *Radiation damage test of the PEO composite electrolyte. Reproduced with permission from [19]. Copyright 2024 by the authors. Published by American Chemical Society.*

5.4 Buried Morphology Evolution

In addition to the crystalline structure obtained via *operando* GIWAXS, electrochemically-induced changes to the internal morphology of the PCE are detected with the simultaneously performed *operando* GISAXS measurements. The grazing incidence angle of 0.4° is chosen to be above the critical angle of each component in the PCE, which ensures that the inner morphology of this material is probed [131-167]. The selected 2D GISAXS data at different operation time is given in Figure 5.12.

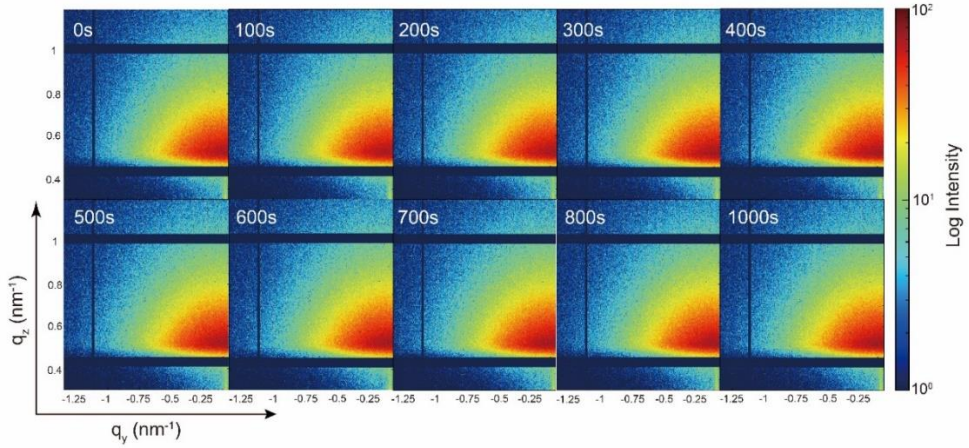

Figure 5.12. *Selected 2D GISAXS data of Li| PEO composite electrolyte |Cu cell at different operation time. Reproduced with permission from [19]. Copyright 2024 by the authors. Published by American Chemical Society.*

The horizontal line cuts are conducted at the Yoneda peak region of the PCE to quantitatively analyze the morphology evolution. The line cut data is modeled in the framework of the Distorted Wave Born Approximation [168-169]. Figure 5.13a and b shows the horizontal line cuts with best fits in a series of voltage changes. From these fits the form factor (radius) and structure factor (center-to-center distance) are extracted as shown in Figure 5.14. During the negative CV sweep (from 2.5 V to 0 V), the radius of the PEO-LiTFSI domains increases from 3 nm to 3.4 nm, and the related center-to-center distances show the same trend by increasing from 240 nm to 310 nm. In the second step of the CV (from 0 V to 2.5 V), the radius and the center-to-center distance show a reversed tendency and change into smaller radius and shorter distance.

Notably, the changes of radius and distance during the CV test are in accordance with the observed peaks shown in Figure 6.1b. Similarly, the radius and center-to-center distance changes at various voltage intervals are extracted along with the corresponding reduction/oxidation CV peaks, as shown in Figure 5.13c-f. When the voltage sweeps from 1.75 V to 1.45 V (Figure 5.13c), the distance increase from 290 nm to 300 nm, consistent with the PEO reduction reaction. The increase in distance and radius implies that Li ions escape from the PEO-LiTFSI coordination group for further reaction. With voltage continuous decrease to 1 V (Figure 5.13d), the distance expands from 300 nm to 310 nm as well as the radius increases to 3.5 nm, indicating the reduction and decomposition of $TFSI^-$ anions, and SEI formation [170-171].

In the underpotential deposition of Li at 0.62 V and in the voltage range of 0.25 - 0.03 V according to the CV curve (depicted in Figure 5.13e), a decrease in radius of PEO domains is observed. However, no concurrent change in the distance between two domains is seen. This finding suggests that the Li^+ diffusion is undergoing through the EO chain. As a consequence of a number of free Li^+ transporting to Cu side a continuous formation and breaking of the Li-O bond with each ether oxygen atom from PEO domains occurs. This process contributes to the diminishing radius of the PEO domain. Furthermore, it is noteworthy that ion diffusion does not induce a movement in the EO chain, thereby maintaining the unchanged distance between each domain. With voltage continuous increase (Figure 5.13f), the PEO domain radius continues to decrease while the distance remains constant, indicating that Li^+ can transport into the PCE through the polymer chain segments, but cannot reform the PEO-Li^+ coordination groups [172].

I tabulated the observed crystalline structure and buried morphology variations across various sweep voltages, together with the corresponding electrochemical reactions. These comprehensive findings are detailed in Table 5.1, providing a summary of the

relationship between sweep voltage and the associated structural and morphological modifications, as well as the electrochemical responses.

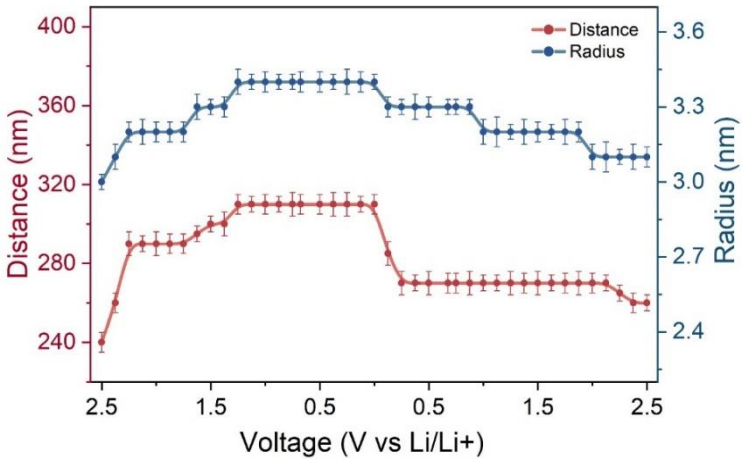

Figure 5.14. *Extracted fit parameters in terms of radius (blue) and center-to-center distance (red) of the PEO-LiTFSI domains as function of the applied voltage during CV sweep. Note that the sweep direction was reversed at 0 V. Reproduced with permission from [19]. Copyright 2024 by the authors. Published by American Chemical Society.*

Table 5.1. *Summary of the crystalline structure and buried morphology changes at different swept voltage and electrochemical reactions.*

Voltage from CV (V vs Li/Li+)	Electrochemical reactions	Crystalline structure	Morphology
1.57	EO-Li reduction	Intensity of both sub peaks decreaed then increased, and orientation becomes more isotropic.	EO-Li domain shows larger radius, and the distance between each domains increased.
1.15	TFSI- decomposition	Only LiTFSI sub-peak shows decreased intensity.	Radius and distance of domains continuously increasing.
0.62	Li+ plating	Intensity of both sub peaks decreaed then increased.	Li+ transporting process, only the domain radius changes.
0.88	Li+ stripping	Reversed tendency of Li+ plating process.	Li+ transporting process, only the domain radius changes.

5.5 Electrochemical Performance

Apart from the cyclic voltammetry, which has been collected in the *operando* measurement, the electrochemical and cycling performance are presented in Figure 6.15 to prove the effectiveness of the PCE in a coin cell framework. As seen from the electrochemical performance shown in Figure 5.15a, the PCE exhibits a good electrochemical stability with an ionic conductivity of 1.34×10^{-4} S cm^{-1} and a broadened electrochemical window up to 4.8 V (Figure 5.15b) in spite of the oxidation of the –OH group above 4 V (vs Li/Li^+) [173-174]. These results show that the dissociation of $TFSI^-$ with PEO chains sets off more free Li^+ ions to increase conductivity and protects the EO chain from oxidation [175-176].

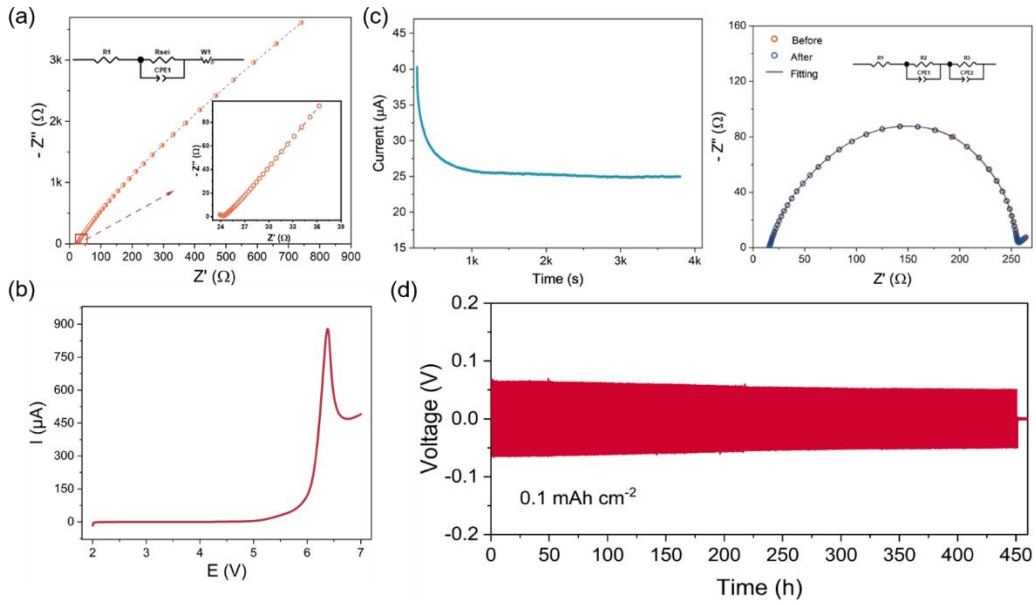

Figure 5.15. *Electrochemical measurement on PCE in coin cell configuration. (a) Impendence spectra for calculation of the ionic conductivity. (b) Linear sweep voltammetry curve of the PEO composite electrolyte for the electrochemical window. (c) Steady current as a function of time recorded during 10 mV polarization on the Li symmetric coin cell and EIS plots before and after the polarization. (d) Voltage-time profile of the Li symmetric coin cell measured at a current density of 0.1 mA* cm^{-2}*. Reproduced with permission from [19]. Copyright 2024 by the authors. Published by American Chemical Society.*

Li symmetrical cells are assembled to further estimate the stability of the PCE to the Li anode (Figure 5.15c). The PCE presents a high Li^+ transference number of 0.38, and a

minor elaboration of interfacial resistance before and after polarization. Accordingly, the symmetric cell containing PCE electrolyte displays an excellent long-term stability (Figure 5.15d) over 450 h at 0.1 mA cm^{-2}, coupling with a steady overpotential of 96 mV, which is ascribed to the good ionic conductivity and Li^+ transfer number. With the confirmed stability of PCE to Li metal, it proves the feasibility of PCE-based LMBs and are consistent with prior literature reports [177-182].

5.6 Summary

In summary, we have investigated the evolution of the buried morphology and crystalline structure of PCE within the Li||Cu cell under bias during cyclic voltammetry sweep by synchrotron-radiation based simultaneously operando GISAXS and GIWAXS measurements. The electrochemical reactions within the PCE are strongly related to the observed morphology and structure changes. When the PCE undergoes the PEO reduction process, the PEO-LiTFSI domain radius and the center-to-center distance increase, while the intensity of the PEO-Li^+ coordination Bragg peak decreases due to the disconnection of the PEO-Li^+ coordination bonds. Moreover, the increase in the PEO-LiTFSI domain radius at a bias of approx. 1.15 V and the decreased intensity of the LiTFSI Bragg peak are observed as a result of the $TFSI^-$ decomposition reaction and SEI formation. During the Li+ stripping process at 0.88 V, the crystalline structure remains unchanged whereas inner morphology changes are ongoing, implying the Li ion diffusion but not build the PEO-Li+ bonds. Moreover, the crystallite orientation of the PCE changes from an edge-on domain to an isotropic domain type, meaning that a more disordered and amorphous structure of the PCE is generated under the applied voltage, which is beneficial for ion transport through polymer chains. In addition to this, the moderate electrochemical properties and battery performance also demonstrate the feasibility of LMBs with the probed PCE acting as the solid electrolyte. Thus, our work develops pioneering operando measurements using grazing incidence X-ray scattering techniques and contributes to an understanding of the lithium ion plating/stripping process by probing morphology and structure changes in real time, which can provide a guideline for development of high CE and high conductivity lithium metal batteries.

6 Li/electrolyte Interface Behavior for Dendrite-free Lithium Batteries

This chapter is based on the published article: Unveiling the Li/electrolyte Interface Behavior for Dendrite-free Lithium Batteries by *Operando* Nano-focus WAXS [20]. Reproduced with permission from (Y. Liang, F. A. C. Apfelbeck, K. Sun, Y. Yan, L. Cheng, G. Pan, T. Zhang, Y. Cheng, A. Davydok, C. Krywka, and P. Müller-Buschbaum, Advanced Science 2024, 2414714, DOI: 10.1002/advs.202414714).

Poly(ethylene oxide) (PEO)-based solid composite electrolytes suffer from poor conductivity and lithium dendrite growth, especially toward the metallic lithium metal anode. In this study, succinonitrile (SN) is incorporated into PEO composite electrolyte to fabricate an electrode-compatible electrolyte with good electrochemical performance. The SN-doped electrolyte successfully inhibits the lithium dendrite growth and facilitates the SEI layer formation, as determined by the *operando* nanofocus wide-angle X-ray scattering (nWAXS), meanwhile, stably cycled over 700 h in Li\SN-PEO\Li cell. Apart from the observation of lithium dendrite, the robust SEI layer formation mechanism in the first cycle is investigated in the SN-enhanced composite electrolyte by nWAXS. The inorganic electrochemical reaction products, LiF and Li_3N, are found to initially deposit on the electrolyte side, progressively extending toward the lithium metal anode. This growth process effectively protected the metallic lithium, inhibited electron transfer, and facilitated Li^+ transport. This study not only demonstrates a high-performance interfacial-stable lithium metal battery with composite electrolyte but also introduces a novel strategy for real-time visualizing dendrite formation and SEI growth directing at the interface area of electrolyte and metallic lithium.

6.1 Preface

The pursuit of interfacial stable lithium metal batteries (LMBs) has been a longstanding challenge in the field, particularly since metallic lithium replaces graphite as an anode material. Conventional LMBs, which use flammable liquid electrolytes such as ether-based electrolyte and carbonate-based electrolyte, pose potential safety hazards like leakage, ignition, and even explosions [183-184]. Furthermore, the highly active lithium metal anode easily reacts with electrolytes, leading to uncontrollable and infinite lithium dendrite growth, which remains the key bottleneck for long-life stable LMBs [103]. The concurrent formation of a solid electrolyte interface (SEI) layer can prevent the direct contact of Li metal and electrolyte. However, the SEI layer can be easily destroyed by its volume expansion, resulting in cell failure. Efforts have been made to address this challenge through various strategies. For instance, researchers have utilized electrolyte solvation chemistry to regulate carbonate-based electrolytes, achieving stable cycling at low temperatures [185]. Additionally, carbonate materials have been employed to mediate low-concentration ether-based electrolytes, enabling stable cycling at high voltages [186]. Furthermore, tuning intermolecular interactions to design nonflammable fluorinated electrolyte for high-voltage wide temperature cycling [187], and building Li-intercalated interlayer as fast Li+ conducting channels and Li protection structure [188] can also support the stable high-voltage cycling of LMBs.

Neverthless, replacing the organic liquid electrolyte with a solid electrolyte is a crucial step for enhancing safety and expanding the potential applications of LMBs. With all the challenges, significant efforts over the past decades have focused on developing new electrolyte materials, such as sulfide-based $Li_xPS_yCl_{6-y}$ argyrodite electrolyte [189-190], oxide-based LLZO garnet electrolyte [191-192], and polymer-based electrolyte [193-194]. Each type has advantages and limitations. Ceramic electrolytes offer high ionic conductivity but are brittle, while polymer electrolytes are flexible but lack sufficient mechanical strength [145]. In contrast, composite electrolytes, consisting of a polymer matrix reinforced with inorganic fillers, inherent the advantages of both polymer and ceramic electrolytes, offering mechanical flexibility along with enhanced stability and conductivity [195]. This makes composite electrolytes a promising solution for achieving interfacial stability in lithium metal batteries.

The low-cost poly(ethylene oxide) (PEO) composite electrolyte stands out as the promising candidate due to its high flexibility, strong Li^+ solubility, and excellent

processability [111]. The Li^+ transport in a PEO-based electrolyte is realized by the mobility of the ethylene oxide (EO) segments. However, the semi-crystalline nature of PEO hinders the segment motion dynamics at room temperature, resulting in a low ion conductivity ($10^{-6} \sim 10^{-8}$ S cm^{-1}) [64]. To overcome this limitation, introducing low molecular weight plasticizers, such as ester-based materials and nitrile-based materials, has been proven as an effective strategy. These plasticizers not only enhance thermal stability and reduce PEO crystallinity, but they also significantly improve ion conductivity [176-196]. Furthermore, they contribute to the formation of a stable Li/electrolyte interface composed of LiF, Li_3N, and organic components, which helps to suppress lithium dendrite penetration and improves the overall battery performance.

Currently, adjusting electrolyte compositions has enabled the development of batteries with high-voltage, fast-charging, and wide-temperature capabilities for diverse environmental conditions. However, understanding electrode interfacial behavior, the dynamics of lithium dendrite growth, and the process of SEI formation remains an open challenge despite ongoing research efforts [197]. For instance, in-situ optical microscopy can observe Li-deposited layer and lithium dendrite under varying current densities [198], while in-situ transmission electron microscopy (TEM) has captured the nucleation and growth of Li in functioning solid-state lithium metal batteries [199]. However, these techniques probe only surface information and are limited by the resolution and response times, making them difficult to kinetically capture the dynamical process. Similarly, in-situ neutron techniques, such as in-situ neutron tomography (NT) [200-201], face limitations in terms of beam size and beam energy, lacking precision and resolution, preventing the effective monitoring of lithium dendrite and SEI layer formation. In contrast, synchrotron X-ray techniques offer an innovative approach to studying various types of batteries. For example, Sun et al. employed synchrotron X-ray tomography to capture the degradation of Li-based anodes during electrochemical cycling [202]. They also employed this technique to assess the morphological reversibility of modified Li-based anode materials for next generation batteries [203]. Similarly, Lu et al. utilized synchrotron X-ray computed tomography to explore the failure mechanisms of Li/Na–CO_2 batteries [204]. Moreover, nondestructive synchrotron nanofocus X-ray scattering (nXS), which combines a high photon flux and a precise illumination area, has been widely applied in fields such as polymer science and solar cells [127-205]. The combination of high flux and nm-grade illumination area provides a unique opportunity to study growth kinetics in real-time [206]. This unique approach gives rise to the visualization of lithium dendrite growth

and SEI layer formation process when appplied together with galvanostatic cycling in LMBs.

In this work, an interfacial-stable PEO composite electrolyte is fabricated with the addition of succinonitrile (SN) for all-solid-state LMBs. With the incorporation of SN, the modified electrolyte demonstrates a high ion conductivity of 2.69×10^{-4} S cm^{-1} and Li^+ transfer number of 0.57, attributed to the reduced PEO crystallinity of 10.09 %. This results in the stable Li plating/stripping at 0.1 mA cm^{-2} over 1000 h and an increased critical current density of 0.7 mA cm^{-2}, exhibiting a superior compatibility with metallic lithium. Furthermore, the lithium dendrite growth and the SEI layer formation during the first cycle is observed by operando nanofocus wide-angle X-ray scattering (nWAXS) using a nanobeam size of 350 nm × 330 nm (H × V). The modified electrolyte in a Li symmetric cell effectively suppresses lithium dendrites by forming a stable interfacial layer primarily composed of LiF and Li_3N. More importantly, the nWAXS reveals that SEI layer formation initiates at the electrolyte side of the Li/electrolyte interface midway through the first cycle and gradually extends towards the lithium metal electrode. Such a stable SEI layer enables steady long-term charging/discharging at elevated current densities, facilitates ion transports, and mitigates further electrolyte degradation. Leveraging this knowledge, our work presents an easy and cost-effective strategy for fabricating interfacial-stable composite electrolytes for all-solid-state LMBs and offers insights into the kinetics of electrode/electrolyte interfacial behavior microscopically during cycling.

6.2 Ion conductivity and thermal behavior

The influence of SN on the conductivity and electrochemical window is investigated by electrochemical impendence spectroscopy (EIS) and liner sweep voltammetry (LSV), respectively. Figure 6.1a displays the Nyquist plot of CPEs with and without SN additives. The addition of 10 wt% SN results in an increased ionic conductivity (2.69×10^{-4} S cm^{-1}), which is much higher than that of the reference sample without additive (1.22×10^{-4} S cm^{-1}). As shown in Figure 6.1b, the introduction of SN expands the electrochemical window to over 5.35 V, thereby reducing the reaction current compared to the reference sample.

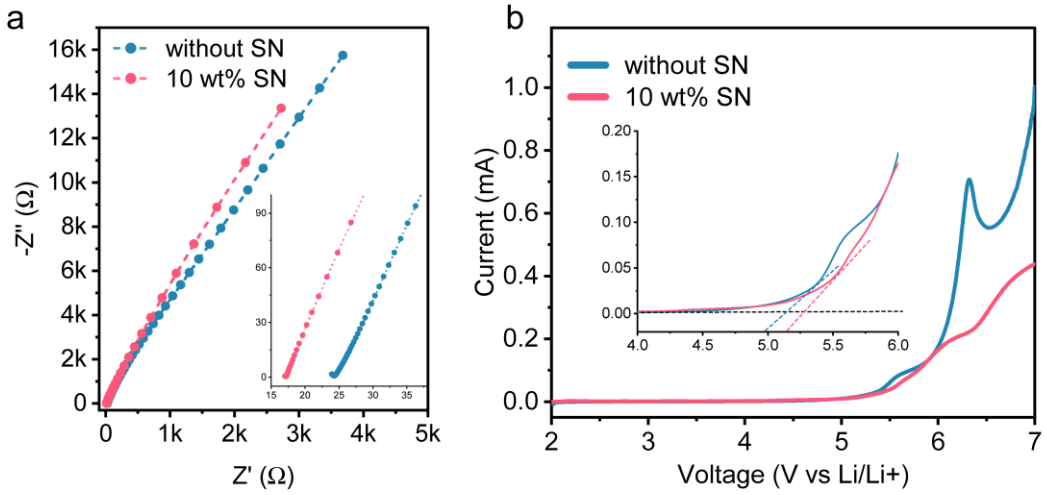

Figure 6.1. *Characterization of ion transport in PEO-xSN (x = 0 and 10) composite electrolyte. (a) Ionic conductivity of PEO-xSN at room temperature. (b) Electrochemical window of PEO-xSN electrolyte. Reproduced with permission from [20]. Copyright 2025 by the authors. Advanced Science published by Wiley-VCH GmbH.*

To satisfy the operational demands of a lithium battery for commercial applications, the composite electrolyte should exhibit a low glass transition temperature (T_g) to enhance the conductivity performance, a low melting temperature (T_m) to guarantee an effective operation at low temperatures, and a low crystallinity to facilitate the ion transport [196]. The thermal properties are evaluated using differential scanning calorimetry (DSC) and thermogravimetric analysis (TGA). Pure PEO powder possesses poor thermal properties, as shown in Figure 6.2, which present an extremely high T_m of 72.2 °C and melting enthalpy (ΔH_m) of 128.06 J g^{-1}. The heat flow curves of the reference (PEO-0SN) sample and PEO-10SN samples are shown in Figure 6.3. The addition of LiTFSI and Al_2O_3 leads to the reduction of Tm (51 °C) and ΔH_m (50.85 J g^{-1}), which can be attributed to the Lewis acid–base interactions between the ether O of the PEO chain and Lewis acid sites on the surface of Al_2O_3 [196], resulting to the disruption of PEO crystal structure. A slight increase in T_g is observed, attributing to the presence of Al_2O_3. Furthermore, the film with SN additive exhibits a further decreased T_g of -44 °C, T_m of 39.3 °C and ΔH_m of 13.95 J g^{-1}. Figure 6.4a shows the comparison of the samples with/without SN and pure PEO powder as the reference to calculate crystallinity. Notably, the PEO-10 wt% SN sample not only presents a lower T_g, T_m, and T_c, but also achieves the lowest relative crystallinity of 10.09 %. The decreased crystallinity can

increase the amorphous portion of PEO, which is beneficial for ion conductivity. Figure 6.4b shows the TGA curve of the composite electrolytes with and without additives. The slight weight loss of 4 wt% around 100 °C can be attributed to the removal of moisture or residual solvent in the film. In the reference sample (blue curve in Figure 6.4b), the major weight loss happens in the temperature window 240 - 520 °C around 80 wt%, indicating sublimation of PEO. In the PEO-10SN sample, another weight loss of 6 wt% appears at 100 - 184 °C, which can be attributed to the sublimation process of SN. Notably, not all of SN undergoes sublimation. Moreover, the decomposition onset temperature (T_d) shifts from 363.5 to 347.1°C after adding SN. This finding can be attributed to the trapping and integration phenomenon of SN in the polymer chain entanglement, and the noncovalent interaction between SN molecules and the functional groups of PEO, respectively [207]. Thus, the addition of SN is beneficial for decreasing the melting temperature and crystallinity, contributing to the high conductivity and thermal-stable composite electrolyte for all-solid-state LMBs [208-209].

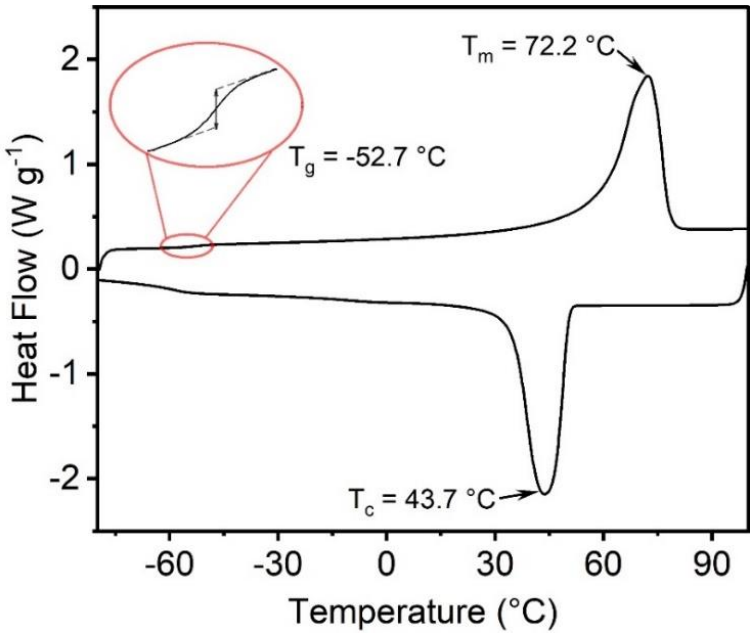

Figure 6.2. *DSC curve of pure PEO powder in the heating/cooling rage of -80 to 100 °C. The PEO powder shows a T_g of -52.7 °C, T_m of 72.2 °C, and T_c of 43.7 °C. Reproduced with permission from [20]. Copyright 2025 by the authors. Advanced Science published by Wiley-VCH GmbH.*

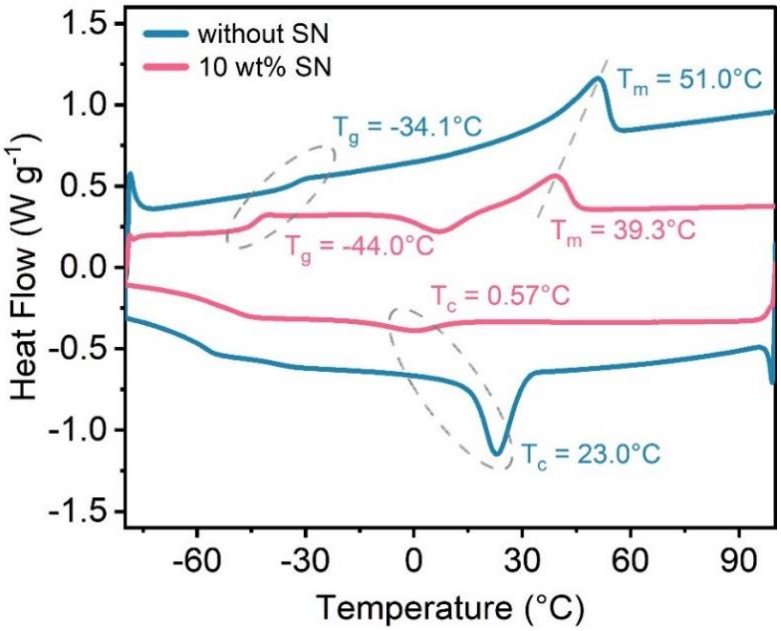

Figure 6.3. *DSC curve of PEO-0SN film (blue curve) and PEO-10SN film (pink curve) in the heating/cooling rage of -80 to 100 °C. Reproduced with permission from [20]. Copyright 2025 by the authors. Advanced Science published by Wiley-VCH GmbH.*

To further determine the chemical interaction between the PEO matrix and SN, Fourier transform infrared (FTIR) spectroscopy is conducted to analyze the coordination between the functional groups. Figure 6.5 shows the full transmittance FTIR spectroscopy in the range of 450 - 4000 cm^{-1}. Figure 6.6 displays the vibration modes of various groups: (S-N), (-CF_3), (-CH_2), (-SO_2), (C-O-C), (C≡N), and (-CH) at wavenumbers 730-750, 900-980, 1030-1200, 2230-2280, and 2750-3050 cm^{-1}. The characteristic SN peak for the C≡N stretching vibration is clearly observed at 2253 cm^{-1} [210]. After the addition of SN, the intensity of the S-N vibration from $TFSI^-$ at 740 cm^{-1} decreases [161], indicating a modification in the Li^+ solvation structure. This behavior suggests a weakening of the interaction between Li^+ and PEO, leading to the formation of ion pairs between $TFSI^-$ and PEO segments, consequently enhancing the Li^+ migration ability. The peaks located at 933 cm^{-1} and at 1100 cm^{-1} are corresponding to the -CF_3 rocking mode and to the symmetric -SO_3 stretching mode in $TFSI^-$, respectively [210-211]. Both peaks exhibit redshifts and altered peak shapes upon SN addition, which indicates enhanced intermolecular interactions between Li^+ ions and $TFSI^-$ anions.

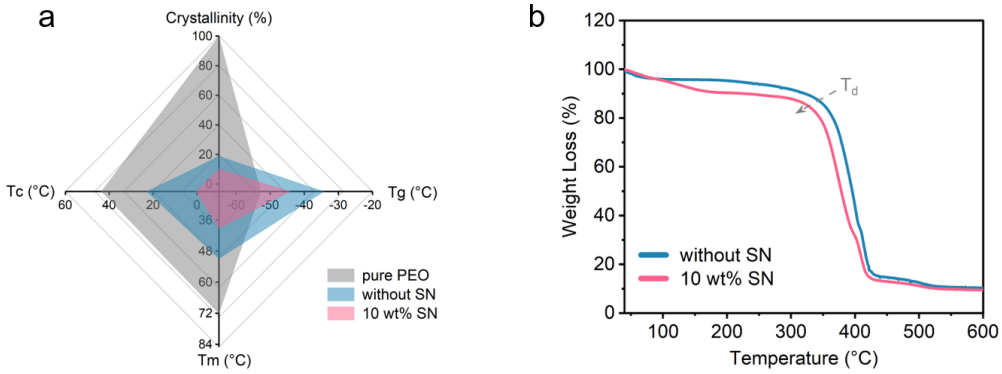

Figure 6.4. *Thermal behavior in PEO-xSN (x = 0 and 10) composite electrolyte. (a) Summary of glass transition temperature (T_g), crystallization temperature (T_c), melting temperature (T_m), and crystallinity of PEO-xSN. The pure PEO powder (grey area) acts as the reference for crystallinity. (b) TGA ranging from room temperature to 600 ℃ under Ar atmosphere of PEO-xSN. Reproduced with permission from [20]. Copyright 2025 by the authors. Advanced Science published by Wiley-VCH GmbH.*

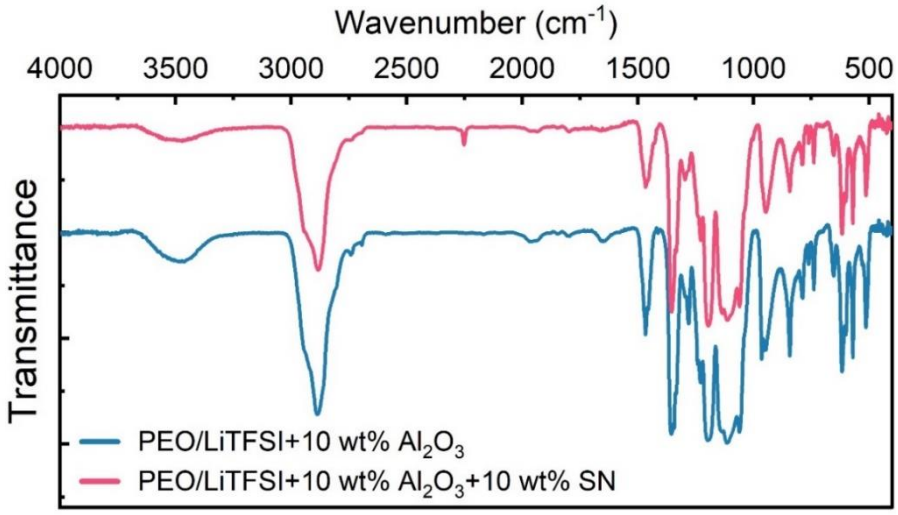

Figure 6.5. *Transmittance FTIR spectra of PEO-0SN film and PEO-10SN film in the rage of 400 - 4000 cm^{-1}. Reproduced with permission from [20]. Copyright 2025 by the authors. Advanced Science published by Wiley-VCH GmbH.*

The triplet C-O-C stretching modes are observed at 1060, 1090, and 1140 cm^{-1}, the peak at 945 cm^{-1} is associated with combined -CH_2 and C-C stretching modes, and the peak at 963 cm^{-1} originates from the mixed asymmetric and symmetric modes of -CH_2 [161-212-213]. The -CH symmetric and asymmetric peaks are at 2821 and 2939 cm^{-1}, while the peak at 2882 cm^{-1} can be attributed to -CH_2 asymmetric vibration peak [214]. With

the addition of SN, the mixed -CH_2 bond signal shifts to a lower wavenumber (from 963 to 956 cm^{-1}), and the intensity of the symmetric -CH_2 increases. Additionally, the triplet C-O-C peak exhibits a red shift (from 1060 to 1057 cm^{-1}) and merges with -SO_3 stretching peak after the introduction of 10 wt% SN. These red shifts in the C-O-C peak and -CH_2 peaks indicate that the structure of the PEO chains is modified with the assistance of SN, leading to the reduced crystallinity of PEO and expanded amorphous regions in the PEO matrix [215]. This modification enhances the ion conduction and migration, contributing to the improved electrochemical properties for the PEO-10SN electrolyte for all-solid-state LMBs.

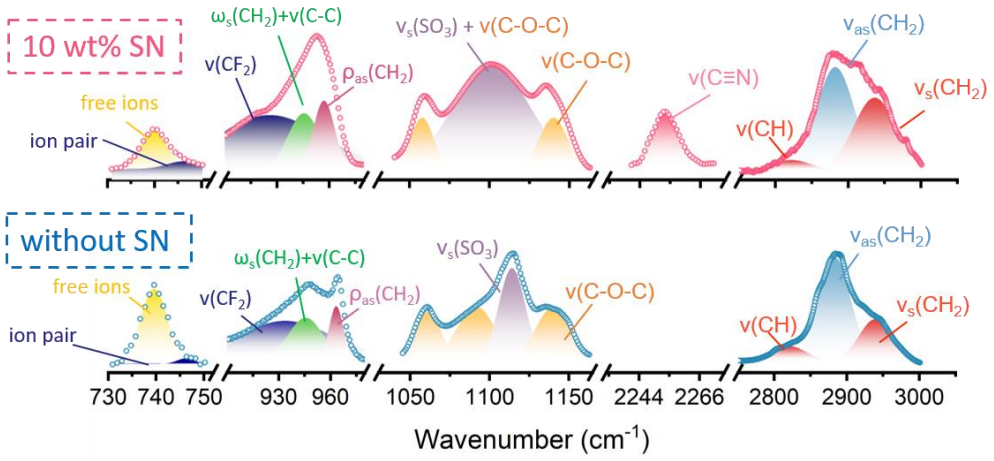

Figure 6.6. *FTIR spectra of PEO-xSN film at room temperature. Reproduced with permission from [20]. Copyright 2025 by the authors. Advanced Science published by Wiley-VCH GmbH.*

6.3 Electrochemical performance

Given its good conductivity and well thermal properties, Li symmetric cells are assembled to evaluate the compatibility of the PEO-xSN electrolyte with metallic lithium, especially the interfacial stability. The addition of SN improves the electrolyte performance, with the PEO-10SN electrolyte achieving the highest lithium transference number of 0.52, which is double that of the reference sample (t_+ = 0.27), as shown in Figure 6.7a. To investigate the long-term stability, charging/discharging cycling is applied on the Li symmetric cells, with Figure 6.7b depicting the first 500 hours of cycling.

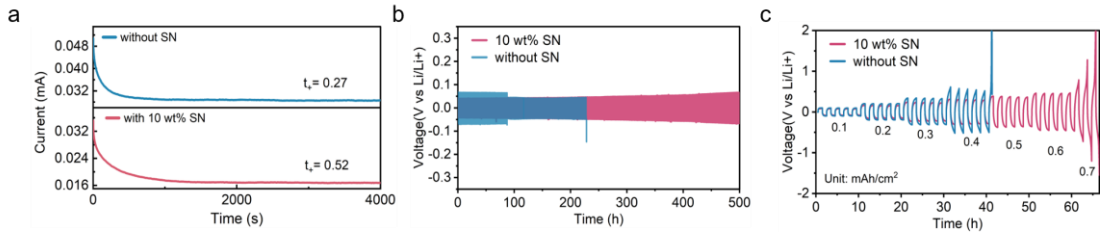

Figure 6.7. *Li symmetric cells performance of PEO-xSN (x = 0 and 10) composite electrolyte. (a) Li^+ transference number of PEO-xSN electrolyte. (b) First 500 h cycles of Li/PEO-xSN/Li cells under the current density of 0.1 mA cm^{-2}. (c) The cycling performance of Li/PEO-xSN/Li cells under increasing current density. Reproduced with permission from [20]. Copyright 2025 by the authors. Advanced Science published by Wiley-VCH GmbH.*

Due to the poor ion conducting behavior, the Li/PEO-0SN/Li cell exhibits a large initial overpotential of 135 mV at 0.1 mA cm^{-2}. Then the overpotential suddenly drops to 90 mV at 87 h, followed by a lithium dendrite penetrated short circuit at 220 h, which might be attributed to the micro short circuit inside the cell. In contrast, in the case of the 10 wt% SN addition, the cell maintains a stable performance over 500 cycles, showing no significant voltage oscillations and sustaining a low overpotential of 80 mV. Additionally, the Li/PEO-10SN/Li cell shows a superior plating/stripping behavior as the current density increases from 0.1 - 0.7 mA cm^{-2}. As shown in Figure 6.7c, the Li/PEO-10SN/Li cell exhibits no short-circuit sign up to 0.7 mA cm^{-2}, with a consistently low overpotential at each current density. The symmetric cell with PEO-0SN shows a short circuit at 0.4 mA cm^{-1}, accompanied by a large overpotential of 1160 mV, suggesting a significant increase in the interfacial resistance. This behavior is attributed to the depletion of cations at the interface and rupture and detachment of the interfacial layer under high current density [216-217].

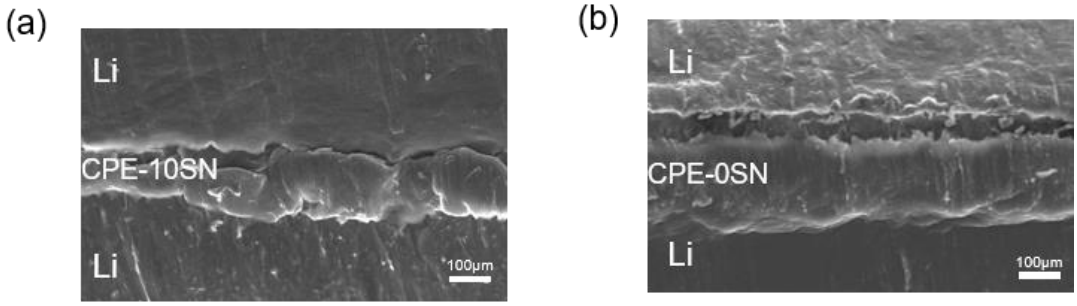

Figure 6.8. *Cross-section SEM image of (a) Li/PEO-10SN/Li cell and (b) Li/PEO-0SN/Li cell before cycling. Reproduced with permission from [20]. Copyright 2025 by the authors. Advanced Science published by Wiley-VCH GmbH.*

To further investigate the interface of the Li/electrolyte, scanning electron microscopy (SEM) is conducted on the Li symmetric cells before and after cycling under 0.1 mA cm^{-2}. Figure 6.8 shows the cross section SEM of two samples before cycling. Three layers can be clearly distinguished as Li metal, composite electrolyte, and Li metal, respectively, and no extra layer can be detected. A distance can be observed between the Li metal and composite electrolyte, regardless with or without SN, which means that the contact of electrolyte and Li metal is not good before cycling.

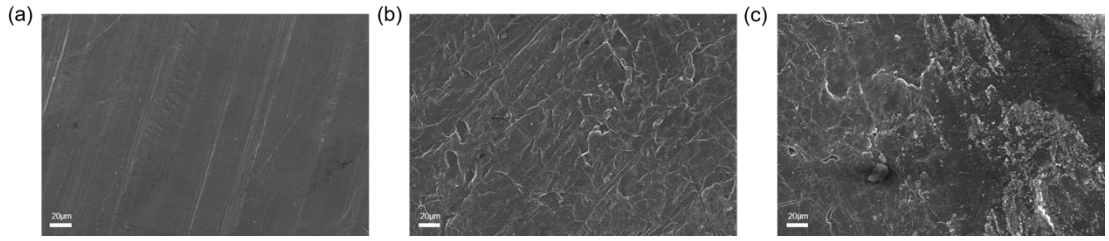

Figure 6.9. *SEM image of Li metal surface (a) Pure Li metal before cycling, (b)Li metal from Li/PEO-10SN/Li cell after cycling and (c) Li metal from Li/PEO-0SN/Li cell after cycling. Reproduced with permission from [20]. Copyright 2025 by the authors. Advanced Science published by Wiley-VCH GmbH.*

Figure 6.9 and Figure 6.10 give the SEM images of Li symmetric cells after cycling. The pure Li metal before cycling shows a very smooth surface (Figure 6.9a). As shown in Figure 6.9b and Figure 6.10a, after the Li plating/stripping process, the Li metal maintains good contact with the PEO-10SN electrolyte, and the Li metal exhibit a uniform and flat surface with no visible lithium dendrite formation. This finding suggests a uniform Li plating/stripping in the cycling process. Meanwhile, the clear high illuminance extra layer can be observed in Figure 6.10, denoted as the SEI layer. The 3D reconstruction further confirms the presence of a thick and uniform SEI layer, preventing the dendrite penetration into the electrolyte. In contrast, the symmetric cell without SN addition, seen in Figure 6.9c and Figure 6.10, suffers from dramatic damage during cycling. The lithium metal displays a mossy lithium morphology with voids. The electrolyte shows a clear separation, with large voids at the interface, indicating poor contact with the Li metal. Moreover, two lithium dendrites are observed nucleating from the Li surface, penetrating the electrolyte, and extending into the opposing Li electrode. The 3D reconstruction also reveals the absence of the SEI layer, which might contribute to the failure of the Li symmetric cell with PEO-0SN electrolyte (without SN additive). These results confirm the crucial role of SN in PEO-based electrolytes, which increases the Li^+ migration ability and ion conductivity, thereby contributing to the formation of a stable interface layer and promoting uniform Li^+ plating/stripping.

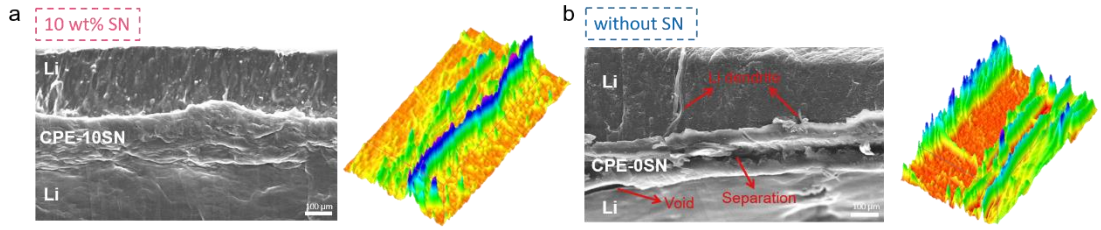

Figure 6.10. *Ex-situ cross-section SEM and 3D reconstruction image of (a) Li/PEO-10SN/Li cell and (b) Li/PEO-0SN/Li cell after cycling under 0.1 mA cm^{-2}. The color bar in 3D construction images represent the illuminance of this area. Reproduced with permission from [20]. Copyright 2025 by the authors. Advanced Science published by Wiley-VCH GmbH.*

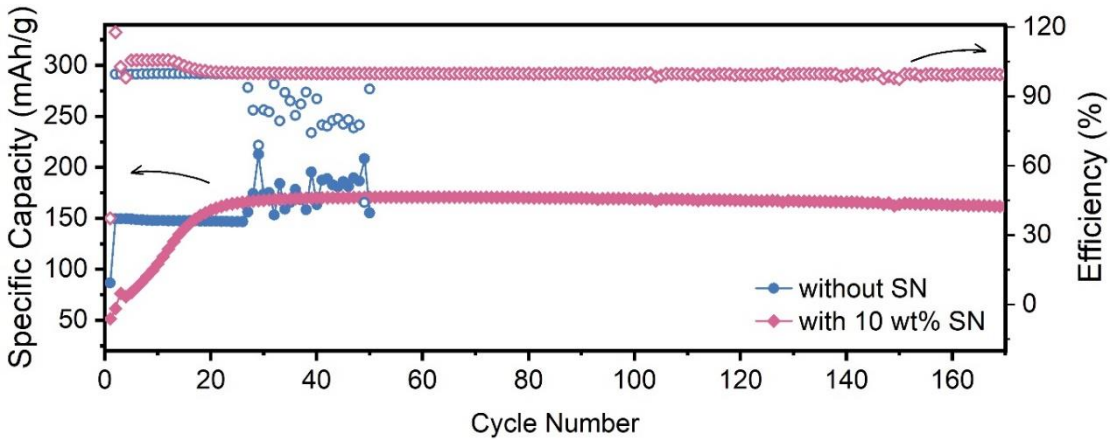

Figure 6.11. *Capacity retention and efficiency of the Li/PEO-10SN/LiFePO$_4$ cell (pink) and Li/PEO-0SN/LiFePO$_4$ cell (blue). Reproduced with permission from [20]. Copyright 2025 by the authors. Advanced Science published by Wiley-VCH GmbH.*

The stability of PEO-10SN with lithium metal was confirmed, and all-solid-state LiFePO$_4$ batteries were subsequently assembled to assess the oxidative stability of two samples, as shown in Figure 6.11. The fitst three cycles were performed at 0.05 C and the following cycles were performed at 0.1 C. In the Li/PEO-10SN/LiFePO$_4$ cell, the initial 25 cycles can be considered as the activeation process. The Li/PEO-10SN/LiFePO$_4$ cell achieved an impressive discharge specific capacity of 169.15 mAh g^{-1} after 25 cycles at 0.1C, with a coulombic efficiency consistently exceeding 99.5 %. Notably, the cell maintained a high capacity retention of 95.6 % even after 170 cycles. These results demonstrate that the SN-modified electrolyte is highly compatible with both lithium metal and LiFePO$_4$ electrodes. In contrast, the Li/PEO-0SN/LiFePO$_4$ cell does not exhibit an activation process. It delivers a discharge capacity of 149.56 mAh

g^{-1} initially, which decreases to 146 mAh g^{-1} by the 26th cycle. Subsequently, the cell fails during continuous cycling.

6.4 Observation of lithium dendrite growth

Lithium dendrites are the most significant hurdles for lithium batteries, especially for those with a metallic lithium anode. While ex-situ techniques such as SEM or X-ray tomography can confirm the presence of dendrites after several cycles, capturing the real-time initiation and growth of dendrites during cell operation remains a difficult task. Nondestructive synchrotron radiation-based operando nWAXS with high photon flux and high temporal resolution [127], stands out from other techniques and enables monitoring the lithium dendrite growth process in real time. Detailed information about the setup and experiments are explained in Section 3.1.4.

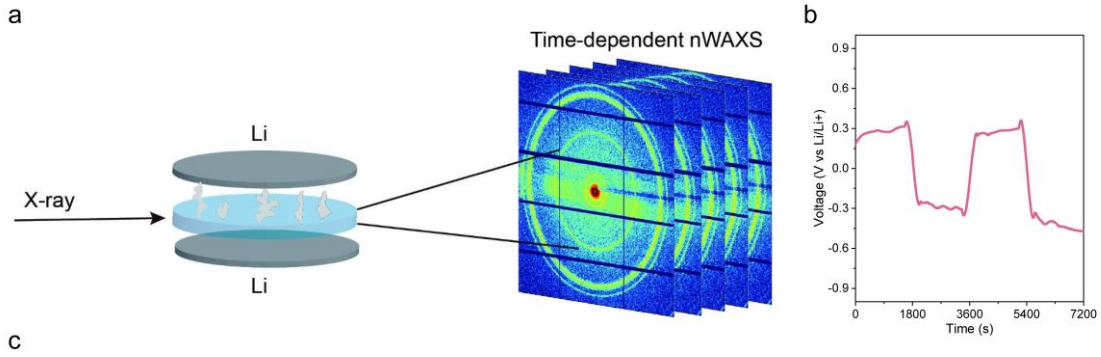

Figure 6.12. *(a) Schematic illustration of operando nWAXS measurement. (b) Time-voltage cycling profile of Li/PEO-10SN/Li cells during operando nWAXS measurement. Reproduced with permission from [20]. Copyright 2025 by the authors. Advanced Science published by Wiley-VCH GmbH.*

The illustration of operando nWAXS measurement is given in Figure 6.12a. Figure 6.12b and Figure 6.13 exhibits the charging/discharging curves of Li/PEO-10SN/Li and Li/PEO-0SN/Li cells, respectively. The reference sample exhibits a large overpotential on the initial half cycle, while the symmetric cell with 10 wt% SN additive demonstrates a smooth cycling profile with a lower overpotential.

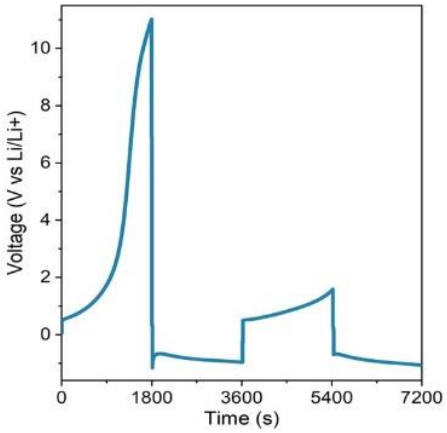

Figure 6.13. *Time-Voltage cycling profile of Li/PEO-0SN/Li cells during operando nWAXS measurement. Reproduced with permission from [20]. Copyright 2025 by the authors. Advanced Science published by Wiley-VCH GmbH.*

Figures 6.14 and Figure 6.15 show the 1D radius cuts acquired from the 2D nWAXS data of Li/PEO-10SN/Li cell, and Li/PEO-0SN/Li cell, respectively, and the standard PDF data of Li, LiF, and Li_3N. The drop lines represent the standard PDF profile of Li (black), LiF (red), and Li_3N (green).

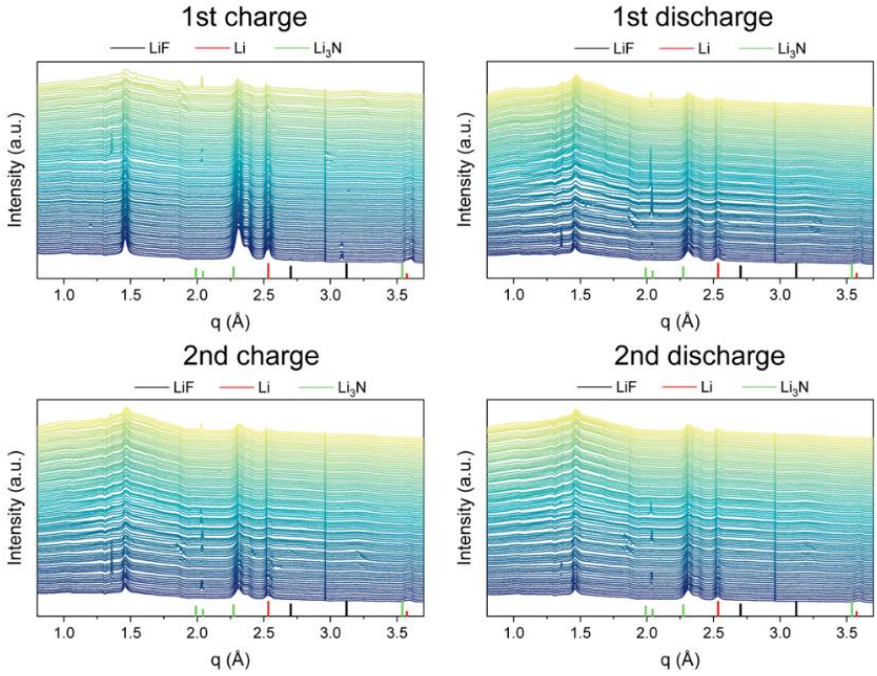

Figure 6.14. *Accumulated radius cuts of 2D nWAXS data at Li/PEO-10SN interface during two charging/discharging cycles. Reproduced with permission from [20]. Copyright 2025 by the authors. Advanced Science published by Wiley-VCH GmbH.*

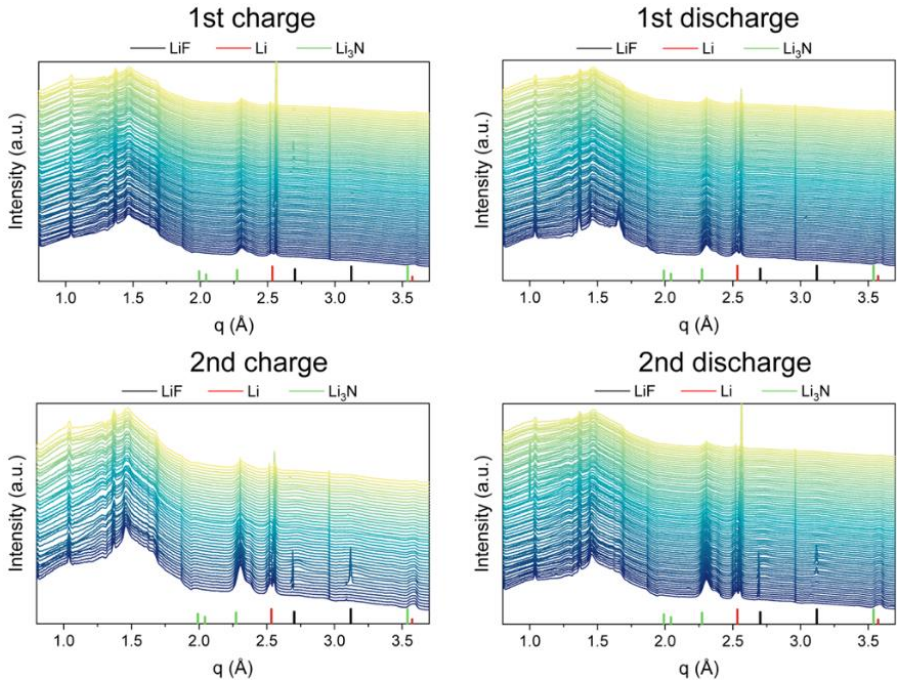

Figure 6.15. *Accumulated radius cuts of 2D nWAXS data at Li/PEO-0SN interface during two charging/discharging cycles. Reproduced with permission from [20]. Copyright 2025 by the authors. Advanced Science published by Wiley-VCH GmbH.*

Figure 6.16a-b show the q maps for the prominent Li (110) peak over two charge/discharge cycles of Li/PEO-10SN/Li and Li/PEO-0SN/Li cells, respectively, revealing the lithium dendrites formation process. In the Li/PEO-10SN cell, no visible mossy Li growth is observed along the (110) direction after repeated Li plating and stripping, indicating that dendrites do not form at the Li/PEO-10SN interface. Moreover, the depletion of Li (200) at the Li/PEO-10SN electrolyte interface is clearly visible (Figure 6.17), indicating that original metallic lithium actively participates in the stripping and plating process from the (200) plane without regrowth. This stable interface in lithium metal batteries guarantees cycling stability, mitigating dendrite growth and promoting uniform lithium deposition. In contrast, in the reference sample (Li/PEO-0SN/Li cell), large metallic nano Li crystals grow from the metallic lithium side, then distribute along the vertical direction (q_y from 2 to 7.5 μm) with respect to the X-ray beam, and finally reach the electrolyte phase during the first half-cycle, correlating with the large overpotential seen on Figure 6.13. This leads to the micro-short circuit within the cells. In the following cycles, the Li (110) remains visible, especially during the second charge and discharge cycles, indicating a continuous growth of the nano lithium crystals at the interface, which ultimately results in cell failure. Unlike the Li/PEO-10SN/Li cells, where the Li from (200) plane participants in

the plating/stripping process, the Li (200) peak from Li/PEO-0SN interface (Figure 6.18) continuously accumulates during cycling, increasing the thickness of the Li layer. This accumulation, in turn, creates an uneven and irregular contact interface, further destabilizing the cell and contributing to its failure.

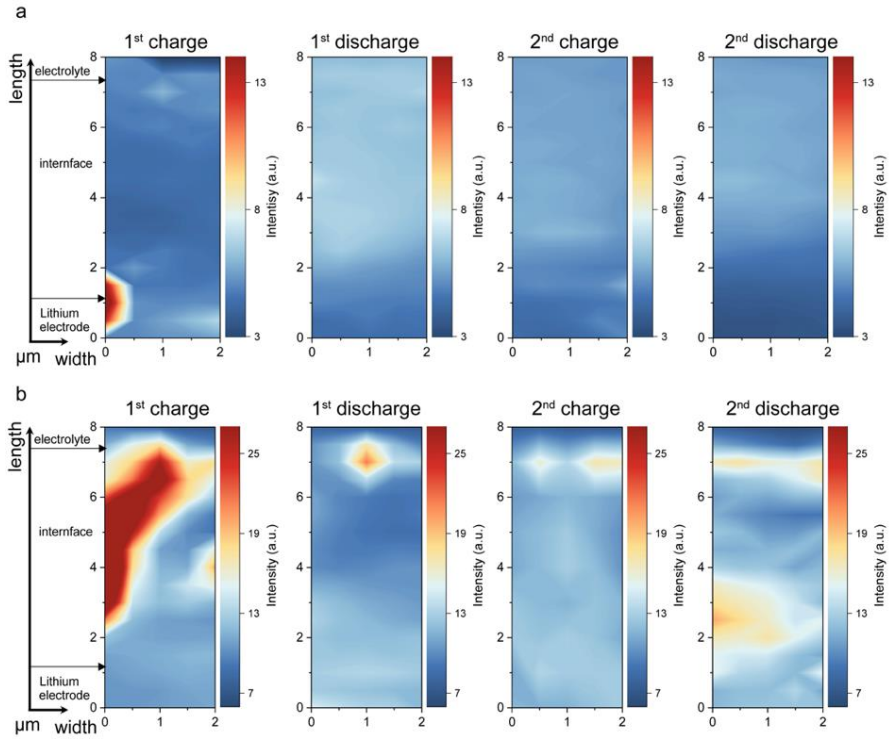

Figure 6.16. *2D q maps of Li (110) peak in the scanned area around the Li/electrolyte interface during two charging/discharging cycles of (a) Li/PEO-10SN electrolyte interface and (b) Li/PEO-0SN electrolyte interface. Reproduced with permission from [20]. Copyright 2025 by the authors. Advanced Science published by Wiley-VCH GmbH.*

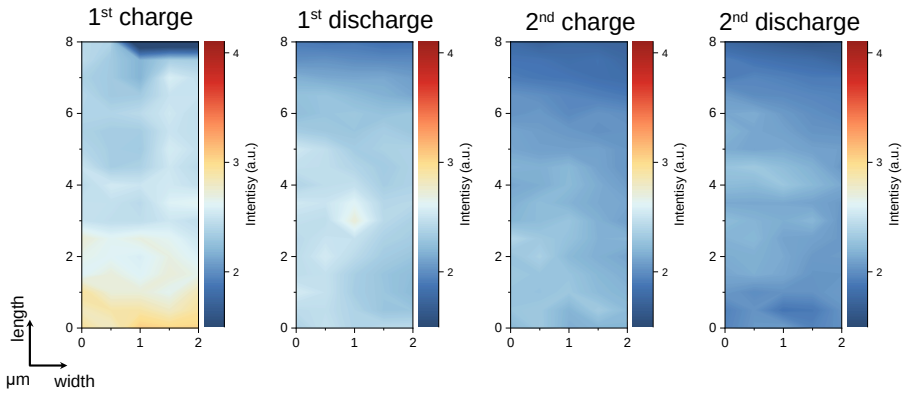

Figure 6.17. *2D q maps of Li (200) peak in the scanned area around the Li/PEO-10SN electrolyte interface during two charging/discharging cycles. Reproduced with permission from [20]. Copyright 2025 by the authors. Advanced Science published by Wiley-VCH GmbH.*

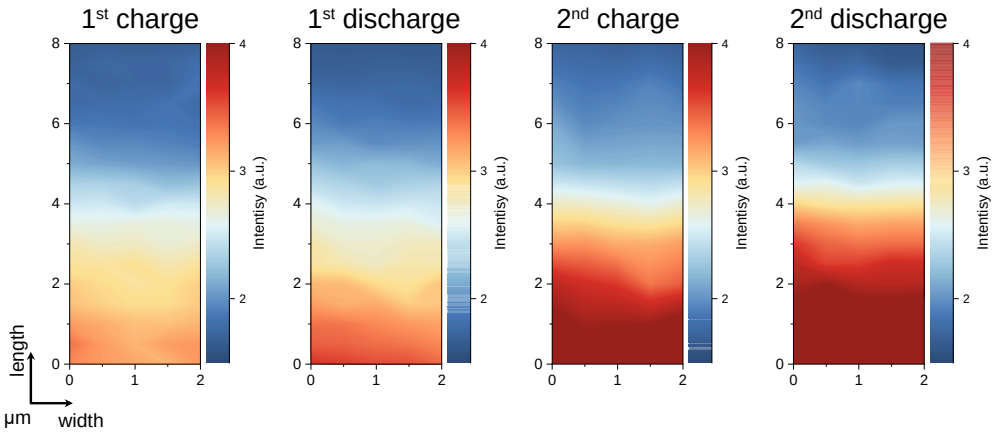

Figure 6.18. *2D q maps of Li (200) peak in the scanned area around the Li/PEO-0SN electrolyte interface during two charging/discharging cycles. Reproduced with permission from [20]. Copyright 2025 by the authors. Advanced Science published by Wiley-VCH GmbH.*

6.5 Observation of SEI formation

A stable and uniform SEI, including components such as LiF, Li_3N, and Li_2S, is essential for suppressing lithium dendrite growth, blocking electron transport, and facilitating efficient Li^+ plating and stripping. However, similar to lithium dendrites, tracking and analyzing the SEI formation process in all-solid-state lithium batteries remains challenging. By using operando nWAXS, we are able to track the formation kinetics of key SEI components, specifically LiF and Li_3N in real-time.

The LiF growth on (200) and (111) planes at Li/PEO-0SN interface is mapped out in Figure 6.19a and Figure 6.20. Interestingly, no signal is detected for the (200) plane, and only a weak (111) plane signal, originating from the metallic lithium side, is observed. The LiF (111) peak might result from the reaction between the decomposition product of $TFSI^-$ and Li metal, rather than with plating Li^+. Furthermore, the q map of (111) plane presents an unclear and irregular edge (Figure 6.20), which dissolves during the second half-cycle (stripping process), indicating the formation of a weak and soft SEI layer. In contrast, at the Li/PEO-10SN interface, distinct (200) and (111) plane signals are observed (Figure 6.19b and Figure 6.21, respectively). At the Li/PEO-10SN interface, LiF growth initials from the electrolyte side at around a middle-time of the Li^+ plating process, then extends across the interface, reaching the original metallic lithium by the end of the Li^+ stripping process. This LiF formation leads to the

development of a rigid and stable SEI layer, providing an enhanced interfacial stability and suppressing dendrite formation. The formation of Li_3N exhibits a similar trend. At the Li/PEO-0SN interface (Figure 6.19c), the signal from Li_3N (100) plane is barely detectable. However, at the Li/PEO-10SN interface, the Li_3N (100) plane signal is clearly pronounced, as shown in Figure 6.19d. During the Li^+ plating process (1st half-cycle), Li_3N starts forming on the PEO-10SN electrolyte side and continues to grow toward the metallic lithium electrode. This growth persists throughout the cycle, extending until the Li^+ stripping process is complete.

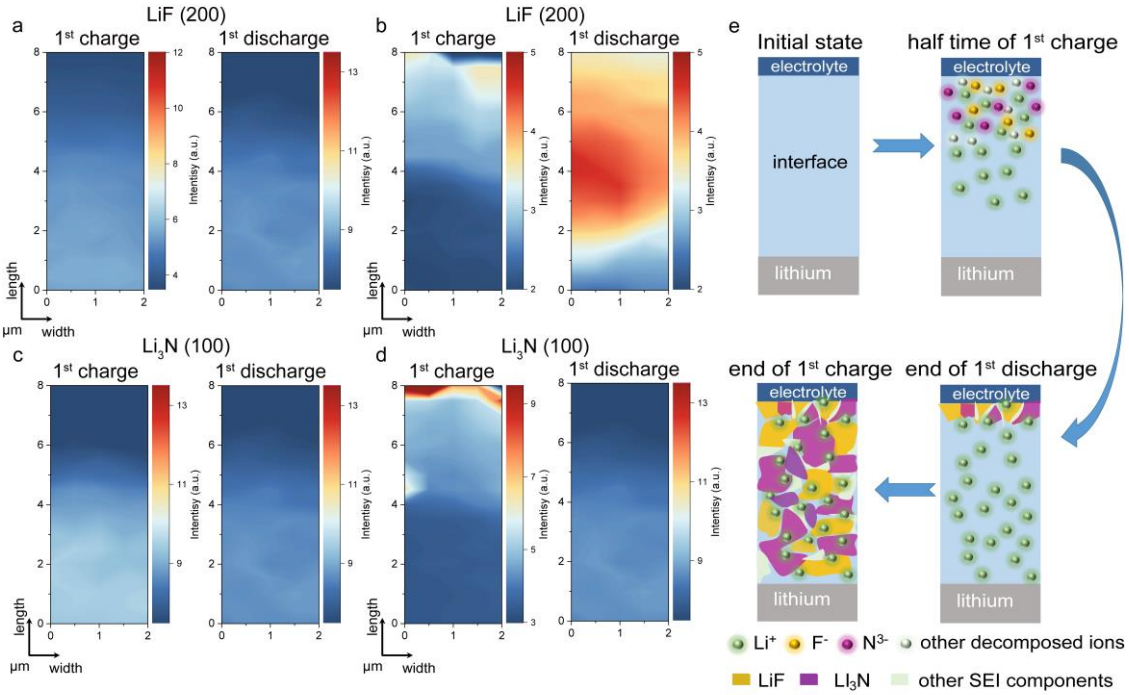

Figure 6.19. *Real-time observation of SEI formation on Li/PEO-xSN/Li cells (x = 0 and 10) during the first cycle by operando nWAXS. Temporal contour 2D maps of LiF (200) peaks in the scanned area around the Li/electrolyte interface during the first cycle of (a) Li/PEO-0SN electrolyte interface and (b) Li/PEO-10SN electrolyte interface. Temporal contour 2D maps of Li3N (100) peaks in the scanned area around the Li/electrolyte interface during two charging/discharging cycles of (c) Li/PEO-0SN electrolyte interface and (d) Li/PEO-10SN electrolyte interface. These 2D maps illustrate the growth mechanism of the SEI layer on the Li/electrode interface. (e) Schematic illustration of SEI formation mechanism in Li/PEO-10SN/Li cell. Reproduced with permission from [20]. Copyright 2025 by the authors. Advanced Science published by Wiley-VCH GmbH.*

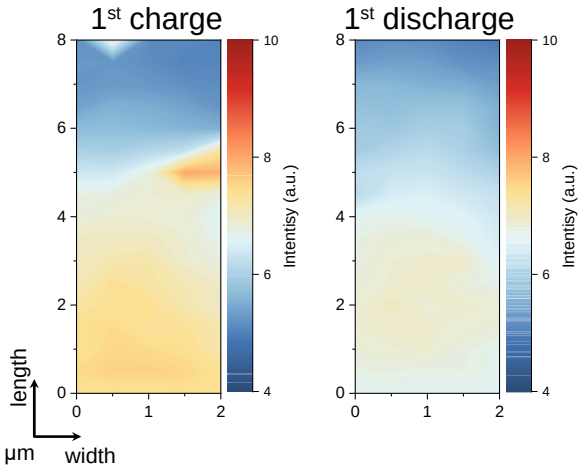

Figure 6.20. *2D q maps of LiF (111) peak in the scanned area around the Li/ PEO-0SN interface during the first charging/discharging cycle. Reproduced with permission from [20]. Copyright 2025 by the authors. Advanced Science published by Wiley-VCH GmbH.*

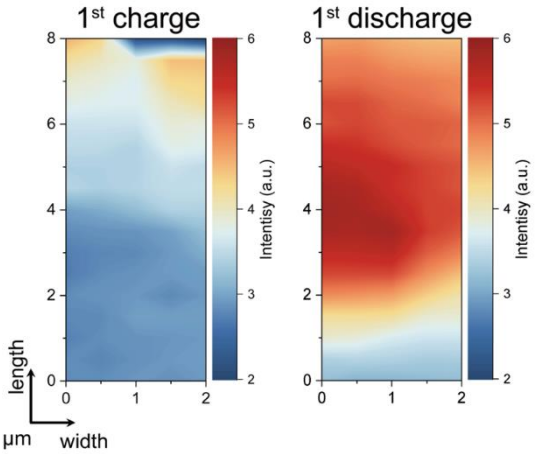

Figure 6.21. *2D q maps of LiF (111) peak in the scanned area around the Li/ PEO-10SN interface during the first charging/discharging cycle. Reproduced with permission from [20]. Copyright 2025 by the authors. Advanced Science published by Wiley-VCH GmbH.*

The formation of LiF and Li_3N at Li/PEO-10SN interface in the 1st charging/discharging process suggests the formation of a stable and continuous SEI layer, which is contributing to the high-performance all-solid-state lithium batteries. To wrap up, the SEI formation mechanism is illustrated in Figure 6.17e. To better illustrate the SEI formation mechanism, the interface area is exaggerated. The primary components, LiF and Li_3N, nucleate from the electrolyte side at the half-time of the Li^+

plating process as the result of electrochemical reactions between $TFSI^-$ decomposition products and Li^+. This SEI layer should then gradually extend toward the lithium electrode, continuing its growth until the completion of 1st charge/discharge process. The formation of a stable, ion-conductive SEI layer is crucial for maintaining the cycling performance and extending the lifespan of lithium batteries.

6.6 Summary

In summary, we fabricate a succinonitrile-enhanced PEO composite electrolyte that effectively improves the conductivity and compatibility toward metallic lithium. We use *operando* nWAXS for real-time monitoring the lithium dendrites growth and SEI formation. The addition of SN reduces crystallinity and promotes the molecule intercalations, which enhanced the ion conductivity. The modified composite electrolyte demonstrates a superior stability against metallic lithium, leading to a low overpotential and stable cycling in all-solid-state LMB. *Operando* nWAXS analysis shows that the modified symmetric cells effectively suppress dendrite growth, with no nano lithium crystal detected. In contrast, the reference symmetric cells reveal that the lithium dendrites initially grow in the early stage of the Li^+ plating process, originating from the lithium metal side and penetrating across the Li/electrolyte interface into the electrolyte. Despite the slight dissolution of nano lithium crystals, these dendrite crystals still exist and remain harmful to the cell performance. Additionally, the SEI formation mechanism is revealed by nWAXS. The main SEI components, LiF and Li_3N, begin to form from the electrolyte side around halfway through the first charging cycle and continuously extend to the lithium metal side at the end of the first discharging cycle. This process creates a uniform and stable Li/electrolyte interface layer that effectively suppresses the lithium dendrite growth, promoting Li^+ diffusion and uniform Li^+ plating/stripping. Thus, our findings validate that the use of simple additives such as SN is an effective strategy for enhancing interface stability and improving electrochemical performance in all-solid-state LMBs. Furthermore, the insights gained from *operando* nWAXS measurements will facilitate a deeper understanding of dendrite growth and SEI formation across various battery types, allowing for optimization of interface behavior and electrochemical properties in future research.

7 Conclusion and outlook

Solid electrolytes are designed for use in energy storage devices, particularly in lithium-ion and lithium metal batteries, where they replace traditional liquid electrolytes. Solid composite electrolytes are considered promising candidates for the next generation of batteries, especially for all-solid-state batteries (ASSBs), due to their numerous advantages, such as enhanced safety, higher energy densities, and longer lifespans. Unlike liquid electrolytes, solid electrolytes do not contain organic solvents, making them non-flammable and less prone to leakage, which significantly improves safety, particularly in high-energy applications like lithium metal batteries. Additionally, solid electrolytes can withstand higher operating temperatures and generally offer better chemical stability compared to liquid electrolytes. However, despite advancements in ionic conductivity, solid electrolytes still lag behind liquid electrolytes in terms of ion conduction, particularly at lower temperatures. Furthermore, issues at the interface between the solid electrolyte and electrodes, especially with lithium metal, can lead to problems like dendrite growth or poor adhesion, potentially causing battery failure.

A widely used approach to address this challenge is the development of solid composite electrolytes (SCEs) that combine a polymer and lithium salt matrix, inorganic fillers, and other additives. SCEs leverage the advantages of both polymer and ceramic materials, leading to enhanced thermal and chemical stability, reduced dendrite formation, and improved electrochemical performance. In this thesis, we focus on PEO-based composite electrolytes, where PEO and LiTFSI form the polymer matrix, and Al_2O_3 acts as an inorganic filler to enhance the mechanical stability of the electrolyte. PEO is cost-effective and easy to process, which simplifies the fabrication of composite electrolytes. The incorporation of inorganic fillers or plasticizers does not require complex methods, making PEO-based composites both cost-efficient and scalable for large-scale manufacturing. Additionally, PEO composite electrolytes are environmentally friendly, supporting the development of sustainable battery technologies and contributing to eco-conscious energy storage solutions.

To unlock the full potential of PEO composite electrolytes, it is imperative to gain a comprehensive understanding of their structural arrangement and internal morphology. Achieving this requires high-resolution analytical techniques capable of providing deep insights into these complex systems. Synchrotron-based X-ray scattering is a powerful tool for such investigations, offering unparalleled nanoscale resolution. Its high photon flux and precisely controlled illumination area make it an indispensable method for operando studies, enabling real-time analysis under working conditions. This advanced technique allows for the detailed examination of solid electrolyte structures, including their dimensions, spatial distribution, and crystalline properties. By employing synchrotron-based X-ray scattering during current or voltage sweeps, researchers can monitor the crystallization processes and morphological evolution of composite electrolytes with precision. Furthermore, the nanometer-scale X-ray beam enables direct observation of electrode/electrolyte interfacial behavior during operation, providing critical insights into interface stability and its impact on electrochemical performance.

The first study proposes PEO composite electrolyte with Al_2O_3 as inorganic filler, while Li||Cu cell was constructed to concurrently monitoring the electrochemical process with *operando* GISAXS/GIWAXS. With the assistance of GISAXS/GIWAXS, the intricate relationship between electrochemical processes and the buried morphology and crystalline structure of PEO composite electrolyte under working conditions. Our results reveal that two irreversible reactions — PEO-Li^+ reduction and $TFSI^-$ anion decomposition—induce pronounced changes in the crystalline structure, domain orientation, and overall morphology of the PEO composite electrolyte. These structural transformations compromise the electrolyte's long-term stability and performance. Additionally, the reversible lithium plating/stripping process was found to primarily affect the internal morphology, specifically altering the radius and spacing of PEO-LiTFSI domains. Interestingly, this process did not significantly impact the crystalline structure or domain orientation, highlighting a clear distinction between reversible and irreversible electrochemical mechanisms. By providing a comprehensive understanding of the structural and electrochemical evolution of PEO composite electrolyte, this work opens new pathways for designing advanced solid electrolytes. These insights are particularly valuable for improving the stability of lithium metal interfaces and addressing key challenges in all-solid-state battery development. Our findings emphasize the importance of coupling advanced characterization techniques with material innovation to achieve safer, more efficient, and commercially viable lithium metal batteries.

Further work introduces a succinonitrile (SN)-enhanced polyethylene oxide (PEO) composite electrolyte that significantly improves ionic conductivity and compatibility with metallic lithium. Leveraging *operando* nano-focus wide-angle X-ray scattering (nWAXS), we achieve real-time monitoring of lithium dendrite growth and solid electrolyte interphase (SEI) formation. The incorporation of SN reduces the crystallinity of PEO and promotes molecular intercalation, resulting in enhanced ion conductivity. This modified composite electrolyte demonstrates excellent stability against lithium metal, enabling low overpotential and stable cycling performance in all-solid-state lithium metal batteries (LMBs). Operando nWAXS reveals that the modified symmetric cells effectively suppress dendrite growth, with no evidence of nano-lithium crystals. In contrast, the reference symmetric cells show lithium dendrites forming early during the Li^+ plating process, originating from the lithium metal surface and penetrating into the electrolyte. Despite some dissolution, these harmful dendritic crystals persist, degrading cell performance. Additionally, nWAXS provides critical insights into SEI formation. Key SEI components, including LiF and Li_3N, begin forming on the electrolyte side midway through the first charge cycle, gradually extending toward the lithium metal surface by the end of the first discharge cycle. This process creates a uniform and stable Li/electrolyte interfacial layer that effectively mitigates dendrite growth, enhances Li^+ diffusion, and ensures uniform Li^+ plating and stripping. Our findings demonstrate that introducing simple additives like SN is a highly effective strategy for stabilizing interfaces and improving the electrochemical performance of all-solid-state LMBs. Furthermore, the operando nWAXS analysis offers valuable insights into dendrite dynamics and SEI evolution, providing a robust framework for optimizing interfacial behavior and electrochemical properties across various battery systems. This work lays the foundation for advancing the design and performance of next-generation energy storage technologies.

Overall, this thesis focuses on the fabrication and comprehensive characterization of performance-enhanced polyethylene oxide (PEO)-based composite electrolytes for lithium batteries. Advanced grazing-incidence scattering techniques (GISAXS and GIWAXS) were used to analyze the morphology of the PEO composite electrolyte and correlate these structural findings with their electrochemical behavior. Building on these insights, the performance of PEO electrolyte was further enhanced. nWAXS further confirmed the interfacial behavior within the lithium metal battery, as well as its failure mechanism. The results highlight the potential of these fabrication and analysis methods, demonstrating their application in advancing lithium battery technologies and contributing to the development of cutting-edge characterization techniques. While the

findings provide valuable structural insights, the studies were limited to specific material compositions and experimental conditions. Expanding the range of electrolyte materials and incorporating in situ cycling studies with real-world battery configurations would provide a more comprehensive understanding.

As battery technology continues to evolve, advanced characterization techniques will play a crucial role in unlocking the full potential of next-generation energy storage systems. Beyond PEO systems, this research paves the way for exploring other solid-state electrolytes, such as polycarbonate-based, NASICONs, garnet-type electrolytes and so on. The advanced scattering techniques employed in this study, can be extended to analyze the structural evolution and ion transport mechanisms in these alternative electrolytes under different electrochemical conditions. By performing operando measurements under applied current or voltage sweeps, researchers can gain deeper insights into phase stability, ion migration pathways, and potential degradation mechanisms that affect battery performance and longevity. The advanced scattering techniques used here can also be applied to study the behavior of these electrolytes under current or voltage sweeps. Furthermore, utilizing a variety of battery configurations, such as lithium symmetric cells, Li||LFP cells, Li||NMC811 cells, and Li||Cu cells, enables a comprehensive investigation of the interfacial interactions between solid electrolytes and both anode and cathode materials. These studies are critical for understanding interfacial stability, lithium dendrite formation, and potential side reactions, which are key challenges in solid-state battery development. The findings from such investigations will help in optimizing electrolyte formulations, improving electrode-electrolyte compatibility, and ultimately enabling the design of high-performance, durable, and safer solid-state lithium batteries for future energy storage applications.

Bibliography

[1] Tarascon, J.-M.; Armand, M., Issues and challenges facing rechargeable lithium batteries. *Nature* **2001,** *414* (6861), 359-367.

[2] Evarts, E. C., Lithium batteries: To the limits of lithium. *Nature* **2015,** *526* (7575), 93-95.

[3] Kim, S.; Park, G.; Lee, S. J.; Seo, S.; Ryu, K.; Kim, C. H.; Choi, J. W., Lithium-metal batteries: from fundamental research to industrialization. *Advanced Materials* **2023,** *35* (43), 2206625.

[4] Liu, J.; Bao, Z.; Cui, Y.; Dufek, E. J.; Goodenough, J. B.; Khalifah, P.; Li, Q.; Liaw, B. Y.; Liu, P.; Manthiram, A., Pathways for practical high-energy long-cycling lithium metal batteries. *Nature Energy* **2019,** *4* (3), 180-186.

[5] Xiao, J.; Li, Q.; Bi, Y.; Cai, M.; Dunn, B.; Glossmann, T.; Liu, J.; Osaka, T.; Sugiura, R.; Wu, B.; Yang, J.; Zhang, J.-G.; Whittingham, M. S., Understanding and applying coulombic efficiency in lithium metal batteries. *Nature Energy* **2020,** *5* (8), 561-568.

[6] Zhang, X.; Yang, Y.; Zhou, Z., Towards practical lithium-metal anodes. *Chemical Society Reviews* **2020,** *49* (10), 3040-3071.

[7] Xu, W.; Wang, J.; Ding, F.; Chen, X.; Nasybulin, E.; Zhang, Y.; Zhang, J.-G., Lithium metal anodes for rechargeable batteries. *Energy & Environmental Science* **2014,** *7* (2), 513-537.

[8] Goodenough, J. B.; Kim, Y., Challenges for rechargeable Li batteries. *Chemistry of Materials* **2010,** *22* (3), 587-603.

[9] Kim, H.; Jeong, G.; Kim, Y.-U.; Kim, J.-H.; Park, C.-M.; Sohn, H.-J., Metallic anodes for next generation secondary batteries. *Chemical Society Reviews* **2013,** *42* (23), 9011-9034.

[10] Varzi, A.; Thanner, K.; Scipioni, R.; Di Lecce, D.; Hassoun, J.; Dörfler, S.; Altheus, H.; Kaskel, S.; Prehal, C.; Freunberger, S. A., Current status and future perspectives of lithium metal batteries. *Journal of Power Sources* **2020,** *480*, 228803.

[11] Liu, B.; Zhang, J.-G.; Xu, W., Advancing lithium metal batteries. *Joule* **2018,** *2* (5), 833-845.

[12] Lopez, J.; Mackanic, D. G.; Cui, Y.; Bao, Z., Designing polymers for advanced battery chemistries. *Nature Reviews Materials* **2019,** *4* (5), 312-330.

[13] Saal, A.; Hagemann, T.; Schubert, U. S., Polymers for battery applications — active materials, membranes, and binders. *Advanced Energy Materials* **2021,** *11* (43), 2001984.

[14] Haruyama, J.; Sodeyama, K.; Han, L.; Takada, K.; Tateyama, Y., Space–charge layer effect at interface between oxide cathode and sulfide electrolyte in all-solid-state lithium-ion battery. *Chemistry of Materials* **2014,** *26* (14), 4248-4255.

[15] Schnell, J.; Günther, T.; Knoche, T.; Vieider, C.; Köhler, L.; Just, A.; Keller, M.; Passerini, S.; Reinhart, G., All-solid-state lithium-ion and lithium metal batteries–paving the way to large-scale production. *Journal of Power Sources* **2018,** *382*, 160-175.

[16] Eshetu, G. G.; Grugeon, S.; Laruelle, S.; Boyanov, S.; Lecocq, A.; Bertrand, J.-P.; Marlair, G., In-depth safety-focused analysis of solvents used in electrolytes for large scale lithium ion batteries. *Physical Chemistry Chemical Physics* **2013,** *15* (23), 9145-9155.

[17] Xia, S.; Wu, X.; Zhang, Z.; Cui, Y.; Liu, W., Practical challenges and future perspectives of all-solid-state lithium-metal batteries. *Chem* **2019,** *5* (4), 753-785.

[18] Wang, J.; Ge, B.; Li, H.; Yang, M.; Wang, J.; Liu, D.; Fernandez, C.; Chen, X.; Peng, Q., Challenges and progresses of lithium-metal batteries. *Chemical Engineering Journal* **2021,** *420*, 129739.

[19] Liang, Y.; Zheng, T.; Sun, K.; Xu, Z.; Guan, T.; Apfelbeck, F. A. C.; Ding, P.; Sharp, I. D.; Cheng, Y.; Schwartzkopf, M.; Roth, S. V.; Müller-Buschbaum, P., Operando study insights into lithiation/delithiation processes in a poly(ethylene oxide) electrolyte of all-solid-state lithium batteries by grazing-incidence x-ray scattering. *ACS Applied Materials & Interfaces* **2024,** *16* (26), 33307-33315.

[20] Liang, Y.; Apfelbeck, F. A.; Sun,K.; Yan, Y.; Cheng,L.; Pan,G.; Zheng,T.; Cheng, Y.; Davydok, A.; Krywka, C.; Müller-Buschbaum, P., Unveiling the li/electrolyte interface behavior for dendrite-free all-solid-state lithium metal batteries by operando nano-focus WAXS. *Advanced Science* **2025,** *2414714*.

[21] Chen, T.; Jin, Y.; Lv, H.; Yang, A.; Liu, M.; Chen, B.; Xie, Y.; Chen, Q., Applications of lithium-ion batteries in grid-scale energy storage systems. *Transactions of Tianjin University* **2020,** *26* (3), 208-217.

[22] Kim, T.; Song, W.; Son, D.-Y.; Ono, L. K.; Qi, Y., Lithium-ion batteries: outlook on present, future, and hybridized technologies. *Journal of Materials Chemistry*

A **2019,** *7* (7), 2942-2964.

[23] Murashko, K. Thermal modelling of commercial lithium-ion batteries. **2016**.

[24] Goodenough, J. B.; Park, K.-S., The Li-ion rechargeable battery: a perspective. *Journal of the American Chemical Society* **2013,** *135* (4), 1167-1176.

[25] Deng, D., Li-ion batteries: basics, progress, and challenges. *Energy Science & Engineering* **2015,** *3* (5), 385-418.

[26] Nzereogu, P. U.; Omah, A. D.; Ezema, F. I.; Iwuoha, E. I.; Nwanya, A. C., Anode materials for lithium-ion batteries: A review. *Applied Surface Science Advances* **2022,** *9*, 100233.

[27] Bonino, F.; Brutti, S.; Reale, P.; Scrosati, B.; Gherghel, L.; Wu, J.; Müllen, K., A disordered carbon as a novel anode material in lithium-ion cells. *Advanced Materials* **2005,** *17*(6), 743-746.

[28] Lu, J.; Chen, Z.; Pan, F.; Cui, Y.; Amine, K., High-performance anode materials for rechargeable lithium-ion batteries. *Electrochemical Energy Reviews* **2018,** *1* (1), 35-53.

[29] Chan, C. K.; Peng, H.; Liu, G.; McIlwrath, K.; Zhang, X. F.; Huggins, R. A.; Cui, Y., High-performance lithium battery anodes using silicon nanowires. *Nature Nanotechnology* **2008,** *3* (1), 31-35.

[30] Ruffo, R.; Hong, S. S.; Chan, C. K.; Huggins, R. A.; Cui, Y., Impedance analysis of silicon nanowire lithium ion battery anodes. *The Journal of Physical Chemistry C* **2009,** *113* (26), 11390-11398.

[31] Yuan, C.; Wu, H. B.; Xie, Y.; Lou, X. W., Mixed transition-metal oxides: Design, synthesis, and energy-related applications. *Angewandte Chemie International Edition* **2014,** *53* (6), 1488-1504.

[32] Wang, F.; Robert, R.; Chernova, N. A.; Pereira, N.; Omenya, F.; Badway, F.; Hua, X.; Ruotolo, M.; Zhang, R.; Wu, L., Conversion reaction mechanisms in lithium ion batteries: study of the binary metal fluoride electrodes. *Journal of the American Chemical Society* **2011,** *133* (46), 18828-18836.

[33] Yu, D. Y.; Hoster, H. E.; Batabyal, S. K., Bulk antimony sulfide with excellent cycle stability as next-generation anode for lithium-ion batteries. *Scientific Reports* **2014,** *4* (1), 4562.

[34] Lu, Y.; Yu, L.; Lou, X. W. D., Nanostructured conversion-type anode materials for advanced lithium-ion batteries. *Chem* **2018,** *4* (5), 972-996.

[35] Lin, D.; Liu, Y.; Cui, Y., Reviving the lithium metal anode for high-energy batteries. *Nature Nanotechnology* **2017,** *12* (3), 194-206.

[36] Bruce, P. G.; Freunberger, S. A.; Hardwick, L. J.; Tarascon, J.-M., Li–O_2 and Li–S batteries with high energy storage. *Nature materials* **2012,** *11* (1), 19-29.

[37] Nitta, N.; Wu, F.; Lee, J. T.; Yushin, G., Li-ion battery materials: present and future. *Materials Today* **2015,** *18* (5), 252-264.

[38] Kim, Y.; Kim, D.; Kang, S., Experimental and first-principles thermodynamic study of the formation and effects of vacancies in layered lithium nickel cobalt oxides. *Chemistry of Materials* **2011,** *23* (24), 5388-5397.

[39] Marianetti, C.; Van der Ven, A.; Ceder, G., Jahn-Teller mediated ordering in layered Li_xMO_2 compounds. *Physical Review B* **2001,** *63* (14), 144107.

[40] Sharma, S. K.; Sharma, G.; Gaur, A.; Arya, A.; Mirsafi, F. S.; Abolhassani, R.; Rubahn, H.-G.; Yu, J.-S.; Mishra, Y. K., Progress in electrode and electrolyte materials: path to all-solid-state Li-ion batteries. *Energy Advances* **2022,** *1* (8), 457-510.

[41] Laubach, S.; Laubach, S.; Schmidt, P. C.; Ensling, D.; Schmid, S.; Jaegermann, W.; Thißen, A.; Nikolowski, K.; Ehrenberg, H., Changes in the crystal and electronic structure of $LiCoO_2$ and $LiNiO_2$ upon Li intercalation and de-intercalation. *Physical Chemistry Chemical Physics* **2009,** *11* (17), 3278-3289.

[42] Wang, J. M.; Hu, J. P.; Ouyang, C. Y.; Shi, S. Q.; Lei, M. S., Cobalt suppressed Jahn-Teller effect in $LiCo_{0.5}Ni_{0.5}O_2$ for lithium ion batteries. *Solid State Communications* **2011,** *151* (3), 234-237.

[43] Myung, S.-T.; Ogata, A.; Lee, K.-S.; Komaba, S.; Sun, Y.-K.; Yashiro, H., structural, electrochemical, and thermal aspects of $Li[(Ni_{0.5}Mn_{0.5})_{1-x}Co_x]O_2$ ($0 \leqslant x \leqslant 0.2$) for high-voltage application of lithium-ion secondary batteries. *Journal of the Electrochemical Society* **2008,** *155* (5), 374.

[44] Martha, S.; Markevich, E.; Burgel, V.; Salitra, G.; Zinigrad, E.; Markovsky, B.; Sclar, H.; Pramovich, Z.; Heik, O.; Aurbach, D., A short review on surface chemical aspects of Li batteries: A key for a good performance. *Journal of Power Sources* **2009,** *189* (1), 288-296.

[45] Li, D.; Yuan, C.; Dong, J.; Peng, Z.; Zhou, Y., Synthesis and electrochemical properties of $LiNi_{0.85-x}Co_xMn_{0.15}O_2$ as cathode materials for lithium-ion batteries. *Journal of Solid State Electrochemistry* **2008,** *12*, 323-327.

[46] Kim, J.-M.; Kumagai, N.; Cho, T.-H., Synthesis, structure, and electrochemical characteristics of overlithiated $Li_{1+x}(Ni_zCo_{1-2z}Mn_z)_{1-x}O_2$ ($z= 0.1–0.4$ and $x= 0.0–0.1$) positive electrodes prepared by spray-drying method. *Journal of the Electrochemical Society* **2007,** *155* (1), 82.

[47] Fergus, J. W., Recent developments in cathode materials for lithium ion batteries.

Journal of Power Sources **2010,** *195* (4), 939-954.

[48] Hosono, E.; Kudo, T.; Honma, I.; Matsuda, H.; Zhou, H., synthesis of single crystalline spinel $LiMn_2O_4$ nanowires for a lithium ion battery with high power density. *Nano Letters* **2009,** *9* (3), 1045-1051.

[49] Xia, Y.; Zhou, Y.; Yoshio, M., Capacity fading on cycling of 4 V Li/$LiMn_2O_4$ cells. *Journal of The Electrochemical Society* **1997,** *144* (8), 2593.

[50] Ohzuku, T.; Takeda, S.; Iwanaga, M., Solid-state redox potentials for $Li[Me_{1/2}Mn_{3/2}]O_4$ (Me: 3d-transition metal) having spinel-framework structures: A series of 5 volt materials for advanced lithium-ion batteries. *Journal of Power Sources* **1999,** *81-82*, 90-94.

[51] Zhang, T.; Li, D.; Tao, Z.; Chen, J., Understanding electrode materials of rechargeable lithium batteries via DFT calculations. *Progress in Natural Science: Materials International* **2013,** *23* (3), 256-272.

[52] Yuan, L. X.; Wang, Z. H.; Zhang, W. X.; Hu, X. L.; Chen, J. T.; Huang, Y. H.; Goodenough, J. B., Development and challenges of $LiFePO_4$ cathode material for lithium-ion batteries. *Energy and Environmental Science* **2011,** *4* (2), 269-284.

[53] Malik, R.; Burch, D.; Bazant, M.; Ceder, G., Particle size dependence of the ionic diffusivity. *Nano Letters* **2010,** *10* (10), 4123-4127.

[54] Morgan, D.; Van der Ven, A.; Ceder, G., Li Conductivity in Li_xMPO_4 (M = Mn, Fe, Co, Ni) olivine materials. *Electrochemical and Solid-State Letters* **2004,** *7* (2), A30.

[55] Nishimura, S.-i.; Kobayashi, G.; Ohoyama, K.; Kanno, R.; Yashima, M.; Yamada, A., Experimental visualization of lithium diffusion in $LixFePO_4$. *Nature Materials* **2008,** *7* (9), 707-711.

[56] [56]. Dathar, G. K. P.; Sheppard, D.; Stevenson, K. J.; Henkelman, G., Calculations of Li-ion diffusion in olivine phosphates. *Chemistry of Materials* **2011,** *23* (17), 4032-4037.

[57] Gover, R. K. B.; Burns, P.; Bryan, A.; Saidi, M. Y.; Swoyer, J. L.; Barker, J., $LiVPO_4F$: A new active material for safe lithium-ion batteries. *Solid State Ionics* **2006,** *177* (26-32 SPEC. ISS.), 2635-2638.

[58] Xu, B.; Qian, D.; Wang, Z.; Meng, Y. S., Recent progress in cathode materials research for advanced lithium ion batteries. *Materials Science and Engineering: R: Reports* **2012,** *73* (5), 51-65.

[59] Liu, Y.-K.; Zhao, C.-Z.; Du, J.; Zhang, X.-Q.; Chen, A.-B.; Zhang, Q., Research progresses of liquid electrolytes in lithium-ion batteries. *Small* **2023,** *19* (8), 2205315.

[60] Fan, X.; Wang, C., High-voltage liquid electrolytes for Li batteries: progress and perspectives. *Chemical Society Reviews* **2021,** *50* (18), 10486-10566.

[61] Wang, H.; Yu, Z.; Kong, X.; Kim, S. C.; Boyle, D. T.; Qin, J.; Bao, Z.; Cui, Y., Liquid electrolyte: The nexus of practical lithium metal batteries. *Joule* **2022,** *6* (3), 588-616.

[62] Xue, Z.; He, D.; Xie, X., Poly(ethylene oxide)-based electrolytes for lithium-ion batteries. *Journal of Materials Chemistry A* **2015,** *3* (38), 19218-19253.

[63] Shaplov, A. S.; Marcilla, R.; Mecerreyes, D., Recent advances in innovative polymer electrolytes based on poly (ionic liquid) s. *Electrochimica Acta* **2015,** *175*, 18-34.

[64] Zhou, D.; Shanmukaraj, D.; Tkacheva, A.; Armand, M.; Wang, G., Polymer electrolytes for lithium-based batteries: advances and prospects. *Chem* **2019,** *5* (9), 2326-2352.

[65] Sun, C.; Liu, J.; Gong, Y.; Wilkinson, D. P.; Zhang, J., Recent advances in all-solid-state rechargeable lithium batteries. *Nano Energy* **2017,** *33*, 363-386.

[66] Gao, Z.; Sun, H.; Fu, L.; Ye, F.; Zhang, Y.; Luo, W.; Huang, Y., Promises, challenges, and recent progress of inorganic solid-state electrolytes for all-solid-state lithium batteries. *Advanced Materials* **2018,** *30* (17), 1705702.

[67] Liu, X.; Li, X.; Li, H.; Wu, H. B., Recent progress of hybrid solid-state electrolytes for lithium batteries. *Chemistry–A European Journal* **2018,** *24* (69), 18293-18306.

[68] Keller, M.; Varzi, A.; Passerini, S., Hybrid electrolytes for lithium metal batteries. *Journal of Power Sources* **2018,** *392*, 206-225.

[69] Cheng, X.-B.; Zhao, C.-Z.; Yao, Y.-X.; Liu, H.; Zhang, Q., Recent advances in energy chemistry between solid-state electrolyte and safe lithium-metal anodes. *Chem* **2019,** *5* (1), 74-96.

[70] Li, S.; Zhang, S.-Q.; Shen, L.; Liu, Q.; Ma, J.-B.; Lv, W.; He, Y.-B.; Yang, Q.-H., Progress and perspective of ceramic/polymer composite solid electrolytes for lithium batteries. *Advanced Science* **2020,** *7* (5), 1903088.

[71] Zou, Z.; Li, Y.; Lu, Z.; Wang, D.; Cui, Y.; Guo, B.; Li, Y.; Liang, X.; Feng, J.; Li, H., Mobile ions in composite solids. *Chemical Reviews* **2020,** *120* (9), 4169-4221.

[72] Xiao, W.; Wang, Z.; Zhang, Y.; Fang, R.; Yuan, Z.; Miao, C.; Yan, X.; Jiang, Y., Enhanced performance of P(VDF-HFP)-based composite polymer electrolytes doped with organic-inorganic hybrid particles PMMA-ZrO_2 for lithium ion batteries. *Journal of Power Sources* **2018,** *382*, 128-134.

[73] Zhang, M.; Li, M.; Chang, Z.; Wang, Y.; Gao, J.; Zhu, Y.; Wu, Y.; Huang, W., A sandwich PVDF/HEC/PVDF gel polymer electrolyte for lithium ion battery. *Electrochimica Acta* **2017,** *245*, 752-759.

[74] Ni'Mah, Y. L.; Cheng, M.-Y.; Cheng, J. H.; Rick, J.; Hwang, B.-J., Solid-state polymer nanocomposite electrolyte of TiO_2/PEO/$NaClO_4$ for sodium ion batteries. *Journal of Power Sources* **2015,** *278*, 375-381.

[75] Yu, X.; Manthiram, A., A review of composite polymer-ceramic electrolytes for lithium batteries. *Energy Storage Materials* **2021,** *34*, 282-300.

[76] Judez, X.; Zhang, H.; Li, C.; Eshetu, G. G.; Zhang, Y.; González-Marcos, J. A.; Armand, M.; Rodriguez-Martinez, L. M., Polymer-rich composite electrolytes for all-solid-state Li–S cells. *The Journal of Physical Chemistry Letters* **2017,** *8* (15), 3473-3477.

[77] Yu, X.; Manthiram, A., Electrode–electrolyte interfaces in lithium-based batteries. *Energy & Environmental Science* **2018,** *11* (3), 527-543.

[78] Li, J.; Zhong, L.; Li, J.-x.; Wu, H.-f.; Shao, W.-w.; Wang, P.-q.; Liu, M.-q.; Zhang, G.; Jing, M.-x., Insights into the effects of different inorganic fillers on the electrochemical performances of polymer solid electrolytes. *Colloids and Surfaces A: Physicochemical and Engineering Aspects* **2023,** *671*, 131704.

[79] Zhou, Q.; Ma, J.; Dong, S.; Li, X.; Cui, G., Intermolecular chemistry in solid polymer electrolytes for high-energy-density lithium batteries. *Advanced Materials* **2019,** *31* (50), 1902029.

[80] Xiao, Z.; Long, T.; Song, L.; Zheng, Y.; Wang, C., Research progress of polymer-inorganic filler solid composite electrolyte for lithium-ion batteries. *Ionics* **2022,** *28* (1), 15-26.

[81] Wang, Z.; Huang, X.; Chen, L., Understanding of effects of nano-Al_2O_3 particles on ionic conductivity of composite polymer electrolytes. *Electrochemical and Solid-state Letters* **2003,** *6* (11), E40.

[82] Croce, F.; Appetecchi, G.; Persi, L.; Scrosati, B., Nanocomposite polymer electrolytes for lithium batteries. *Nature* **1998,** *394* (6692), 456-458.

[83] Croce, F.; Curini, R.; Martinelli, A.; Persi, L.; Ronci, F.; Scrosati, B.; Caminiti, R., Physical and chemical properties of nanocomposite polymer electrolytes. *Journal of Physical Chemistry B* **1999,** *103* (48), 10632-10638.

[84] Lin, D.; Liu, W.; Liu, Y.; Lee, H. R.; Hsu, P.-C.; Liu, K.; Cui, Y., High ionic conductivity of composite solid polymer electrolyte via in situ synthesis of monodispersed SiO_2 nanospheres in poly(ethylene oxide). *Nano Letters* **2016,** *16* (1), 459-465.

[85] Ji, K. S.; Moon, H. S.; Kim, J. W.; Park, J. W., Role of functional nano-sized inorganic fillers in poly(ethylene)oxide-based polymer electrolytes. *Journal of Power Sources* **2003,** *117* (1-2), 124-130.

[86] Mariappan, C. R.; Yada, C.; Rosciano, F.; Roling, B., Correlation between micro-structural properties and ionic conductivity of $Li_{1.5}Al_{0.5}Ge_{1.5}(PO_4)_3$ ceramics. *Journal of Power Sources* **2011,** *196* (15), 6456-6464.

[87] Kitaura, H.; Zhou, H., Electrochemical performance of solid-state lithium-air batteries using carbon nanotube catalyst in the air electrode. *Advanced Energy Materials* **2012,** *2* (7), 889-894.

[88] Murugan, R.; Thangadurai, V.; Weppner, W., Fast lithium ion conduction in garnet-type $Li_7La_3Zr_2O_{12}$. *Angewandte Chemie International Edition* **2007,** *46* (41), 7778-7781.

[89] Quartarone, E.; Mustarelli, P., Electrolytes for solid-state lithium rechargeable batteries: recent advances and perspectives. *Chemical Society Reviews* **2011,** *40* (5), 2525-2540.

[90] Fan, L.; Wei, S.; Li, S.; Li, Q.; Lu, Y., Recent progress of the solid-state electrolytes for high-energy metal-based batteries. *Advanced Energy Materials* **2018,** *8* (11).

[91] Chen, R.; Qu, W.; Guo, X.; Li, L.; Wu, F., The pursuit of solid-state electrolytes for lithium batteries: from comprehensive insight to emerging horizons. *Materials Horizons* **2016,** *3* (6), 487-516.

[92] Fu, J.; Li, Z.; Zhou, X.; Guo, X., Ion transport in composite polymer electrolytes. *Materials Advances* **2022,** *3* (9), 3809-3819.

[93] Dirican, M.; Yan, C.; Zhu, P.; Zhang, X., Composite solid electrolytes for all-solid-state lithium batteries. *Materials Science and Engineering: R: Reports* **2019,** *136*, 27-46.

[94] Xu, L.; Li, J.; Shuai, H.; Luo, Z.; Wang, B.; Fang, S.; Zou, G.; Hou, H.; Peng, H.; Ji, X., Recent advances of composite electrolytes for solid-state Li batteries. *Journal of Energy Chemistry* **2022,** *67*, 524-548.

[95] Famprikis, T.; Canepa, P.; Dawson, J. A.; Islam, M. S.; Masquelier, C., Fundamentals of inorganic solid-state electrolytes for batteries. *Nature Materials* **2019,** *18* (12), 1278-1291.

[96] Liu, S.; Liu, W.; Ba, D.; Zhao, Y.; Ye, Y.; Li, Y.; Liu, J., Filler-integrated composite polymer electrolyte for solid-state lithium batteries. *Advanced Materials* **2023,** *35* (2), 2110423.

[97] Fan, P.; Liu, H.; Marosz, V.; Samuels, N. T.; Suib, S. L.; Sun, L.; Liao, L., High

performance composite polymer electrolytes for lithium-ion batteries. *Advanced Functional Materials* **2021,** *31* (23), 2101380.

[98] Cao, D.; Sun, X.; Li, Q.; Natan, A.; Xiang, P.; Zhu, H., Lithium dendrite in all-solid-state batteries: growth mechanisms, suppression strategies, and characterizations. *Matter* **2020,** *3* (1), 57-94.

[99] Yang, T.; Wang, C.; Zhang, W.; Xia, Y.; Huang, H.; Gan, Y.; He, X.; Xia, X.; Tao, X.; Zhang, J., A critical review on composite solid electrolytes for lithium batteries: Design strategies and interface engineering. *Journal of Energy Chemistry* **2023,** *84*, 189-209.

[100] Usiskin, R.; Maier, J., Interfacial effects in lithium and sodium batteries. *Advanced Energy Materials* **2021,** *11* (2), 2001455.

[101] Hobold, G. M.; Khurram, A.; Gallant, B. M., Operando gas monitoring of solid electrolyte interphase reactions on lithium. *Chemistry of Materials* **2020,** *32* (6), 2341-2352.

[102] Wu, H.; Jia, H.; Wang, C.; Zhang, J.-G.; Xu, W., Recent progress in understanding solid electrolyte interphase on lithium metal anodes. *Advanced Energy Materials* **2021,** *11* (5), 2003092.

[103] Qin, K.; Holguin, K.; Mohammadiroudbari, M.; Huang, J.; Kim, E. Y. S.; Hall, R.; Luo, C., Strategies in structure and electrolyte design for high-performance lithium metal batteries. *Advanced Functional Materials* **2021,** *31* (15), 2009694.

[104] Gadjourova, Z.; Andreev, Y. G.; Tunstall, D. P.; Bruce, P. G., Ionic conductivity in crystalline polymer electrolytes. *Nature* **2001,** *412* (6846), 520-3.

[105] Fullerton-Shirey, S. K.; Maranas, J. K., Effect of $LiClO_4$ on the structure and mobility of PEO-based solid polymer electrolytes. *Macromolecules* **2009,** *42* (6), 2142-2156.

[106] Zhao, F.; Qian, X.; Wang, E.; Dong, S., Advances in ionic conductive polymer electrolytes. *Progress in Chemistry* **2002,** *14* (05), 374.

[107] MacGlashan, G. S.; Andreev, Y. G.; Bruce, P. G., Structure of the polymer electrolyte poly(ethylene oxide)$_6$:$LiAsF_6$. *Nature* **1999,** *398* (6730), 792-794.

[108] Borodin, O.; Smith, G. D., LiTFSI structure and transport in ethylene carbonate from molecular dynamics simulations. *The Journal of Physical Chemistry B* **2006,** *110* (10), 4971-4977.

[109] Arya, A.; Sharma, A. L., A glimpse on all-solid-state Li-ion battery (ASSLIB) performance based on novel solid polymer electrolytes: a topical review. *Journal of Materials Science* **2020,** *55* (15), 6242-6304.

[110] Guo, B.; Fu, Y.; Wang, J.; Gong, Y.; Zhao, Y.; Yang, K.; Zhou, S.; Liu, L.; Yang,

S.; Liu, X.; Pan, F., Strategies and characterization methods for achieving high performance PEO-based solid-state lithium-ion batteries. *Chemical Communications* **2022,** *58* (59), 8182-8193.

[111] Su, X.; Xu, X.-P.; Ji, Z.-Q.; Wu, J.; Ma, F.; Fan, L.-Z., Polyethylene Oxide-based composite solid electrolytes for lithium batteries: current progress, low-temperature and high-voltage limitations, and prospects. *Electrochemical Energy Reviews* **2024,** *7* (1), 2.

[112] Feng, J.; Wang, L.; Chen, Y.; Wang, P.; Zhang, H.; He, X., PEO based polymer-ceramic hybrid solid electrolytes: a review. *Nano Convergence* **2021,** *8* (1), 2.

[113] Zhao, Y.; Wang, L.; Zhou, Y.; Liang, Z.; Tavajohi, N.; Li, B.; Li, T., Solid polymer electrolytes with high conductivity and transference number of li ions for Li-based rechargeable batteries. *Advanced Science* **2021,** *8* (7), 2003675.

[114] Wang, H.; Sheng, L.; Yasin, G.; Wang, L.; Xu, H.; He, X., Reviewing the current status and development of polymer electrolytes for solid-state lithium batteries. *Energy Storage Materials* **2020,** *33*, 188-215.

[115] Tolan, M., Reflectivity of x-rays from surfaces. In *X-Ray Scattering from Soft-Matter Thin Films: Materials Science and Basic Research*, Springer Berlin Heidelberg: Berlin, Heidelberg, **1999**, 5-31.

[116] Farinha, J.; Martinho, J., Resonance energy transfer in polymer interfaces. In *Fluorescence of Supermolecules, Polymers, and Nanosystems*, Springer: **2007**, 215-255.

[117] Lazzari, R., IsGISAXS: a program for grazing-incidence small-angle X-ray scattering analysis of supported islands. *Journal of Applied Crystallography* **2002,** *35* (4), 406-421.

[118] Müller-Buschbaum, P., A basic introduction to grazing incidence small-angle x-ray scattering. In *Applications of Synchrotron Light to Scattering and Diffraction in Materials and Life Sciences*, Eds. Springer Berlin Heidelberg: Berlin, Heidelberg, **2009**, 61-89.

[119] Gonzalo, S.; Shun, Y., Grazing incidence small angle x-ray scattering as a tool for in- situ time-resolved studies. In *X-ray Scattering*, Alicia Esther, A., Ed. IntechOpen: Rijeka, **2017**; p Ch. 2.

[120] Sinha, S.; Sirota, E.; Garoff; Stanley, H., X-ray and neutron scattering from rough surfaces. *Physical Review B* **1988,** *38* (4), 2297.

[121] Altamura, D.; Sibillano, T.; Siliqi, D.; Caro, L. D.; Giannini, C., Assembled nanostructured architectures studied by grazing incidence X-ray scattering. *Nanomaterials and Nanotechnology* **2012,** *2*, 16.

[122] Naudon, A.; Babonneau, D.; Thiaudiere, D.; Lequien, S., Grazing-incidence small-angle X-ray scattering applied to the characterization of aggregates in surface regions. *Physica B: Condensed Matter* **2000,** *283* (1-3), 69-74.

[123] Williams, C. E.; May, R. P.; Guinier, A., Small-angle scattering of X-rays and neutrons. *X-ray Characterization of Materials* **1999**, 211-254.

[124] Steele, J. A.; Solano, E.; Hardy, D.; Dayton, D.; Ladd, D.; White, K.; Chen, P.; Hou, J.; Huang, H.; Saha, R. A.; Wang, L.; Gao, F.; Hofkens, J.; Roeffaers, M. B. J.; Chernyshov, D.; Toney, M. F., How to GIWAXS: Grazing incidence wide angle x-ray scattering applied to metal halide perovskite thin films. *Advanced Energy Materials* **2023,** *13* (27), 2300760.

[125] Strobl, G., From the melt via mesomorphic and granular crystalline layers to lamellar crystallites: A major route followed in polymer crystallization? *The European Physical Journal E* **2000,** *3*, 165-183.

[126] Müller-Buschbaum, P., The active layer morphology of organic solar cells probed with grazing incidence scattering techniques. *Advanced Materials* **2014,** *26* (46), 7692-7709.

[127] Li, N.; Pratap, S.; Körstgens, V.; Vema, S.; Song, L.; Liang, S.; Davydok, A.; Krywka, C.; Müller-Buschbaum, P., Mapping structure heterogeneities and visualizing moisture degradation of perovskite films with nano-focus WAXS. *Nature Communications* **2022,** *13* (1), 6701.

[128] Vattuone, L.; Savio, L.; Rocca, M., Influence of defects on adsorption — model studies with stepped surfaces. In *Encyclopedia of Interfacial Chemistry*, Wandelt, K., Ed. Elsevier: Oxford, **2018**, 138-165.

[129] Zhou, W.; Apkarian, R.; Wang, Z. L.; Joy, D., Fundamentals of scanning electron microscopy (SEM). *Scanning Microscopy for Nanotechnology: Techniques and Applications* **2007**, 1-40.

[130] Benecke, G.; Wagermaier, W.; Li, C.; Schwartzkopf, M.; Flucke, G.; Hoerth, R.; Zizak, I.; Burghammer, M.; Metwalli, E.; Müller-Buschbaum, P.; Trebbin, M.; Förster, S.; Paris, O.; Roth, S. V.; Fratzl, P., A customizable software for fast reduction and analysis of large X-ray scattering data sets: applications of the new DPDAK package to small-angle X-ray scattering and grazing-incidence small-angle X-ray scattering. *Journal of Applied Crystallography* **2014,** *47* (Pt 5), 1797-1803.

[131] Müller-Buschbaum, P., Grazing incidence small-angle X-ray scattering: an advanced scattering technique for the investigation of nanostructured polymer films. *Analytical and Bioanalytical Chemistry* **2003,** *376*, 3-10.

[132] Reus, M. A.; Reb, L. K.; Kosbahn, D. P.; Roth, S. V.; Müller-Buschbaum, P.,

INSIGHT: in situ heuristic tool for the efficient reduction of grazing-incidence X-ray scattering data. *Journal of Applied Crystallography* **2024,** *57* (2), 509-528.

[133] Prime, R. B.; Bair, H. E.; Vyazovkin, S.; Gallagher, P. K.; Riga, A., Thermogravimetric Analysis (TGA). In *Thermal Analysis of Polymers*, **2009**, 241-317.

[134] Coats, A. W.; Redfern, J. P., Thermogravimetric analysis: A review. *Analyst* **1963,** *88* (1053), 906-924.

[135] Ortiz Ortega, E.; Hosseinian, H.; Aguilar Meza, I. B.; Rodríguez Vera, A.; Rosales López, M. J.; Hosseini, S., Characterization techniques for electrochemical analysis. In *Material Characterization Techniques and Applications*, Ortiz Ortega, E.; Hosseinian, H.; Aguilar Meza, I. B.; Rosales López, M. J.; Rodríguez Vera, A.; Hosseini, S., Eds. Springer Singapore: Singapore, **2022**, 195-220.

[136] Lazanas, A. C.; Prodromidis, M. I., Electrochemical impedance spectroscopy—A tutorial. *ACS Measurement Science Au* **2023,** *3* (3), 162-193.

[137] Abdullah, M.; Lenggoro, W.; Okuyama, K., Polymer electrolyte nanocomposites. In *Encyclopedia of Nanoscience and Nanotechnology*, American Scientific Publishers Stevenson Ranch, CA, USA: **2004**, 8, 731-762.

[138] Paul, S., Materials and electrochemistry: present and future battery. *Journal of Electrochemical Science Technology* **2016,** *7* (2), 115-131.

[139] Elgrishi, N.; Rountree, K. J.; McCarthy, B. D.; Rountree, E. S.; Eisenhart, T. T.; Dempsey, J. L., A practical beginner's guide to cyclic voltammetry. *Journal of Chemical Education* **2018,** *95* (2), 197-206.

[140] Lin, Q.; Dawson, G.; Diao, T., Experimental electrochemical potentials of nickel complexes. *Synlett* **2021,** *32* (16), 1606-1620.

[141] Bontempelli, G.; Dossi, N.; Toniolo, R., Linear sweep and cyclic☆. In *Reference Module in Chemistry, Molecular Sciences and Chemical Engineering*, Elsevier: 2016.

[142] Islam, M. N.; Channon, R. B., Chapter 1.3 - Electrochemical sensors. In *Bioengineering Innovative Solutions for Cancer*, Ladame, S.; Chang, J. Y. H., Eds. Academic Press: 2020; pp 47-71.

[143] Yang, X.; Rogach, A. L., Electrochemical techniques in battery research: A tutorial for nonelectrochemists. *Advanced Energy Materials* **2019,** *9* (25), 1900747.

[144] Goodenough, J. B.; Park, K. S., The Li-ion rechargeable battery: a perspective. *Journal of the American Chemical Society* **2013,** *135* (4), 1167-76.

[145] Wu, F.; Maier, J.; Yu, Y., Guidelines and trends for next-generation rechargeable lithium and lithium-ion batteries. *Chemical Society Reviews* **2020,** *49* (5), 1569-1614.

[146] Shen, X.; Liu, H.; Cheng, X.-B.; Yan, C.; Huang, J.-Q., Beyond lithium ion batteries: Higher energy density battery systems based on lithium metal anodes. *Energy Storage Materials* **2018,** *12*, 161-175.

[147] Placke, T.; Kloepsch, R.; Dühnen, S.; Winter, M., Lithium ion, lithium metal, and alternative rechargeable battery technologies: the odyssey for high energy density. *Journal of Solid State Electrochemistry* **2017,** *21* (7), 1939-1964.

[148] Li, M.; Lu, J.; Chen, Z.; Amine, K., 30 years of lithium-ion batteries. *Advanced Materials* **2018,** *30* (33), 1800561.

[149] Zheng, Y.; Yao, Y.; Ou, J.; Li, M.; Luo, D.; Dou, H.; Li, Z.; Amine, K.; Yu, A.; Chen, Z., A review of composite solid-state electrolytes for lithium batteries: fundamentals, key materials and advanced structures. *Chemical Society Reviews* **2020,** *49* (23), 8790-8839.

[150] Li, S.; Zhang, S. Q.; Shen, L.; Liu, Q.; Ma, J. B.; Lv, W.; He, Y. B.; Yang, Q. H., Progress and perspective of ceramic/polymer composite solid electrolytes for lithium batteries. *Advanced Science* **2020,** *7* (5), 1903088.

[151] Feng, J.; Wang, L.; Chen, Y.; Wang, P.; Zhang, H.; He, X., PEO based polymer-ceramic hybrid solid electrolytes: a review. *Nano Convergence* **2021,** *8*, 1-12.

[152] Chen, J.; Li, Q.; Pollard, T. P.; Fan, X.; Borodin, O.; Wang, C., Electrolyte design for Li metal-free Li batteries. *Materials Today* **2020,** *39*, 118-126.

[153] Xiao, J.; Li, Q.; Bi, Y.; Cai, M.; Dunn, B.; Glossmann, T.; Liu, J.; Osaka, T.; Sugiura, R.; Wu, B., Understanding and applying coulombic efficiency in lithium metal batteries. *Nature Energy* **2020,** *5* (8), 561-568.

[154] Varzi, A.; Raccichini, R.; Passerini, S.; Scrosati, B., Challenges and prospects of the role of solid electrolytes in the revitalization of lithium metal batteries. *Journal of Materials Chemistry A* **2016,** *4* (44), 17251-17259.

[155] Zhang, S.; Zhao, F.; Chen, J.; Fu, J.; Luo, J.; Alahakoon, S. H.; Chang, L.-Y.; Feng, R.; Shakouri, M.; Liang, J., A family of oxychloride amorphous solid electrolytes for long-cycling all-solid-state lithium batteries. *Nature Communications* **2023,** *14* (1), 3780.

[156] Conder, J.; Bouchet, R.; Trabesinger, S.; Marino, C.; Gubler, L.; Villevieille, C., Direct observation of lithium polysulfides in lithium–sulfur batteries using operando X-ray diffraction. *Nature Energy* **2017,** *2* (6), 1-7.

[157] Zhang, X. Q.; Chen, X.; Cheng, X. B.; Li, B. Q.; Shen, X.; Yan, C.; Huang, J. Q.;

Zhang, Q., Highly stable lithium metal batteries enabled by regulating the solvation of lithium ions in nonaqueous electrolytes. *Angewandte Chemie International Edition* **2018,** *57* (19), 5301-5305.

[158] Wang, F.; Cheng, J., Unraveling the origin of reductive stability of super-concentrated electrolytes from first principles and unsupervised machine learning. *Chemical Science* **2022,** *13* (39), 11570-11576.

[159] Reus, M. A.; Reb, L. K.; Weinzierl, A. F.; Weindl, C. L.; Guo, R.; Xiao, T.; Schwartzkopf, M.; Chumakov, A.; Roth, S. V.; Müller-Buschbaum, P., Time-resolved orientation and phase analysis of lead halide perovskite film annealing probed by in situ GIWAXS. *Advanced Optical Materials* **2022,** *10* (14), 2102722.

[160] Qin, M.; Chan, P. F.; Lu, X., A systematic review of metal halide perovskite crystallization and film formation mechanism unveiled by in situ GIWAXS. *Advanced Materials* **2021,** *33* (51), 2105290.

[161] Xu, B.; Li, X.; Yang, C.; Li, Y.; Grundish, N. S.; Chien, P.-H.; Dong, K.; Manke, I.; Fang, R.; Wu, N.; Xu, H.; Dolocan, A.; Goodenough, J. B., Interfacial chemistry enables stable cycling of all-solid-state li metal batteries at high current densities. *Journal of the American Chemical Society* **2021,** *143* (17), 6542-6550.

[162] Wang, C.; Yang, Y.; Liu, X.; Zhong, H.; Xu, H.; Xu, Z.; Shao, H.; Ding, F., Suppression of lithium dendrite formation by using LAGP-PEO (LiTFSI) composite solid electrolyte and lithium metal anode modified by PEO (LiTFSI) in all-solid-state lithium batteries. *ACS Applied Materials & Interfaces* **2017,** *9* (15), 13694-13702.

[163] Zhang, N.; He, J.; Han, W.; Wang, Y., Composite solid electrolyte PEO/SN/$LiAlO_2$ for a solid-state lithium battery. *Journal of Materials Science* **2019,** *54* (13), 9603-9612.

[164] Guo, B.; Fu, Y.; Wang, J.; Gong, Y.; Zhao, Y.; Yang, K.; Zhou, S.; Liu, L.; Yang, S.; Liu, X., Strategies and characterization methods for achieving high performance PEO-based solid-state lithium-ion batteries. *Chemical Communications* **2022,** *58* (59), 8182-8193.

[165] Johari, S.; Tajuddin, N. A.; Hanibah, H.; Deraman, S. K., A review: ionic conductivity of solid polymer electrolyte based polyethylene oxide. *International Journal of Electrochemical Science* **2021,** *16* (2).

[166] Muller-Buschbaum, P., The active layer morphology of organic solar cells probed with grazing incidence scattering techniques. *Advanced Materials* **2014,** *26* (46), 7692-709.

[167] Hexemer, A.; Müller-Buschbaum, P., Advanced grazing-incidence techniques for modern soft-matter materials analysis. *IUCrJ* **2015,** *2* (1), 106-125.

[168] Weindl, C. L.; Fajman, C. E.; Giebel, M. A.; Wienhold, K. S.; Yin, S.; Tian, T.; Geiger, C.; Kreuzer, L. P.; Schwartzkopf, M.; Roth, S. V., Effect of solvent vapor annealing on diblock copolymer-templated mesoporous Si/Ge/C thin films: Implications for Li-ion batteries. *ACS Applied Nano Materials* **2022,** *5* (5), 7278-7287.

[169] Oechsle, A. L.; Heger, J. E.; Li, N.; Yin, S.; Bernstorff, S.; Müller-Buschbaum, P., In Situ Observation of morphological and oxidation level degradation processes within ionic liquid post-treated PEDOT: PSS thin films upon operation at high temperatures. *ACS Applied Materials & Interfaces* **2022,** *14* (27), 30802-30811.

[170] Zhao, Z.; Chen, W.; Impeng, S.; Li, M.; Wang, R.; Liu, Y.; Zhang, L.; Dong, L.; Unruangsri, J.; Peng, C., Covalent organic framework-based ultrathin crystalline porous film: manipulating uniformity of fluoride distribution for stabilizing lithium metal anode. *Journal of Materials Chemistry A* **2020,** *8* (6), 3459-3467.

[171] Fujii, K.; Wakamatsu, H.; Todorov, Y.; Yoshimoto, N.; Morita, M., Structural and electrochemical properties of Li ion solvation complexes in the salt-concentrated electrolytes using an aprotic donor solvent, N, N-Dimethylformamide. *The Journal of Physical Chemistry C* **2016,** *120* (31), 17196-17204.

[172] Yan, C.; Yao, Y. X.; Chen, X.; Cheng, X. B.; Zhang, X. Q.; Huang, J. Q.; Zhang, Q., Lithium nitrate solvation chemistry in carbonate electrolyte sustains high-voltage lithium metal batteries. *Angewandte Chemie International Edition* **2018,** *57* (43), 14055-14059.

[173] Cabañero Martínez, M. A.; Boaretto, N.; Naylor, A. J.; Alcaide, F.; Salian, G. D.; Palombarini, F.; Ayerbe, E.; Borras, M.; Casas-Cabanas, M., Are polymer-based electrolytes ready for high-voltage lithium battery applications? An overview of degradation mechanisms and battery performance. *Advanced Energy Materials* **2022,** *12* (32), 2201264.

[174] Yang, X.; Jiang, M.; Gao, X.; Bao, D.; Sun, Q.; Holmes, N.; Duan, H.; Mukherjee, S.; Adair, K.; Zhao, C.; Liang, J.; Li, W.; Li, J.; Liu, Y.; Huang, H.; Zhang, L.; Lu, S.; Lu, Q.; Li, R.; Singh, C. V.; Sun, X., Determining the limiting factor of the electrochemical stability window for PEO-based solid polymer electrolytes: main chain or terminal –OH group? *Energy & Environmental Science* **2020,** *13* (5), 1318-1325.

[175] Chen, H.; Adekoya, D.; Hencz, L.; Ma, J.; Chen, S.; Yan, C.; Zhao, H.; Cui, G.; Zhang, S., Stable seamless interfaces and rapid ionic conductivity of Ca–CeO_2/LiTFSI/PEO composite electrolyte for high-rate and high-voltage all-solid-state battery. *Advanced Energy Materials* **2020,** *10* (21), 2000049.

[176] Lyu, W.; He, G.; Liu, T., PEO-LITFSI-SiO_2-SN system promotes the application of polymer electrolytes in all-solid-state lithium-ion batteries. *ChemistryOpen* **2020,** *9* (6), 713-718.

[177] Xu, B.; Li, X.; Yang, C.; Li, Y.; Grundish, N. S.; Chien, P. H.; Dong, K.; Manke, I.; Fang, R.; Wu, N.; Xu, H.; Dolocan, A.; Goodenough, J. B., Interfacial chemistry enables stable cycling of all-solid-state li metal batteries at high current densities. *Journal of the American Chemical Society* **2021,** *143*(17):6542-6550.

[178] Das, S.; Ghosh, A., Ion conduction and relaxation in PEO-LiTFSI-Al_2O_3 polymer nanocomposite electrolytes. *Journal of Applied Physics* **2015,** *117* (17), 174103.

[179] Wang, C.; Wang, T.; Wang, L.; Hu, Z.; Cui, Z.; Li, J.; Dong, S.; Zhou, X.; Cui, G., Differentiated lithium salt design for multilayered PEO electrolyte enables a high-voltage solid-state lithium metal battery. *Advanced Science* **2019,** *6* (22), 1901036.

[180] Fang, R.; Xu, B.; Grundish, N. S.; Xia, Y.; Li, Y.; Lu, C.; Liu, Y.; Wu, N.; Goodenough, J. B., Li_2S_6-integrated PEO-based polymer electrolytes for all-solid-state lithium-metal batteries. *Angewandte Chemie* **2021,** *133* (32), 17842-17847.

[181] Liu, Y.; Tao, X.; Wang, Y.; Jiang, C.; Ma, C.; Sheng, O.; Lu, G.; Lou, X. W., Self-assembled monolayers direct a LiF-rich interphase toward long-life lithium metal batteries. *Science* **2022,** *375* (6582), 739-745.

[182] Wu, N.; Chien, P. H.; Qian, Y.; Li, Y.; Xu, H.; Grundish, N. S.; Xu, B.; Jin, H.; Hu, Y. Y.; Yu, G., Enhanced surface interactions enable fast Li+ conduction in oxide/polymer composite electrolyte. *Angewandte Chemie International Edition* **2020,** *59* (10), 4131-4137.

[183] Adenusi, H.; Chass, G. A.; Passerini, S.; Tian, K. V.; Chen, G., Lithium batteries and the solid electrolyte interphase (SEI) — Progress and outlook. *Advanced Energy Materials* **2023,** *13* (10), 2203307.

[184] Li, M.; Lu, J.; Chen, Z.; Amine, K., 30 years of lithium-ion batteries. *Advanced Materials* **2018,** *30* (33), 1800561.

[185] Huang, A.; Ma, Z.; Kumar, P.; Liang, H.; Cai, T.; Zhao, F.; Cao, Z.; Cavallo, L.; Li, Q.; Ming, J., Low-temperature and fast-charging lithium metal batteries enabled by solvent–solvent interaction mediated electrolyte. *Nano Letters* **2024,** *24* (24), 7499-7507.

[186] Chen, Y.; Ma, Z.; Wang, Y.; Kumar, P.; Zhao, F.; Cai, T.; Cao, Z.; Cavallo, L.; Cheng, H.; Li, Q.; Ming, J., Trace ethylene carbonate-mediated low-concentration ether-based electrolytes for high-voltage lithium metal batteries. *Energy &*

Environmental Science **2024,** *17* (15), 5613-5626.

[187] Zou, Y.; Liu, G.; Wang, Y.; Li, Q.; Ma, Z.; Yin, D.; Liang, Y.; Cao, Z.; Cavallo, L.; Kim, H.; Wang, L.; Alshareef, H. N.; Sun, Y.-K.; Ming, J., Intermolecular interactions mediated nonflammable electrolyte for high-voltage lithium metal batteries in wide temperature. *Advanced Energy Materials* **2023,** *13* (19), 2300443.

[188] Chen, J.; Li, Z.; Sun, N.; Xu, J.; Li, Q.; Yao, X.; Ming, J.; Peng, Z., A robust li-intercalated interlayer with strong electron withdrawing ability enables durable and high-rate li metal anode. *ACS Energy Letters* **2022,** *7* (5), 1594-1603.

[189] Li, D.; Liu, H.; Wang, C.; Yan, C.; Zhang, Q.; Nan, C.-W.; Fan, L.-Z., High ionic conductive, mechanical robust sulfide solid electrolyte films and interface design for all-solid-state lithium metal batteries. *Advanced Functional Materials* **2024,** *34* (27), 2315555.

[190] Nikodimos, Y.; Jiang, S.-K.; Huang, S.-J.; Taklu, B. W.; Huang, W.-H.; Desta, G. B.; Tekaligne, T. M.; Muche, Z. B.; Lakshmanan, K.; Chang, C.-Y.; Hagos, T. M.; Shitaw, K. N.; Yang, S.-C.; Wu, S.-H.; Su, W.-N.; Hwang, B. J., Moisture robustness of Li_6PS_5Cl argyrodite sulfide solid electrolyte improved by nano-level treatment with lewis acid additives. *ACS Energy Letters* **2024,** *9* (4), 1844-1852.

[191] Kim, D.; Nguyen, M. H.; Chun, S. H.; Jeon, J.; Kim, B.-K.; Park, S., Stabilization of $Li_7La_3Zr_2O_{12}$ solid electrolyte through Ga-based precipitates and the Ga–Au surface layer. *International Journal of Energy Research* **2024,** *2024* (1), 9050890.

[192] Ghosh, K.; Wasim Raja, M., Facile Li-ion transport in microstructurally engineered hybrid LLZO electrolyte for application in pseudo-solid state lithium metal batteries. *Chemical Engineering Journal* **2024,** *480*, 148200.

[193] Wang, Y.; Li, T.; Yang, X.; Yin, Q.; Wang, S.; Zhang, H.; Li, X., 2D solid-electrolyte interphase built by high-concentration polymer electrolyte for highly reversible silicon anodes. *Advanced Energy Materials* **2024,** *14* (2), 2303189.

[194] Yang, J.; Li, R.; Zhang, P.; Zhang, J.; Meng, J.; Li, L.; Li, Z.; Pu, X., Crosslinked polymer-in-salt solid electrolyte with multiple ion transport paths for solid-state lithium metal batteries. *Energy Storage Materials* **2024,** *64*, 103088.

[195] Li, S.; Zhang, S.-Q.; Shen, L.; Liu, Q.; Ma, J.-B.; Lv, W.; He, Y.-B.; Yang, Q.-H. Progress and perspective of ceramic/polymer composite solid electrolytes for lithium batteries *Advanced Science*, **2020**, *7*(5), 1903088.

[196] Pitawala, H. M. J. C.; Dissanayake, M. A. K. L.; Seneviratne, V. A.; Mellander, B. E.; Albinson, I., Effect of plasticizers (EC or PC) on the ionic conductivity and thermal properties of the $(PEO)_9LiTf$: Al_2O_3 nanocomposite polymer electrolyte

system. *Journal of Solid State Electrochemistry* **2008,** *12* (7), 783-789.

[197] Cai, T.; Wang, Y.; Zhao, F.; Ma, Z.; Kumar, P.; Xie, H.; Sun, C.; Wang, J.; Li, Q.; Guo, Y.; Ming, J., Graphic, Quantitation, visualization, standardization, digitization, and intelligence of electrolyte and electrolyte-electrode interface. *Advanced Energy Materials* **2024,** *14* (25), 2400569.

[198] Wei, P.; Wang, H.; Yang, M.; Wang, J.; Wang, D., Relocatable hollow multishelled structure-based membrane enables dendrite-free lithium deposition for ultrastable lithium metal batteries. *Advanced Energy Materials* **2024,** *14* (22), 2400108.

[199] Wang, C.; Wang, H.; Tao, L.; Wang, X.; Cao, P.; Lin, F.; Xin, H. L., Direct observation of nucleation and growth behaviors of lithium by in situ electron microscopy. *ACS Energy Letters* **2023,** *8* (4), 1929-1935.

[200] Bradbury, R.; Kardjilov, N.; Dewald, G. F.; Tengattini, A.; Helfen, L.; Zeier, W. G.; Manke, I., Visualizing Lithium ion transport in solid-state Li–S batteries using 6Li contrast enhanced neutron imaging. *Advanced Functional Materials* **2023,** *33* (38), 2302619.

[201] Bradbury, R.; Dewald, G. F.; Kraft, M. A.; Arlt, T.; Kardjilov, N.; Janek, J.; Manke, I.; Zeier, W. G.; Ohno, S., Visualizing reaction fronts and transport limitations in solid-state Li–S batteries via operando neutron imaging. *Advanced Energy Materials* **2023,** *13* (17), 2203426.

[202] Sun, F.; He, X.; Jiang, X.; Osenberg, M.; Li, J.; Zhou, D.; Dong, K.; Hilger, A.; Zhu, X.; Gao, R.; Liu, X.; Huang, K.; Ning, D.; Markötter, H.; Zhang, L.; Wilde, F.; Cao, Y.; Winter, M.; Manke, I., Advancing knowledge of electrochemically generated lithium microstructure and performance decay of lithium ion battery by synchrotron X-ray tomography. *Materials Today* **2019,** *27*, 21-32.

[203] Sun, F.; Zhou, D.; He, X.; Osenberg, M.; Dong, K.; Chen, L.; Mei, S.; Hilger, A.; Markötter, H.; Lu, Y.; Dong, S.; Marathe, S.; Rau, C.; Hou, X.; Li, J.; Stan, M. C.; Winter, M.; Dominko, R.; Manke, I., Morphological reversibility of modified Li-based anodes for next-generation batteries. *ACS Energy Letters* **2020,** *5* (1), 152-161.

[204] Lu, J.; Zhang, S.; Yao, J.; Guo, Z.; Osenberg, M.; Hilger, A.; Markötter, H.; Wilde, F.; Manke, I.; Zhang, X.; Sun, F.; Cui, G., Synergistic effect of CO_2 in accelerating the galvanic corrosion of lithium/sodium anodes in alkali metal–carbon dioxide batteries. *ACS Nano* **2024,** *18* (16), 10930-10945.

[205] Melnikov, A. P.; Rosenthal, M.; Rodygin, A. I.; Doblas, D.; Anokhin, D. V.; Burghammer, M.; Ivanov, D. A., Re-exploring the double-melting behavior of semirigid-chain polymers with an in-situ combination of synchrotron nano-focus X-ray scattering and nanocalorimetry. *European Polymer Journal* **2016,** *81*, 598-

606.

[206] Buffet, A.; Rothkirch, A.; Döhrmann, R.; Körstgens, V.; Abul Kashem, M. M.; Perlich, J.; Herzog, G.; Schwartzkopf, M.; Gehrke, R.; Müller-Buschbaum, P.; Roth, S. V., P03, the microfocus and nanofocus X-ray scattering (MiNaXS) beamline of the PETRA III storage ring: the microfocus endstation. *J Synchrotron Radiation* **2012,** *19* (4), 647-53.

[207] van Laack, V.; Langer, F.; Hartwig, A.; Koschek, K., Succinonitrile-polymer composite electrolytes for li-ion solid-state batteries — The influence of polymer additives on thermomechanical and electrochemical properties. *ACS Omega* **2023,** *8* (10), 9058-9066.

[208] Zhang, X.; Fu, C.; Cheng, S.; Zhang, C.; Zhang, L.; Jiang, M.; Wang, J.; Ma, Y.; Zuo, P.; Du, C.; Gao, Y.; Yin, G.; Huo, H., Novel PEO-based composite electrolyte for low-temperature all-solid-state lithium metal batteries enabled by interfacial cation-assistance. *Energy Storage Materials* **2023,** *56*, 121-131.

[209] Alarco, P.-J.; Abu-Lebdeh, Y.; Abouimrane, A.; Armand, M., The plastic-crystalline phase of succinonitrile as a universal matrix for solid-state ionic conductors. *Nature Materials* **2004,** *3* (7), 476-481.

[210] Usta, S.; Çelik, M.; Çetinkaya, T., Enhancement of the stability window of PEO for high voltage all-solid-state lithium batteries. *Journal of Power Sources* **2023,** *580*, 233404.

[211] Gupta, R. K.; Shaikh, H.; Imran, A.; Bedja, I.; Ajaj, A. F.; Aldwayyan, A. S.; Khan, A.; Ayub, R., Electrical transport properties of [(1−x)succinonitrile: xpoly(ethyleneoxide)]–$LiCF_3SO_3$–Co[tris-(2,2′-bipyridine)]$_3$$(TFSI)_2$–Co[tris-(2,2′-bipyridine)]$_3$$(TFSI)_3$ solid redox mediators. *RSC Advances* **2024,** *14* (1), 539-547.

[212] Wang, S.; Sun, Q.; Zhang, Q.; Li, C.; Xu, C.; Ma, Y.; Shi, X.; Zhang, H.; Song, D.; Zhang, L., Li-ion transfer mechanism of ambient-temperature solid polymer electrolyte toward lithium metal battery. *Advanced Energy Materials* **2023,** *13* (16), 2204036.

[213] Liu, Y.; Zhao, Y.; Lu, W.; Sun, L.; Lin, L.; Zheng, M.; Sun, X.; Xie, H., PEO based polymer in plastic crystal electrolytes for room temperature high-voltage lithium metal batteries. *Nano Energy* **2021,** *88*, 106205.

[214] Sreepathi Rao, S.; Jaipal Reddy, M.; Laxmi Narsaiah, E.; Subba Rao, U. V., Development of electrochemical cells based on (PEO + $NaYF_4$) and (PEO + KYF_4) polymer electrolytes. *Materials Science and Engineering: B* **1995,** *33* (2), 173-177.

[215] Liu, L.; Wang, T.; Sun, L.; Song, T.; Yan, H.; Li, C.; Mu, D.; Zheng, J.; Dai, Y.,

Stable cycling of all-solid-state lithium metal batteries enabled by salt engineering of PEO-Based polymer electrolytes. *Energy & Environmental Materials* **2024,** *7* (2), e12580.

[216] Lu, Y.; Zhao, C.-Z.; Yuan, H.; Cheng, X.-B.; Huang, J.-Q.; Zhang, Q., Critical current density in solid-state lithium metal batteries: mechanism, influences, and strategies. *Advanced Functional Materials* **2021,** *31* (18), 2009925.

[217] Fang, C.-D.; Huang, Y.; Sun, Y.-F.; Sun, P.-F.; Li, K.; Yao, S.-Y.; Zhang, M.-Y.; Fang, W.-H.; Chen, J.-J., Revealing and reconstructing the 3D Li-ion transportation network for superionic poly(ethylene) oxide conductor. *Nature Communications* **2024,** *15* (1), 6781.

[218] Mendes, E.; Duarte, N., Mid-infrared spectroscopy as a valuable tool to tackle food analysis: a literature review on coffee, dairies, honey, olive oil and wine. *Food* **2021,** *10*, 477.

List of publications

Publications related to the dissertation

- Liang, Y.; Zheng, T.; Sun, K.; Xu, Z.; Guan, T.; Apfelbeck, F. A.C.; Pan, D.; Sharp, I. D.; Cheng, Y.; Schwartzkopf, M.; Roth, S. V.; Müller-Buschbaum, P., Operando study insights into lithiation/delithiation processes in a poly(ethylene oxide) electrolyte of all-Solid-State Lithium Batteries by Grazing-Incidence X-ray scattering. *ACS Applied Materials & Interface* **2024,** *16* (26), 33307-33315.

- Liang, Y.; Apfelbeck, F. A.C.; Sun, K.; Yan, Y.; Cheng, L.; Pan, G.; Zheng, T.; Cheng, Y.; Davydok, A.; Krywka, C.; Müller-Buschbaum, P., Unveiling the Li/electrolyte interface behavior for dendrite-free all-solid-state lithium metal batteries by *operando* nano-focus WAXS. *Advanced Science* **2025,** 2414714.

Further publications

- Sun, K., Guo, R., Liu, S., Guo, D., Jiang, X., Huber, L. F., Liang, Y, Reus, M.A., Li, Z., Guan, T., Zhou, J., Schwartzkopf, M., Stranks, S. D., Deschler, F., Müller-Buschbaum, P., Deciphering Structure and Charge Carrier Behavior in Reduced-Dimensional Perovskites. *Advanced Functional Materials*, **2024**, *34*(52), 2411153.

- Qiu, Q., Zheng, T., Huang, L., Xu, T., Pan, L., Sun, W., Tian, H., Zhang, W., Yu, Q., Liang, Y., Yan, Y., Yuan, J., Müller-Buschbaum, P., Xia, L., A small amount of sodium difluoro (oxalate) borate additive induces anion-derived interphases for sodium-ion batteries. *Energy Storage Materials*, **2024**, *73*, 103858.

- Zheng, T., Xu, T., Xiong, J., Xie, W., Wu, M., Yu, Y., Xu, Z., Liang, Y., Liao, C., Dong, X., Xia, Y., Cheng, Y., Xia, Y., Müller-Buschbaum, P., Multipoint anionic bridge: Asymmetric solvation structure improves the stability of lithium-ion

batteries. *Advanced Science*, **2024**, *11*(48), 2410329.

- Sun, K., Guo, R., Liang, Y., Heger, J. E., Liu, S., Yin, S., Reus, M.A., Spanier, L.V., Deschler, F., Bernstorff, S., Müller-Buschbaum, P., Morphological insights into the degradation of perovskite solar cells under light and humidity. *ACS Applied Materials & Interfaces*, **2023**, *15*(25), 30342-30349..

- Zheng, T., Zhu, B., Xiong, J., Xu, T., Zhu, C., Liao, C., Yin, S., Pan, G., Liang, Y., Shi, X., Zhao, H., Berger, R., Cheng, Y., Xia, Y., Müller-Buschbaum, P., When audience takes stage: Pseudo-localized-high-concentration electrolyte with lithium nitrate as the only salt enables lithium metal batteries with excellent temperature and cathode adaptability. *Energy Storage Materials*, **2023**, *59*, 102782.

Scientific reports

- Liang Y., Müller-Buschbaum P., "Influence of lithium additive and solvent on NMC111 cathode for lithium ion batteries" Lehrstuhl für Funktionelle Materialien, Annual Report, 2021.

- Liang Y., Roth, S. V.; Müller-Buschbaum P., "Operando study of poly (ethylene oxide) composite electrolyte in all-solid-state lithium batteries", Lehrstuhl für Funktionelle Materialien, Annual Report, 2022.

- Liang Y., Chumakov A., Roth, S. V.; Müller-Buschbaum P., "Operando study of poly(ethylene oxide) composite electrolyte in all-solid-state lithium batteries", Lehrstuhl für Funktionelle Materialien, Annual Report, 2023.

- Liang Y., Davydok A., Krywka, C.; Müller-Buschbaum P., "Unveiling the Li/electrolyte interface behavior for dendrite-free lithium batteries by operando nano-focus WAXS", Lehrstuhl für Funktionelle Materialien, Annual Report, 2024.

Conference talks

- Liang Y., Oechsle A-L., Reitenbach J., "Fourier transform infrared spectroscopy", Polymer Science Summer School, Obertauern, Austria, 2022.

- Liang Y., Pivarnikova I., Petz D., Westphal L., "Battery electrodes", Polymer Science Summer School, Obertauern, Austria, 2023.

- Liang Y., Li Z., Lindenmeir C., "Grazing-incident small-angle X-ray/Neutron scattering", Polymer Science Summer School, Raitenhaslach, Germany, 2024.

- Liang, Y.; Zheng, T.; Sun, K.; Xu, Z.; Guan, T.; Apfelbeck, F. A.C.; Pan, D.; Sharp, I. D.; Cheng, Y.; Schwartzkopf, M.; Roth, S. V.; Müller-Buschbaum, P., "In operando investigation of the poly(ethylene oxide) composite electrolyte in all-solid-state lithium batteries", DPG Spring Conference, Berlin, Germany, 2024.

- Liang, Y.; Apfelbeck, F. A.C.; Sun, K.; Yan, Y.; Cheng, L.; Pan, G.; Zheng, T.; Cheng, Y.; Davydok, A.; Krywka, C.; Müller-Buschbaum, P., "Unveiling the Li/electrolyte interface behavior for dendrite-free all-solid-state lithium metal batteries by *operando* nano-focus WAXS", European XFEL Users´ Meeting and DESY Photon Science Users´ Meeting 2025, Hamburg, Germany, 2025.

Conference poster presentations

- Liang Y., Müller-Buschbaum P., "In operando studies of solid polymer electrolyte for thin film Lithium-Ion battery", 11th Energy Colloquium of the Munich School of Engineering, Garching, Germany, 2021

- Liang Y., Müller-Buschbaum P., "Influence of Mg on the structure and electrolyte/electrode interface in all-solid-state lithium battery" DPG Meeting SKM 2021, Germany, 2021.

- Liang Y., Heger J. E., Müller-Buschbaum P., "Influence of Mg on the structure and electrolyte/electrode interface in all-solid-state lithium battery" MLZ User Meeting 2021, Munich, Germany, 2021.

- Liang Y., Xu Z., Sun K., Guan T., Apfelbeck F. A. C., Ding P., Sharp I. D., Müller-Buschbaum P., "Influence of solvent and lithium salt on the structure and Performance of NCM111 cathode for lithium ion batteries", 12th Energy Colloquium of the Munich Institute of Integrated Materials, Energy and Process Engineering (MEP), Garching, Germany, 2022.

- Liang Y., Xu Z., Sun K., Guan T., Apfelbeck F. A. C., Ding P., Sharp I. D., Müller-Buschbaum P., "Influence of solvent and lithium salt on the structure and Performance of NCM111 cathode for lithium ion batteries" DPG Fall Meeting, 2022, Rengensburg, Germany, 2022.

- Y Liang Y., Xu Z., Sun K., Guan T., Apfelbeck F. A. C., Ding P., Sharp I. D., Müller-Buschbaum P., “Influence of solvent and lithium salt on the structure and Performance of NCM111 cathode for lithium ion batteries”. MLZ User Meeting 2022, Munich, Germany, 2022.

- Liang Y., Zheng T., Sun K., Xu Z., Guan T., Apfelbeck F. A. C., Ding P., Sharp I. D., Cheng Y., Schwartzkopf M., Roth S. V., Muller-Buschbaum P., “Real-time monitoring the Li+ plating/stripping process in all-solid-state lithium battery by simultaneous grazing-incident small-angle/wide-angle X-ray scattering”, DPG Spring Meeting 2023, Dresden, Germany, 2023.

- Liang Y., Zheng T., Sun K., Xu Z., Guan T., Apfelbeck F. A. C., Ding P., Sharp I. D., Cheng Y., Schwartzkopf M., Roth S. V., Muller-Buschbaum P., “Real-time monitoring the Li+ plating/stripping process in all-solid-state lithium battery by simultaneous grazing-incident small-angle/wide-angle X-ray scattering”, 245th Electrochemical Society Meeting, San Francesco, America, 2024.

- Liang, Y.; Apfelbeck, F. A.C.; Sun, K.; Yan, Y.; Cheng, L.; Pan, G.; Zheng, T.; Cheng, Y.; Davydok, A.; Krywka, C.; Müller-Buschbaum, P., “Unveiling the Li/electrolyte interface behavior for dendrite-free all-solid-state lithium metal batteries by *operando* nano-focus WAXS”, European XFEL Users´ Meeting and DESY Photon Science Users´ Meeting 2025, Hamburg, Germany, 2025.

Acknowledgements

I would like to express my gratitude to everyone who contributed to the projects presented in this dissertation and supported me throughout the years. This thesis would not have been possible without their valuable contributions to the findings shared here. I would like to acknowledge them briefly, in no particular order.

I am deeply grateful to my supervisor, Prof. Dr. Peter Müller-Buschbaum, for giving me the opportunity to join the Chair of Functional Materials at the Physics Department, especially during a challenging time when I was dealing with visa issues and scholarship concerns. I have learned an immense amount from him, not only about advanced scattering techniques but also about presenting results and scientific writing. I am particularly thankful for the incredible opportunity to participate in several beamtimes at DESY (Deutsches Elektronen-Synchrotron) in Hamburg. He is super supportive when sending me to the conferences, workshops, and scientific meetings has been invaluable, allowing me to learn from other scientists and become an active member of the scientific community. Furthermore, I truly appreciate his sincere support in shaping my career, both professionally and personally.

I would also like to express my sincere gratitude to Prof. Yajun Cheng at the Hohai University for providing the battery testing system. I am truly grateful for your guidance and for sharing your extensive knowledge of lithium batteries at the beginning of my PhD journey. Your support has been invaluable.

Special thanks to our secretaries, Carola Kappauf, Sanja Ulrich, and Marion Waletzki, for their kind assistance with my chemical purchase, help in reimbursement, and excellent organization of group events during my time at the Chair.

I would like to thank the P03 beamline scientists at DESY, Hamburg, Prof. Dr. Stephan V. Roth, and Dr. Matthias Schwartzkopf, Dr. Chumakov, Dr. Anton Davydok, and Dr. Christina Krywka for providing me with access to learning and operating the synchrotron-based large facility. Your contribution has been instrumental to the success

of my projects. My thanks also go to the beamline Engineer Jan Rubeck who help us to setup all the instruments before the start of measurements.

I also want to thank my collaborators Dr. Pan Ding and Prof. Dr. Ian D. Sharp, for their assistance with applying for the X-ray scattering measurements and designing the 1st generation in-situ measurement chamber. I would like to express my deepest gratitude to our technical engineer, Mr. Reinhold, for his exceptional work in fabricating the 2nd and 3rd generation operando grazing-incident X-ray scattering measurement chambers and for skillfully manufacturing the battery electrolyte filming holder. Your expertise and dedication have been invaluable to this project. Thanks Fabian A. C. Apfelbeck and Dr. Gilles E. Wittmann for design the nWAXS measurement chamber.

I am highly appreciated that Liangzhen Liu who conduct the TGA measurements at Chemical research center, TUM.

I would like to extend my heartfelt thanks to Mr. Egon Lenker and Mr. Terry Weinmann for their invaluable assistance in upgrading the battery-testing oven and designing the PCB layout. Your unwavering support and readiness to help whenever I reached out have been truly appreciated.

I would like to express my heartfelt gratitude to my colleagues who shared the beamtime experience with me at the P03 beamline: Dr. Tianfu Guan, Dr. Pan Ding, Fabian A. C. Apfelbeck, Yingying Yan, Lyuyang Cheng, and Prof. Dr. Lan Xia. Thank you for generously sharing your expertise and experiences at the beamline and for your invaluable assistance in conducting experiments together. Your support and collaboration have been greatly appreciated. Additionally, I am grateful to the Alumni of E13: Dr. Renjun Guo, Dr. Suzhe Liang, Dr. Tianxiao Xiao, Dr. Nian Li, Dr. Shanshan Yin, Dr. Peixi Wang, Dr. Yanan Li, Dr. Ting Tian, Dr. Suo Tu, Dr. Julian E. Heger, Dr. Dominik Schwaiger, Dr. Lennart Reb, Dr. Christian Weindl, Dr. Apostolos Vagias, Dr. Anna-Lena Oechsle, Dr. Peixi Wang, Simon J. Schaper, Manuel Reus, Christina Geiger, whose scientific suggestions have helped and inspired me in my project.

I would also like to extend my gratitude to the students I had the privilege of advising during my doctoral studies: Tannu Garg, Manyank Garg, Alex Hinke, Niklas Reinecke, Ruodong Yang, and Thomas Bullinger. I am truly pleased that they found interest in my research topic and chose it for their graduation theses. Supervising them has been an enriching and rewarding experience, offering me the opportunity to develop and refine my team leadership skills. I am proud of their dedication and delighted that they successfully completed their theses.

Next, I want to express my gratitude to my current colleagues, Peiran Zhang, Julija Reitenbach, Guangjiu Pan, Thien An Pham, Ivana Pivarnikova, Christopher Everett, Constantin Harder, Lukas Spanier, Zhuijun Xu, Zerui Li, Xiongzhuo Jiang, Jinsheng Zhang, Altantulga Buyan-Arivjikh, Tianle Zheng, Dominik Petz, Huaying Zhong, Thomas Baier, Yusuf Bulut, Pablo Alvarez Herrera, Tobias Hölderle, Linus Huber, Yingjian Guo, Morgan Le Dû, , Wenqi Xu, Lukas Spanier, David Kosbahn, Feifei Zheng, Xiaojing Ci, Zhaonan Jin, and Lixing Li, for making this a wonderful experience at our Chair.

A big thank you to my fiancé, Kun Sun, for being by my side over the past four years. You are the inspiration behind my pursuit of a doctoral degree, and every moment of this journey has been worth it because of you. Thank you for being my friend, my teacher, my partner, and my family. Your unwavering support and love mean everything to me.

I would like to express my deepest gratitude to my parents, Bo Liang and Xiuying Zhang, for their unwavering support throughout my studies and their guidance in shaping my life. I am especially grateful to my paternal grandmother, whose curiosity about the world and nurturing presence inspired me from a young age. My farewell to Munich four years was our last goodbye, but I take comfort in knowing you will always be with me. A special thank you also goes to my maternal grandfather. I am truly grateful for the time we shared in your final days. Even though you may not have remembered who I was in your later years, I cherish those moments deeply.

My time at the Chair of Functional Materials over the past few years has been both rewarding and memorable. The moments shared with my kind and wonderful colleagues are among the highlights of this journey. I truly cherish our experiences, from beamtimes, summer schools, seminar talks, and conferences, to more relaxed gatherings like beer gardens, BBQs, defense celebrations, and coffee breaks. These shared moments have brought immense joy and created unforgettable memories that I will always treasure.

Finally, I would like to take a moment to say a big thank you to myself. For all the perseverance, hard work, and dedication that have brought me to this point. For pushing through challenges, staying focused, and continuously striving for growth. This journey has not always been easy, but through it all, I have remained committed to my goals, and I am proud of the progress I’ve made. This achievement is as much a result of my own efforts as it is of the support I’ve received along the way. Thank you for believing

in yourself and never giving up. The best is yet to come.

My last tribute is to those who knows I am not perfect but still love me.

Yuxin Liang
07.02.2025
Garching, Germany